MEASUREMENT OF THE BRANCHING FRACTION FOR $D^+ \to K^0_L \pi^+$

A Dissertation

Presented to the Faculty of the Graduate School

of Cornell University

in Partial Fulfillment of the Requirements for the Degree of

Doctor of Philosophy

by

Steven Richard Stroiney

January 2009

MEASUREMENT OF THE BRANCHING FRACTION FOR $D^+ \to K^0_L \pi^+$

Steven Richard Stroiney, Ph.D.

Cornell University 2009

The branching fraction for $D^+ \to K^0_L \pi^+$ is measured for the first time, using 281 pb^{-1} of e^+-e^-collisions recorded by the CLEO-c detector at the Cornell Electron Storage Ring. The analysis employs a missing mass technique which does not require reconstruction of the K^0_L. The resulting branching fraction is (1.460 ± 0.040 ± 0.035 ± 0.005)%, where the first uncertainty is statistical, the second is systematic, and the last is due to the input value of $\mathcal{B}(D^+ \to K^0_S \pi^+)$. Using an independent measurement of $\mathcal{B}(D^+ \to K^0_S \pi^+)$, we calculate that the asymmetry between $\mathcal{B}(D^+ \to K^0_S \pi^+)$ and $\mathcal{B}(D^+ \to K^0_L \pi^+)$ is $R(D^+) \equiv [\mathcal{B}(K^0_S \pi^+) - \mathcal{B}(K^0_L \pi^+)]/[\mathcal{B}(K^0_S \pi^+) + \mathcal{B}(K^0_L \pi^+)] = 0.022 \pm 0.016 \pm 0.018$. This result rules out scenarios of maximal interference between amplitudes for $D^+ \to K^0 \pi^+$ and $D^+ \to \bar{K}^0 \pi^+$, and it is consistent with theoretical predictions.

Measurement of track and K^0_S reconstruction efficiencies is also discussed. This analysis provides systematic uncertainties used in the measurement of $\mathcal{B}(D^+ \to K^0_L \pi^+)$ and in other CLEO-c analyses.

BIOGRAPHICAL SKETCH

Steven Stroiney's life story would not be interesting or exciting to anyone who does not know him, but he considers himself lucky to have lived where and when he has. Born in 1981, he grew up in Vernon, CT. He graduated from Rockville High School in 1999 and from Case Western Reserve University in 2003, with a major in Physics. He went immediately to graduate school at Cornell, hoping to learn something like "what the universe is *really* made of." He learned a more valuable lesson, though – that such a question is ultimately meaningless, and what matters is that our models correctly predict our sensory perceptions. At Cornell, Steve has worked on a variety of projects for the CLEO and CMS particle physics experiments. He is pleased to have played a role at the end of the CLEO experiment's long history and in the early days of the CMS experiment.

After graduating from Cornell, Steve will stay in Ithaca with his future wife, Terri Iwata, until she graduates.

To my family,

to my friends,

and to Terri, who is both, and more.

ACKNOWLEDGEMENTS

Any result in experimental particle physics is the product of an enormous number of people. The analyses I describe here are not just my own; they depend on the hard work and expertise of hundreds of others. They sit at the end of decades of effort to build, maintain, and operate CESR and CLEO. So I begin by thanking all those who contributed to this effort and made my work possible.

Stepping back farther, this work depends on a long history of scientific discovery. It is a cliché that we see farther because we stand on the shoulders of giants, but it is also well worth remembering every now and then.

With those grandiose sentiments out of the way, I would like to add some more personal acknowledgements. First I thank my advisor, Anders Ryd, who has offered excellent guidance and has given me many opportunities to work on interesting projects. I have learned a great deal from him; Anders can give a detailed explanation of most any topic, whether it's particle physics, detector hardware, simulations, statistics, software, or collaboration politics. And while he has plenty of advice and good suggestions, he has always allowed me the freedom to choose my own methods and to take ownership of my projects. I have appreciated the opportunity to choose an interesting variety of projects in the CLEO and CMS experiments, from data analysis to hardware maintenance to software development. On all of these projects, Anders invited me in as a full contributor with meaningful responsibilities.

I add my thanks to the many others who have helped me as informal advisors, including David Cassel, Werner Sun, and Peter Wittich.

I always found Wilson Lab to be a friendly place, and I have enjoyed the company of my colleagues. From chatting in the office or at lunch to playing poker to traveling for conferences, I have fond memories of the time I spent

with people here. In particular, my long-time officemates Laura, Jim, and Xin, our pseudo-officemate Peter, and all the other grad students I've known.

And, finally, my thanks to Cornell, for bringing me here to Ithaca, where I have enjoyed $5\frac{1}{2}$ happy years and where I met Terri.

TABLE OF CONTENTS

LIST OF TABLES

LIST OF FIGURES

CHAPTER 1

INTRODUCTION

The physics of D mesons is the physics both of charm quark decay and of strong interactions. Composed of a charm quark and a light anti-quark – anti-up for D^0 and anti-down for D^+ – D mesons decay through the weak decay of the charm quark. However, the light quark is also an active participant in these decays; it allows for forming some final states via multiple tree-level Feynman diagram topologies, and its interactions via the strong force make significant contributions to the decay amplitudes. Thus the physics of D decays is richer than just the decay of the charm quark.

The effect of the light quark may be illustrated by comparing the semileptonic and hadronic decay rates of D^0 and D^+. The total D^0 decay rate is about 2.5 times the D^+ rate, with lifetimes $\tau_{D^0} = (410.1 \pm 1.5) \times 10^{-15}$ sec and $\tau_{D^+} = (1040 \pm 7) \times 10^{-15}$ sec [1]. This difference is due entirely to the hadronic decays; the semileptonic decay rates of D^0 and D^+ are equal.[1] Semileptonic decays are dominated by a single Feynman diagram topology, in which the W from the charm quark decay forms a lepton-neutrino pair. Thus the rates are similar for D^0 and D^+. In contrast, the hadronic decay rates are very different for D^0 and D^+. In hadronic decays there are more tree-level Feynman diagram topologies, and these often generate interference which differs for D^0 and D^+. (We will see an example of this shortly.) Hence in hadronic decays the light quark plays a major role.

One particularly useful laboratory for studying the subtleties of D decays is the family of $D \to K\pi$ decays, where D, K, and π may be any of the ground-state charged or neutral particles bearing that label. These decays represent just a few

[1] The inclusive branching fraction for $D^0 \to e^+X$ is 6.71 ± 0.29 %, with a similar fraction for μ^+X. For $D^+ \to e^+X$, the branching fraction is 17.2 ± 1.9 % [1]. Combining these branching fractions with the D^0 and D^+ lifetimes, we see that the decay rates to e^+X are equal for D^0 and D^+.

percent of the overall D^0 and D^+ decay rates, but they do offer several advantages. As two-body decays, they are among the easier decays to measure experimentally. They are also free of complications from intermediate resonances, which obscure the interpretation of decays to three or more particles. Furthermore, a rich pattern of theoretical relationships connect these decays, enabling prediction of branching ratios and the search for second-order effects such as strong phases and interference.

Measurements of different $D \to K\pi$ branching fractions may be combined to relate the various decay amplitudes. For example, consider the four "right-sign" (Cabibbo-favored) diagrams in Figure 1.1. The two diagrams on the left are for D^0, and the two on the right are for D^+; they differ only by the identity of the spectator quark. The top diagrams are called "external spectator" diagrams, and the bottom ones are "internal spectator" diagrams. Note that the two D^0 diagrams give different final states, but the two D^+ diagrams give the same final state. If we assume isospin symmetry, in which the strong interaction does not distinguish between u and d quarks, then equivalent topologies have equal amplitudes. We can then use the branching fractions for the decays $D^0 \to K^-\pi^+$, $D^0 \to \bar{K}^0\pi^0$, and $D^+ \to \bar{K}^0\pi^+$ to determine the magnitude and relative phase of the amplitudes for external and internal topologies. We learn from this analysis that the magnitudes are close to equal and the phase is close to 180 degrees, so the amplitudes contributing to $D^+ \to \bar{K}^0\pi^+$ interfere destructively. This type of interference is one hypothesis for why the D^+ lifetime is longer than the D^0 lifetime; D^+ decay amplitudes interfere destructively while corresponding D^0 amplitudes produce different final states and therefore do not interfere [2]. More sophisticated theoretical treatments may use a greater number of D branching fractions to determine relationships between a greater number of topological

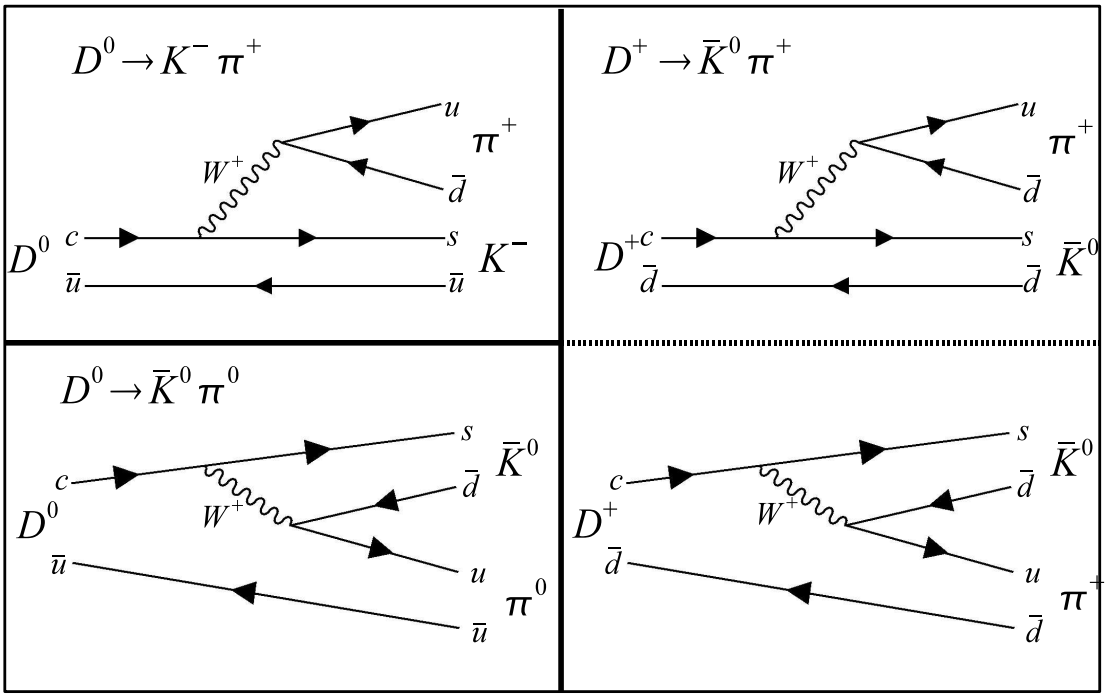

Figure 1.1: Diagrams for "right-sign" (Cabibbo-favored) $D \to K\pi$ decays. D^0 decays are on the left, and D^+ decays are on the right. The two D^0 decays produce different final states, while the D^+ decays produce the same final state. The diagrams on the left differ from those on the right only by the identity of the spectator quark $\bar{u}$ or $\bar{d}$.

amplitudes [3, 4].

An alternative to the topological approach is an isospin decomposition of the amplitudes. Amplitudes for the three Cabibbo-favored D decays may be written as linear combinations of two isospin amplitudes $A_{1/2}$ and $A_{3/2}e^{-i\delta_I}$:

$$\mathcal{A}(D^0 \to K^-\pi^+) = \sqrt{\frac{2}{3}}A_{1/2} + \sqrt{\frac{1}{3}}A_{3/2}e^{-i\delta_I} \quad (1.1)$$

$$\mathcal{A}(D^0 \to \bar{K}^0\pi^0) = -\sqrt{\frac{1}{3}}A_{1/2} + \sqrt{\frac{2}{3}}A_{3/2}e^{-i\delta_I} \quad (1.2)$$

$$\mathcal{A}(D^+ \to \bar{K}^0\pi^+) = \sqrt{3}A_{3/2}e^{-i\delta_I} \quad (1.3)$$

Here $A_{1/2}$ and $A_{3/2}$ are taken to be positive real numbers. As with the topological

amplitudes, using the three measured branching fractions we may solve for the constituent amplitudes. This analysis may be extended by also decomposing the doubly-Cabibbo-suppressed $D \to K\pi$ decays into isospin amplitudes and using measured branching fractions to relate them [5].

To observe the subtleties of D decays requires precision measurements, and for the past 5 years the CLEO-c experiment has been performing these measurements. CLEO-c is ideally suited for D physics; it has accumulated a large sample of $D\bar{D}$ pairs in a clean event environment, observed by a precise and well-characterized detector. The detector hardware is described in Chapter 2, and Chapter 3 describes the process of reconstructing final-state and short-lived particles in the collected data.

Precision studies require a careful and precise evaluation of the uncertainties. Most CLEO-c results depend on reconstruction efficiencies determined from a Monte Carlo simulation of the chain of particle decays, the propagation of final-state particles through the detector, and the response of active detector elements and electronics. It is essential to test and quantify the accuracy of this simulation. Chapter 4 describes the evaluation of systematic uncertainties for the simulation of track and K^0_S reconstruction efficiencies. These systematics serve as inputs to many CLEO-c analyses.

Among the D decay branching fractions measured by CLEO-c are all of the $D \to K\pi$ decays. In particular, the modes with a K^0_L in the final state were measured for the first time [6]. Previously, the difficulty of reconstructing the long-lived K^0_L meson proved insurmountable, but at CLEO-c the K^0_L can be inferred by reconstructing all other particles in the event and examining the missing energy and momentum. Chapter 5 describes the measurement of the decay $D^+ \to K^0_L\pi^+$.

CHAPTER 2

THE CLEO-C DETECTOR

The CLEO-c detector is located at the Cornell Electron Storage Ring (CESR), in which electrons and positrons circulate in opposite directions. During data-taking, the electrons and positrons are made to collide at the center of the detector. CLEO-c is composed of several systems which surround this interaction point and measure the products of each collision. These systems are designed to reconstruct charged particles and photons, measure their momentum or energy, and identify the type of each reconstructed particle.

Figures 2.1 and 2.2 show the CLEO-c detector in cutaway and quarter views. The component closest to the interaction point is the tracking system, which reconstructs the paths of charged particles. The particles' paths are curved by a 1T magnetic field, and the curvature of each track allows measurement of its momentum and charge. The tracking system is surrounded by the Ring Imaging Cherenkov Detector (RICH), which uses cones of Cherenkov light to help identify the particle type (pion, kaon, electon, muon, *etc.*) of each track. The next subsystem, just outside the RICH, is the crystal calorimeter. This device measures the position and energy of electromagnetic showers, permitting the reconstruction of photons and aiding the identification of electrons and positrons. Surrounding all of these systems is a superconducting solenoid used to produce the magnetic field. Outside the solenoid is the muon detector. It is not useful for CLEO-c analysis as the muons produced by D decays are not energetic enough to pass through the material in front of it.

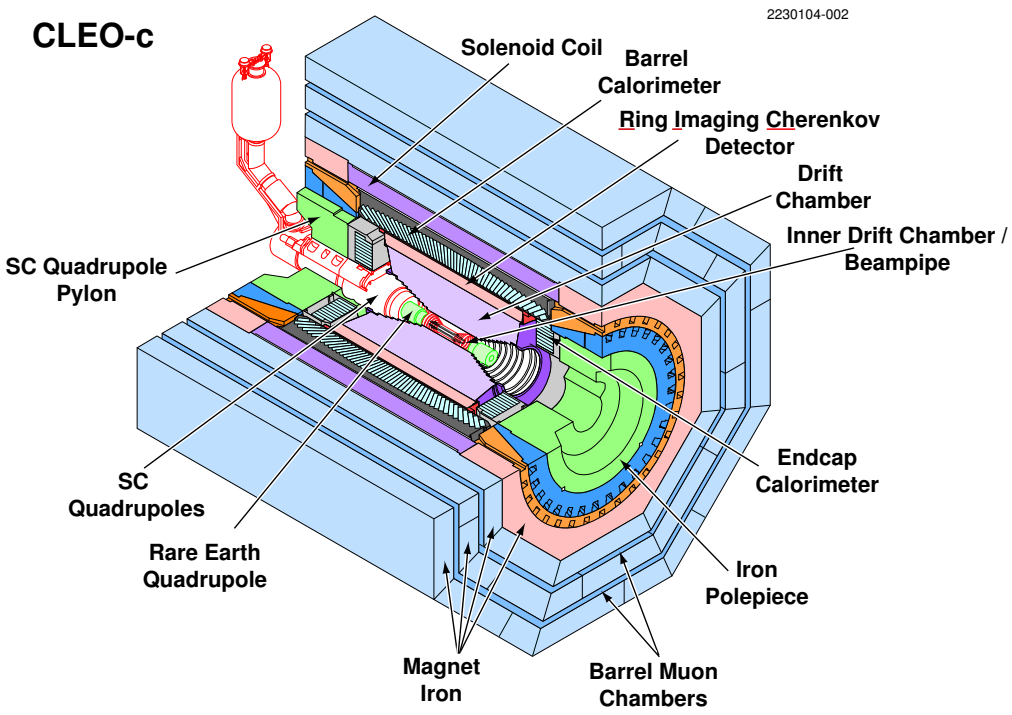

Figure 2.1: Cutaway view of the CLEO-c detector.

2.1 Tracking System

The tracking system consists of two cylindrical drift chambers: an inner 6-layer chamber (ZD) and an outer 47-layer chamber (DR) [7]. The ZD's six layers extend from a radius of 5.3 cm to 10.5 cm, and DR extends to an outer radius of 82 cm. The tracking system is nearly hermetic, covering 93% of the solid angle.

The drift chambers are filled with a helium-propane gas mixture, and tens of thousands of wires cross between the endplates. Approximately 10000 of these wires, called sense wires, are maintained at a high electric potential relative to the others, called field wires. When a charged particle passes through the chamber, it ionizes the gas, and the liberated electrons are drawn to the high potential of the sense wires. As these electrons approach a sense wire, they

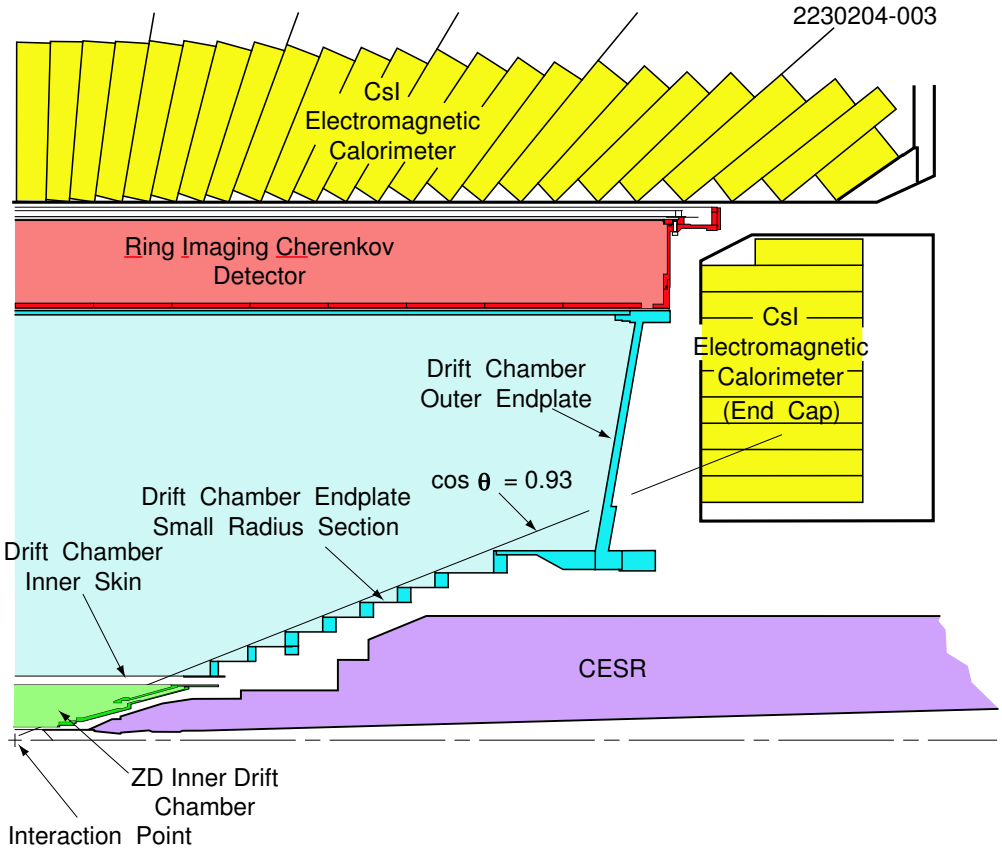

Figure 2.2: Quarter view of the CLEO-c detector.

induce further ionization in the gas nearby, which produces more electrons. All of these electrons are collected by the sense wire, and this signal is amplified and digitized. For each wire receiving a signal (a "hit"), two pieces of information are recorded – the precise time at which the electrons reached the wire, and the amount of charge received.

The timing information is used to determine the particle's distance of closest approach to each wire. The time between the electron-positron collision and the arrival of charge at the wire is the time required for the ionized electrons to drift through the gas from the track to the wire. The drift speed is known from calibration, so the drift time may be converted to a drift distance. A track

is reconstructed by combining hits from many wires and fitting them with a physical model of the particle's path in the magnetic field.

The charge received in each hit is converted to a measurement of the particle's energy loss (dE/dx). Because dE/dx varies as a function of momentum and particle mass according to the Bethe-Bloch equation, the energy loss information helps to distinguish different particle types.

If the drift chamber wires were all parallel to each other, then only two dimensions (perpendicular to the chamber axis) could be reconstructed. To enable reconstruction of the third dimension, a majority of the wires are oriented at a small "stereo" angle with respect to the chamber axis. Position in the third dimension is determined from the timing pattern of hits on layers with different stereo angles. Information about a track's position at the DR outer wall is also provided by cathode strips located on the wall.

The tracking system reconstructs charged particles at high efficiency and with excellent precision. For a particle that does not decay before exiting the drift chamber, reconstruction efficiency is nearly 100%. Hits are measured with spatial resolution better than 150 μm, leading to excellent momentum resolution for reconstructed tracks. The precision of the reconstructed momentum is 0.6% for a 1 GeV particle.

2.2 Ring Imaging Cherenkov Detector (RICH)

The RICH sub-detector [8] aids in particle identification (combined with dE/dx information from the tracking system). It sits just outside the drift chamber.

However, it lacks endcaps, and therefore its angular coverage extends to only 80% of the solid angle.

Particle identification in the RICH uses cones of Cherenkov light, which is generated by motion of a charged particle through a medium at a speed greater than the speed of light in that medium. The opening angle of the Cherenkov cone is a function of the particle's speed. This speed, combined with a momentum measurement from the tracking system, gives the mass of the particle and hence its identity. In practice the RICH does not measure the opening angle and speed at high precision, but the precision is sufficient to distinguish known particle types (*i.e.*, mass hypotheses) from each other.

Figure 2.3 shows a section of the RICH detector. Particles entering the RICH pass through a 1 cm LiF radiator located at the inner radius (82 cm); this generates the Cherenkov light. The Cherenkov photons travel through a 20-cm "expansion volume" (in which the Cherenkov cone expands) to the outer radius (102 cm), where the active detector elements are located. Here the Cherenkov photons are detected with multi-wire chambers. Hits in the multi-wire chambers form an ellipse segment for each Cherenkov cone, as shown in Figure 2.4. The passage of the charged particle through the multi-wire chamber is also detected, and this measurement is used along with the track parameters measured in the drift chamber to determine each particle's path through the RICH. Then, for each photon (cluster of hits) in the cone, the Cherenkov angle can be measured, and the average of these measurments is the opening angle of the Cherenkov cone. In practice, however, when performing particle identification, we do not measure the Cherenkov angle. Instead we compute a likelihood – based on the track path, photon positions, and their uncertainties – for each

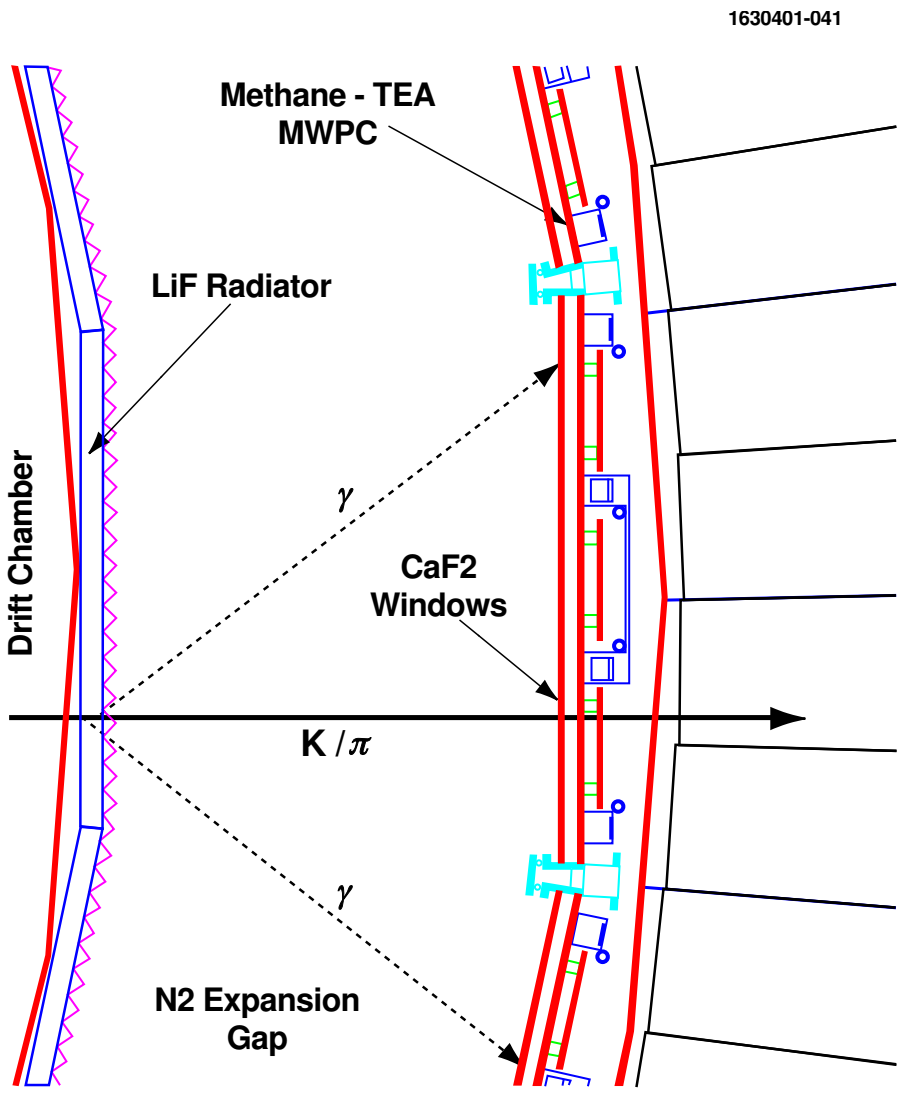

Figure 2.3: Section of the RICH detector.

mass hypothesis (pion mass, kaon mass, etc.). The likelihoods for different particles are compared to determine the most likely identity of a given track.

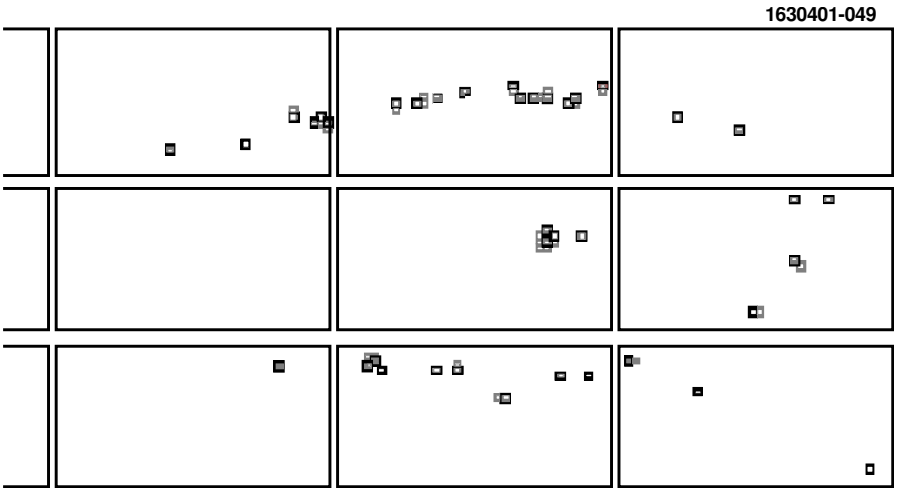

Figure 2.4: Example of hits produced by a Cherenkov cone in the RICH detector. The charged particle also produces a cluster at the center of the cone.

2.3 Crystal Calorimeter

Outside the tracking system and the RICH is the crystal calorimeter [9], used to reconstruct electromagnetic showers. The calorimeter consists of 7800 CsI crystals arrayed around the barrel of the detector and on the endcaps. The calorimeter covers 95% of the solid angle, though the barrel-endcap transition region suffers from poor performance.

The dimensions of each crystal are 5 cm $\times$ 5 cm $\times$ 30 cm, where the long dimension points along a line passing close to the interaction point. This length is 16 CsI radiation lengths, meaning that the calorimeter absorbs effectively all of the energy of an electron or photon. It also absorbs a smaller fraction of the energy of a hadron passing through. Four photodiodes are mounted to the back end of each crystal to measure the scintillation light.

The crystal size of 5 cm $\times$ 5 cm is small enough that a typical shower will

be spread over many adjacent crystals. This allows for interpolation between crystals, based on the amount of energy deposited in each one, to determine the center of the shower. Hence the position resolution is much better than the 5-cm size of each crystal. The pattern of energy deposition is also used to distinguish electromagnetic showers from hadronic showers; electromagnetic showers are narrower than hadronic showers and therefore deposit energy on a smaller cluster of crystals.

The calorimeter reconstructs photon energies with a precision of 2.2% at E_γ = 1 GeV and 5% at 100 MeV.

In D decays, the calorimeter serves two main functions. First, pairs of photons are combined to form neutral particle candidates (π^0 and η). Second, electrons are identified by comparing the track momentum with the energy deposited in the calorimeter where the track entered; for electrons these should be nearly equal.

2.4 CLEO-c Run Strategy

For D physics, the ideal e^+-e^-collision energy is at the $\psi(3770)$ resonance. This point has a relatively high cross section, and the energy is just high enough to produce a $D^0\bar{D}^0$ or D^+D^- pair. However, there is not enough energy to produce any other massive particles along with the $D\bar{D}$ pair. This event environment has several advantages. First, events are clean, containing nothing but the D and $\bar{D}$ decay products. Second, since D mesons are always produced in pairs, an event is "tagged" as $D\bar{D}$ when just one of them is reconstructed. Thus, when a $\bar{D}$ is found in an event, there must also be a D. This is useful in branching frac-

tion measurements because it provides a good measurement of the number of D mesons produced. Finally, the kinematics of $D\bar{D}$ events are very simple. In the center-of-mass frame the D and $\bar{D}$ are back-to-back with the same momentum magnitude; this momentum can be calculated from the beam collision energy. In CLEO-c analyses, reconstruction of D mesons takes advantage of these kinematic features.

Approximately half of CLEO-c data are collected at the $\psi(3770)$ resonance. The remainder is taken at higher energy to produce $D_s^{*\pm}D_s^{\mp}$ pairs or at lower energy to produce the $\psi(2S)$. The analyses in this dissertation use only the $\psi(3770)$ data.

CHAPTER 3

PARTICLE RECONSTRUCTION

The objects directly measured by the CLEO-c detector are charged tracks and electromagnetic showers. The underlying physics, though, is a series of decays of short-lived particles that ends with the final-state particles observed in the detector. To understand the underlying physics, we must analyze the final-state particles to determine the chain of decays that produced them.

The particles produced in an e^+-e^-collision are of three basic types:

- long-lived particles that are directly observed by the detector (π^+, K^+, γ)
- short-lived particles that decay inside the detector to other particles (D^0, D^+, π^0, K^0_S)
- long-lived particles that are invisible or nearly invisible to the detector (ν, K^0_L)

First, the detector objects must be identified as particular particles or rejected as fakes. Then, short-lived particles are reconstructed by forming combinations of these directly-observed particles. Finally, a single invisible particle may be inferred if every other particle in the event has been reconstructed.

3.1 Track and Shower Identification

This section describes the requirements that identify tracks and showers as particular particle types and that reject fakes.

3.1.1 Track Quality Requirements

We impose requirements on track quality to exclude poorly-measured tracks, fake tracks, and secondary tracks (those due to particles not produced in the primary e^+-e^-interaction). To reject poorly-measured and fake tracks, we require that each track produced hits in at least half of the drift chamber layers it passed through. Also, the reconstructed direction must lie within the fiducial volume of the drift chamber; its polar angle θ (the angle relative to the beam line) must satisfy $|\cos\theta| < 0.93$. To eliminate secondary tracks, we require that each track is consistent with coming from the e^+-e^-interaction point. In the dimension parallel to the beam line, the track must pass within 5 cm of this point, and in the transverse direction it must pass within 0.5 cm. These position requirements correspond to approximately 5 standard deviations, so almost all primary tracks satisfy them.

Tracks used for reconstructing $K^0_S \to \pi^+\pi^-$ are not subject to these requirements. A K^0_S typically travels several centimeters before decaying, so a requirement that tracks originate at the interaction point would eliminate most of these pion tracks.

3.1.2 Charged Particle Identification

Identification of charged tracks as particular particle types makes use of two pieces of information: energy loss (dE/dx) measured in the drift chamber and Cherenkov photons from the RICH subdetector. Energy loss depends on both momentum and particle type, as shown in Figure 3.1. Using the measured track momentum, the measured energy loss identifies the particle. In some momen-

tum ranges, the dE/dx curves of different particles nearly overlap, and so the particle type is ambiguous. In particular, at high momentum the curves for pions and kaons overlap, and so dE/dx does not cleanly distinguish between them. For the analyses described in this dissertation, a pion (kaon) candidate must have a measured energy loss within three standard deviations of the expected value for pions (kaons). If the measured dE/dx is consistent with both the pion and kaon hypotheses, the more likely hypothesis is identified by the χ^2 difference $\Delta\chi^2_E \equiv \chi^2_E(\pi) - \chi^2_E(K)$, where each χ^2 is calculated from the measured dE/dx, the expected value for a pion or kaon, and the standard deviation.

To determine the particle type for high-momentum tracks, we also use information from the RICH subdetector if the track passes through it.[1] The RICH information is used only if the track momentum is greater than 700 MeV. This value is far enough above the Cherenkov threshold to provide good separation between pions and kaons, and below 700 MeV dE/dx information provides excellent separation by itself. For tracks above 700 MeV, the track parameters and the measured Cherenkov photons are used to form a likelihood for pion and kaon hypotheses [8]. From these likelihoods we calculate a χ^2 difference between the pion and kaon hypotheses: $\Delta\chi^2_R \equiv \chi^2_R(\pi) - \chi^2_R(K)$. A value of $\Delta\chi^2_R$ greater than (less than) zero indicates that the particle is more likely to be a kaon (pion).

To combine dE/dx and RICH information, we sum the two χ^2 differences: $\Delta\chi^2 = \Delta\chi^2_E + \Delta\chi^2_R$. A particle is considered a kaon candidate if $\Delta\chi^2 \geq 0$ and is considered a pion candidate if $\Delta\chi^2 \leq 0$. If either dE/dx or RICH information is not available or not used, then the χ^2 difference from the other system is used to distinguish pions from kaons.

[1] This corresponds to a requirement that the polar angle θ satisfies $|\cos\theta| < 0.8$.

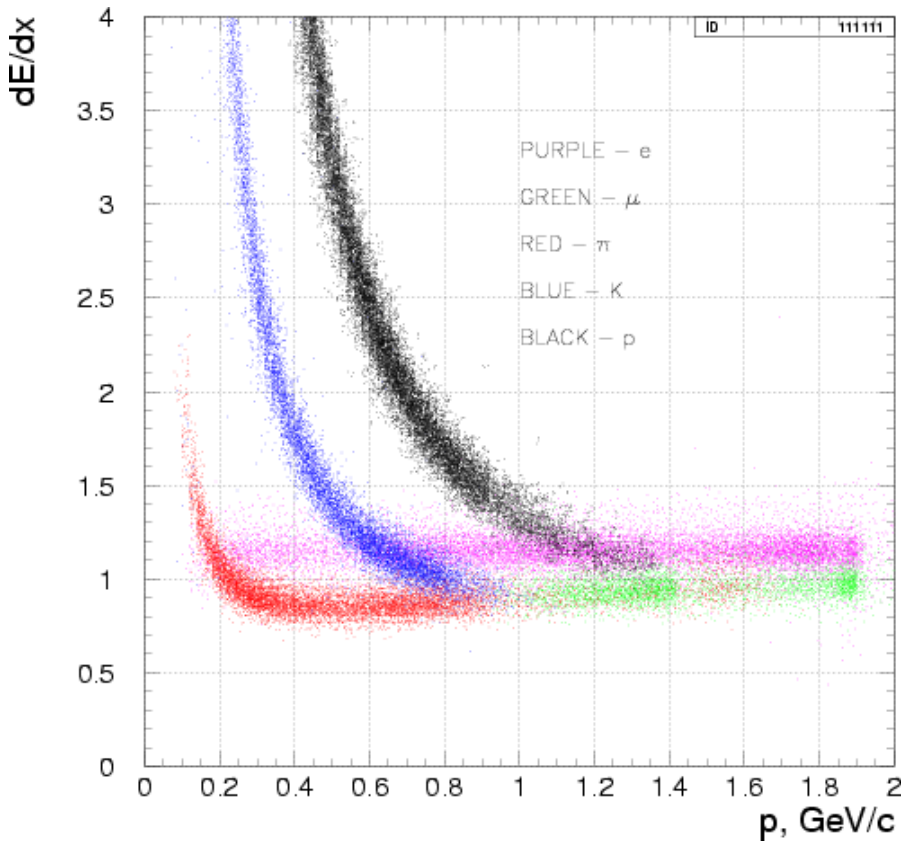

Figure 3.1: Energy loss (dE/dx) in the CLEO-c detector as a function of momentum for different particle types. The horizontal, purple band is for electrons. The three bands spiking at low momentum are, from left to right, pions (red), kaons (blue), and protons (black). The horizontal, green band in the bottom right is for muons. Note that the pion and kaon bands overlap at high momentum.

The combined particle identification system (dE/dx and RICH) identifies pions and kaons with efficiency greater than 95%, and mis-identification rates are on the order of 1%.

3.1.3 Electromagnetic Shower Reconstruction

Electromagnetic showers are formed from energy clusters spread over multiple crystals in the calorimeter. The shower position is determined by interpolating between crystals, and the total energy is determined by summing the crystals.

A small fraction of the crystals in the calorimeter are known to be noisy or to have poor performance; those crystals are ignored.

The shape of a cluster and its relation to any nearby tracks provides information about the source of the shower. The most obvious case is where the path of a track intersects the location of the shower. In this case the shower is almost certainly produced by the charged particle, and so it is not considered a photon candidate. A more subtle piece of information is the shower shape. Electromagnetic showers tend to be narrower than hadronic showers in the calorimeter, and so photon candidates are required to have relatively narrower showers. "Narrowness" is measured by a quantity called $E9/E25$; this is the ratio of the energy in a 3×3 block of crystals around the cluster center to the energy in a 5×5 block. For photons $E9/E25$ should be close to one.

Still more subtle is the relationship of a cluster to a nearby track that is not close enough to be considered "matched". Hadronic interactions in the calorimeter may produce secondary particles ("split-offs") that travel some distance before depositing energy in more distant crystals. These energy deposits produce false photon candidates, and requirements have been developed to identify and remove many of these split-off showers. However, these requirements are less commonly used than the track-matching and cluster shape requirements, and in this dissertation they are not used unless mentioned other-

wise.

3.2 Reconstruction of Decayed Particles

The general strategy for finding a short-lived particle undergoing a particular decay is to, in each event, simply try all possible combinations of decay daughters. False combinations are then reduced by kinematic requirements. The most common kinematic requirement is based on the relativistic equation

$$m^2 = E^2 - p^2 \tag{3.1}$$

where m is a particle's mass, E is its energy, and p is its momentum.[2] For any combination of daughter candidates, the invariant mass is formed by summing their energy and vector momentum and using these sums in Eq. 3.1:

$$m = \sqrt{\left(\sum_i E_i\right)^2 - \left(\sum_i \mathbf{p}_i\right)^2} \tag{3.2}$$

where E_i and $\mathbf{p}_i$ are the energy and momentum of the ith daughter candidate. For a correct combination of daughter candidates, this invariant mass will be consistent with the parent particle's mass. For incorrect combinations (the "combinatoric background"), the invariant mass will typically be far from the correct mass. Therefore, the number of false combinations may be reduced by requiring an invariant mass near the decaying particle's mass.

For example, to reconstruct $\pi^0 \to \gamma\gamma$, we test all pairs of photons (*i.e.*, showers passing photon selection requirements). Pairs whose invariant mass is not consistent with the π^0 mass are rejected. To reconstruct $D^0 \to K^-\pi^+\pi^0$, we test all

[2]Here, factors of the speed of light c are suppressed, so m refers to mc^2 and p refers to pc; c will be suppressed throughout this dissertation.

combinations of a K^- candidate (negatively-charged track identified as a kaon), a π^+ candidate (positively-charged track identified as a pion), and a π^0 candidate (pair of photons whose invariant mass is consistent with the π^0 mass).

3.2.1 π^0 Reconstruction

Almost 99% of π^0s decay into two photons [1]. Therefore π^0 candidates are formed from pairs of photons. These photons must pass the requirements described in Section 3.1.3 and must also have an energy greater than 30 MeV. The invariant mass of the photons is calculated under the assumption that they originated at the center of the detector. An uncertainty σ is also calculated for this mass; the uncertainty varies with the location, energy, and shape of the two showers, and it is typically 5-7 MeV. The π^0 candidate is rejected if its invariant mass is more than 3σ from the true π^0 mass.

Each valid π^0 candidate is then passed through a kinematic fit. This fit adjusts the photon directions and momenta within their uncertainties to place their invariant mass at the true π^0 mass. The π^0 is then assigned the momentum and energy determined from the fit. These parameters are used for all later analysis.

3.2.2 K^0_S Reconstruction

The K^0_S meson is unusual in that, while it does decay inside the detector, the decay does not occur at the e^+-e^-interaction point. Instead, the K^0_S, with $c\tau \approx$ 2.7 cm [1], typically decays with a flight distance on the order of centimeters. The most common decay of the K^0_S, with a branching fraction of about 69%, is

to two charged pions [1]. This is the decay channel used to reconstruct the K_S^0. Therefore, the signature of a K_S^0 is a pair of oppositely-charged tracks sharing a common vertex typically located some distance from the interaction point.

The tracks used to form a K_S^0 candidate are not subject to the track quality or particle identification requirements described above. Each pair of oppositely-charged tracks is subjected to a vertex fit, and if a vertex is found the track parameters from the fit are used to calculate the invariant mass. Candidates whose mass is within 12 MeV of the true K_S^0 mass are accepted. For most analyses, including those described in this dissertation, the vertex and mass requirements are sufficient for reducing combinatoric background. The parameters from the vertex fit are used in all later analysis; no mass constraint is imposed.

3.2.3 D Reconstruction

Candidates for D^0 and D^+ mesons are formed by combining charged particles, π^0 candidates, and K_S^0 candidates according to the D decay mode being reconstructed. In forming these candidates, we must be sure not to use any track or shower more than once (for instance, by using a track in a K_S^0 candidate and as a kaon candidate). The energies and momenta of these particles are summed to form the candidate's energy and momentum.

The kinematic constraints used to identify valid D candidates take advantage of the unique kinematics of e^+-e^-collisions just above $D\bar{D}$ threshold. In the center-of-mass frame,[3] the produced D and $\bar{D}$ are produced back-to-back with

[3] At CLEO-c, the laboratory reference frame is nearly equal to the center-of-mass frame. However, the e^+-e^-system does have a small non-zero momentum in the lab frame due to the crossing angle between the e^+ and e^- beams. For the analysis described in this section, we ignore this

equal energies and momenta; these can be calculated from the energy of the e^+-e^-collision. Therefore, we impose separate requirements on the candidate's energy and momentum, instead of a single requirement on the invariant mass (which is a variable depending on energy and momentum). The actual requirements are on two kinematic variables related to energy and momentum – ΔE and beam constrained mass ($M_{\rm BC}$).

The first kinematic variable, related to energy, is

$$\Delta E \equiv E - E_{\rm tot}/2 \tag{3.3}$$

where E is the candidate energy and $E_{\rm tot}$ is the total energy of the initial e^+ and e^-. Since the D and $\bar{D}$ each carry half of the total energy, ΔE will be consistent with zero for a true D candidate.

The second kinematic variable, related to momentum, is

$$M_{\rm BC} \equiv \sqrt{(E_{\rm tot}/2)^2 - p^2} \tag{3.4}$$

where p is the candidate momentum. $M_{\rm BC}$ is just the invariant mass with the known D energy, $E_{\rm tot}/2$, substituted for the candidate energy. For a true D^0 (D^+) candidate, $M_{\rm BC}$ will be consistent with the D^0 (D^+) mass. Alternatively, $M_{\rm BC}$ may be thought of as a function of momentum which, unlike the raw momentum, peaks at the same value regardless of beam energy.

Figure 3.2 shows a representative plot of ΔE vs. $M_{\rm BC}$. The true D candidates are clustered near $\Delta E = 0$, $M_{\rm BC} = M_D$.

A clean sample of D candidates may be selected by applying requirements on both ΔE and $M_{\rm BC}$. Typically these requirements vary according to the decay

small distinction. However, when analyzing data the energy and momentum values measured in the lab are in fact corrected for this boost into the center-of-mass frame.

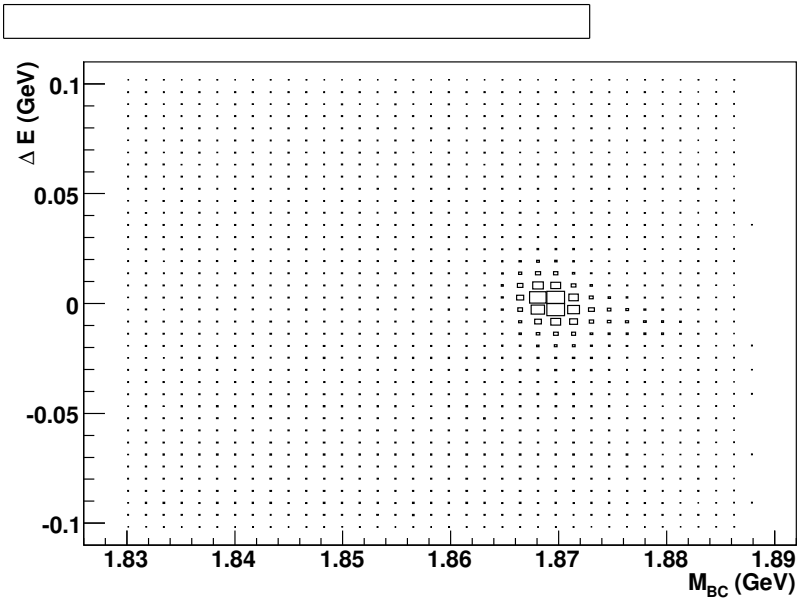

Figure 3.2: Plot of ΔE vs. $M_{\rm BC}$ for decay mode $D^+ \to K^-\pi^+\pi^+$.

mode being reconstructed.

3.3 Inferring Invisible Particles

At first it would appear impossible to reconstruct a particle if it leaves no clear signature in the CLEO detector. However, it is in fact possible if every other particle in the event can be reconstructed. The initial four-momentum of the e^+-e^-system is known, and because it is conserved it must equal the total four-momentum of the final-state particles. When only one of these particles is missing, its four-momentum can be calculated:

$$p_{\rm miss} = p_{\rm tot} - \sum_i p_i \tag{3.5}$$

Here, $p_{\rm tot}$ is the initial e^+-e^-four-momentum, p_i are the four-momenta of the reconstructed particles, and $p_{\rm miss}$ is the missing particle's four-momentum.

The existence of a given missing particle can be inferred from the missing mass squared, which is the square of the missing four-momentum:

$$M^2_{\text{miss}} \equiv p^2_{\text{miss}} = E^2_{\text{miss}} - \mathbf{p}^2_{\text{miss}} \tag{3.6}$$

If an event truly contained the reconstructed particles and an unfound particle X, M^2_{miss} will be consistent with M^2_X, the square of the mass of X.

To find a missing particle X, we first identify a physical process in which we will search for it. We then look for all particles in that process except for X. For each combination of candidates, we calculate M^2_{miss}. The distribution of M^2_{miss} over many events will contain a peak at M^2_X for events in which X was indeed the one missing particle; other events form a background that in general does not peak at M^2_X.

CHAPTER 4

MEASUREMENT OF TRACKING AND K_S^0 EFFICIENCIES

4.1 Introduction

To determine how many events of a certain signal type (say, a particular D decay mode) were produced in a given run period at CLEO-c, we must determine two types of quantities – yields and efficiencies. To determine a yield, in each recorded event we attempt to reconstruct the final state according to selection requirements, which we design to eliminate background events while retaining signal events. We then count the number of events passing these requirements. Second, we need to determine the efficiency for reconstructing a given final state according to these requirements. To determine efficiencies, we use Monte Carlo simulations.

A Monte Carlo simulation begins with the physics of the e^+-e^-collision – the production of particles in the e^+-e^-collision (typically D and $\overline{D}$) and the decay of the intermediate particles into the final-state particles. Decays are simulated accounting for branching fractions into different decay modes and for the angular distributions of daughter particles in those decays. This step of the simulation is performed by the EvtGen software package [10]. The output of EvtGen is a set of final-state particles and their momenta. Final-state radiation from these particles is simulated with PHOTOS [11].

The next simulation step is to propagate these particles through the detector volume and to model the signatures they leave in the active detector elements (drift chamber wires, calorimeter crystals, etc.). This simulation is performed by GEANT [12]. It accounts for physical effects such as particle decays in flight, interactions with detector material, and energy loss due to bremsstrahlung.

Finally, we simulate the response of the CLEO-c detector electronics and data

acquisition, and produce data in the same format that is produced for real data. The simulated data is then run through the same analysis code as the real data.

To determine the efficiency for reconstructing a given final state, we begin by generating Monte Carlo in which EvtGen is constrained to produce only that final state. (This is referred to as "signal Monte Carlo.") We then subject the output of the simulation to the same analysis requirements as data. The efficiency is calculated as the number of events passing these requirements divided by the number of events generated.

To accurately measure a branching fraction or any other quantity requiring knowledge of efficiencies, it is critical that the Monte Carlo simulation is accurate (or that any inaccuracy is well-understood and well-measured). While we make every effort to include all known physical effects and to accurately describe the detector geometry, inevitably the simulation contains compromises and uncertainties. Therefore it is important to check whether the output of the simulation matches data, and to quantify any difference and its uncertainty.

In this chapter, we compare the efficiencies for reconstructing a single track or K^0_S in data and in the Monte Carlo simulation. We will find no measurable difference between efficiencies in data and Monte Carlo, and we will evaluate the uncertainty on the difference to generate systematic uncertainties for use in other CLEO-c analyses.

4.2 Theoretical Expectations for Efficiencies

4.2.1 Sources of Tracking Inefficiency

Before describing the measurements of tracking efficiency, we consider what causes a track to not be reconstructed. A previous study of tracking efficiency for high-momentum muons showed an efficiency of nearly 100% in both data and Monte Carlo [13]. Pions and kaons, on the other hand, do show some inefficiency. The crucial difference is that muons almost never decay or interact inside the detector, but pions and kaons sometimes do. The muon efficiency measurements suggest that when a track passes through the entire drift chamber, the efficiency for reconstructing it is nearly 100%. The only way a track can be lost is if it decays or interacts inside the drift chamber.

In the Monte Carlo simulation, we can examine the dependence of tracking efficiency on decay location and other parameters by using Monte Carlo truth matching. We look at all K^+s and K^-s in the simulated decay tree that are produced near the interaction point and that are directed toward the barrel section of the detector ($|\cos\theta| < 0.7$). Then we ask, for each kaon, whether it has a truth-matched reconstructed track. To match the track quality requirements, we require that the best-matched track have hits in at least half of the detector layers traversed by its helix. The fraction of kaons which have such a match is (approximately) the tracking efficiency.

We first plot, in Fig. 4.1, efficiency as a function of the transverse distance (i.e. distance from the beampipe) at which the kaon died through decay or interaction. The drift chamber extends to a radius of 0.8 m. For tracks that pass

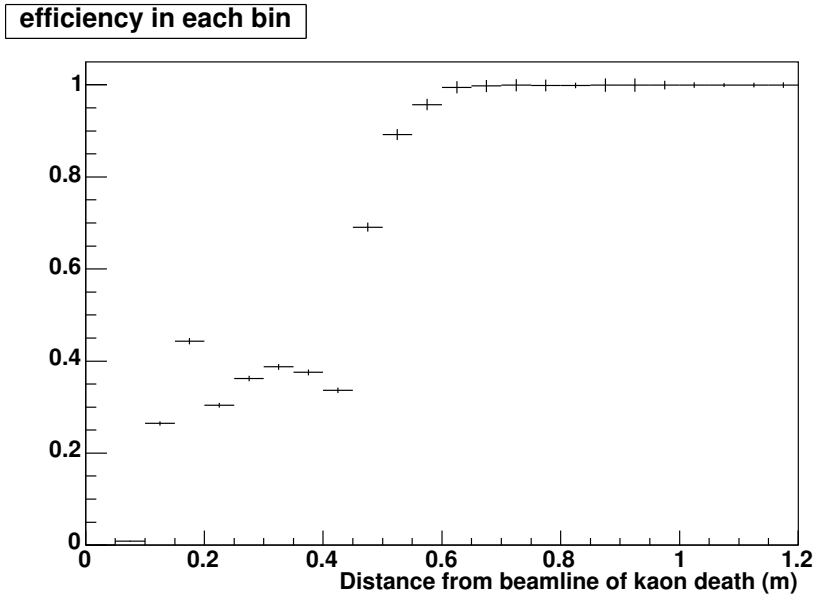

Figure 4.1: Kaon tracking efficiency in the Monte Carlo simulation as a function of the transverse distance at which the kaon decayed or interacted. The structure around 0.2m corresponds to the boundary between the ZD and DR drift chambers. The outer radius of the drift chamber is 0.8m.

through the entire chamber before decaying (*i.e*,, that decay at a radius greater than 0.8 m), the tracking efficiency is 100%. Even for decays inside the chamber at a radius of 0.6m or higher, the efficiency is very close to 100%. As suggested by the muon studies, a track can be lost only if it dies inside the drift chamber. For these tracks, the efficiency is most strongly affected by the requirement that a track contain hits in at least half of the drift chamber layers traversed by its helix. Efficiency drops sharply at a radius of approximately 0.4 m, half the drift chamber radius. A charged particle may be found when it decays inside this radius if its charged decay product produces hits in additional layers; in this case a track can be found but its momentum resolution is poor.

The transverse momentum P_T of a track affects the reconstruction efficiency,

but this dependence is primarily caused by the relationship of P_T to the transverse death distance of the track. Lower-momentum tracks are more likely to decay inside the detector, so their efficiency is lower. For a given death distance, the dependence on transverse momentum is weak. The left column Figure 4.2 shows efficiency as a function of P_T in bins of death distance. Within each bin, there is some dependence on P_T, but it is much weaker than the dependence on death distance.

We might also expect the number of tracks in an event to affect the reconstruction efficiency of a particular track. With more tracks, the noisier environment would make it more difficult to reconstruct a particular track. The right column of Figure 4.2 shows efficiency as a function of the number of reconstructed tracks in bins of death distance. While there is some dependence on track multiplicity, again the dominant effect is from the death distance.

These studies tells us that, according to the Monte Carlo simulation, the only way a track can be lost is if the particle dies before reaching the edge of the drift chamber. If this happens, it might still be found, and the probability depends strongly on the decay distance and less strongly on momentum and multiplicity. As a corollary, high-momentum tracks will have higher efficiency than low-momentum tracks. Also, kaons will have lower efficiency than pions; they are more likely to decay inside the drift chamber because their lifetime is shorter and because their higher mass gives them a smaller relativistic boost at a given momentum.

Another way that we may fail to find a track, not covered by this study of efficiency as a function of death distance, is for the particle to emit final state radiation. In this case, a track may very well be found, but it will not have the

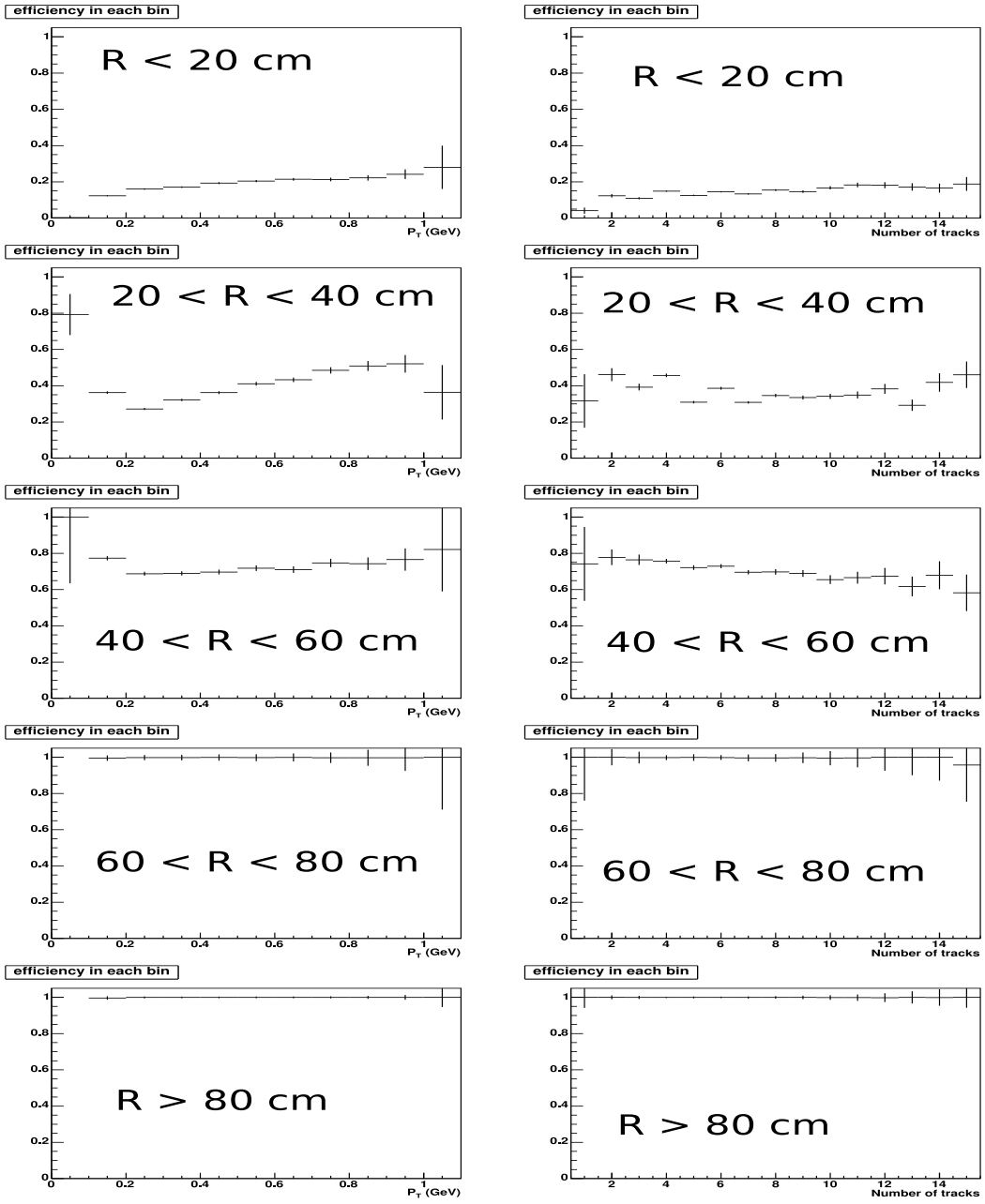

Figure 4.2: Dependence of kaon tracking efficiency in the Monte Carlo simulation on transverse momentum (left column) and track multiplicity (right column) in bins of the kaon's transverse death distance R. The drift chamber extends to a radius of about 80 cm. The dependence of tracking efficiency on transverse momentum and track multiplicity is much weaker than the dependence on death distance.

expected momentum because the radiated photon carried some of the momentum away. We count this as an inefficiency when the radiated energy is large enough that the track fails to form a suitable D candidate when combined with the other D decay products. This is the correct procedure when measuring a tracking systematic for use in D decays. Typically, less than 1% of tracks emit enough final state radiation that they fail to form a good D candidate. Final state radiation is included in the Monte Carlo simulation.

4.2.2 Sources of K^0_S Inefficiency

Reconstruction of a $K^0_S \to \pi^+\pi^-$ candidate requires finding a pair of oppositely-charged tracks that intersect to form a vertex. The easiest way to miss a K^0_S decay to charged pions is for one of the pion tracks to not be found. If the tracks are found, it is very likely that the K^0_S candidate will be found. The main exception is when one of the tracks is poorly measured, leading to a failure of the vertex finder or a failure of the K^0_S mass requirement.

To separate the effects of tracking efficiency from the rest of the K^0_S reconstruction process, we measure the K^0_S efficiency for events in which the two pion tracks were successfully reconstructed. Then the overall K^0_S reconstruction systematic is formed by combining the systematic on this K^0_S efficiency with the tracking systematic for the two pions.

4.3 Overview of Procedure

Our method for measuring efficiencies takes advantage of the technique described in Section 3.3 for inferring the presence of a particle without actually reconstructing it. We fully reconstruct all particles in an event, except for one particle whose efficiency we wish to measure. We identify correct reconstructions of these particles, with the correct missing particle, from a peak in the missing mass squared at the missing particle's mass squared. We then search for the missing particle, and the efficiency is the fraction of events in the missing mass squared peak for which it is found.

Efficiencies in data are measured in $D\bar{D}$ events, and efficiencies in Monte Carlo are measured with a corresponding generic Monte Carlo sample; in this sample $D\bar{D}$ events are produced and the Ds are allowed to decay generically. To measure the various efficiencies, we first reconstruct a tag $\bar{D}$. Then, we choose a D decay that includes the particle whose efficiency we wish to measure, and we reconstruct all of the other particles in that decay. We form the missing mass squared ($M^2_{\rm miss}$) from these particles and the tag $\bar{D}$. Then we look for the missing particle and separate the $M^2_{\rm miss}$ distribution into events where that particle was and was not found. Peaks in these distributions at the missing particle's mass squared give the number of times we did and did not find it. We perform fits to determine the peak yield in both distributions, and from these numbers we calculate the efficiency.

We measure tracking efficiencies for charged pions and kaons in the decays $D^0 \to K^-\pi^+$, $D^0 \to K^-\pi^+\pi^0$ (kaons only), and $D^+ \to K^-\pi^+\pi^+$. For K^0_S efficiency, we use the decay $D^0 \to K^0_S\pi^+\pi^-$. In the three-body modes, efficiency measurements

are performed separately in various bins of momentum and flight direction.

In each sample, we measure the efficiency in both data and Monte Carlo, and compute the data-Monte Carlo discrepancy $\epsilon_{\mathrm{MC}}/\epsilon_{\mathrm{data}} - 1$. This discrepancy is the correction that should be applied for tracking or K^0_S efficiency. For tracking efficiency, we will combine these measured discrepancies, using the procedure described in Section 4.10, to determine efficiency systematics for pions and kaons. For K^0_S efficiency, we calculate a single discrepancy to determine the K^0_S efficiency systematic.

4.4 Calculation of Efficiency and Uncertainty Analysis

The efficiency ϵ is calculated from the number of events in which the missing particle is found ("efficient"), denoted E, and the number in which it is not found ("inefficient"), denoted I:

$$\epsilon \equiv \frac{E}{E+I} = \frac{1}{1+I/E} \tag{4.1}$$

Given uncertainties of δE and δI, the uncertainty on the efficiency is

$$\begin{aligned} \delta\epsilon &= \frac{1}{(E+I)^2}\sqrt{E^2(\delta I)^2 + I^2(\delta E)^2} \\ &= \epsilon(1-\epsilon)\sqrt{\left(\frac{\delta E}{E}\right)^2 + \left(\frac{\delta I}{I}\right)^2} \end{aligned} \tag{4.2}$$

This is the expression used to calculate the efficiency uncertainties in the tables throughout this chapter.

The relative uncertainty on the efficiency, which is the relevant quantity for determining the size of an efficiency systematic $\epsilon_{\mathrm{MC}}/\epsilon_{\mathrm{data}} - 1$, is

$$\frac{\delta\epsilon}{\epsilon} = (1-\epsilon)\sqrt{\left(\frac{\delta E}{E}\right)^2 + \left(\frac{\delta I}{I}\right)^2} \tag{4.3}$$

The efficiencies we will measure are relatively large: ~97% for pions, ~85% for kaons, and ~94% for K^0_Ss. Thus, the factor $(1-\epsilon)$ will be small, which reduces our relative uncertainties.

We now consider some approximations to explore the sensitivity of our measurement to various quantities and uncertainties. The relative error on the inefficient events I will be much larger than the relative error on the efficient events E because there are fewer inefficient events and because (as shown below) there is more background for these events. Therefore, to a good approximation $(\delta E/E)^2$ is negligible, and

$$\frac{\delta\epsilon}{\epsilon} \approx (1-\epsilon)\left(\frac{\delta I}{I}\right) \tag{4.4}$$

The efficiency systematic correction is the deviation from one of the Monte Carlo-data efficiency ratio: $\epsilon_{\mathrm{MC}}/\epsilon_{\mathrm{data}} - 1$. We will find that this correction is consistent with zero. Its uncertainty, which sets the size of the tracking systematic, is approximately

$$\delta(\epsilon_{\mathrm{MC}}/\epsilon_{\mathrm{data}} - 1) \approx \frac{\epsilon_{\mathrm{MC}}}{\epsilon_{\mathrm{data}}}\sqrt{\left[(1-\epsilon_{\mathrm{MC}})\left(\frac{\delta I_{\mathrm{MC}}}{I_{\mathrm{MC}}}\right)\right]^2 + \left[(1-\epsilon_{\mathrm{data}})\left(\frac{\delta I_{\mathrm{data}}}{I_{\mathrm{data}}}\right)\right]^2} \tag{4.5}$$

Assuming that the uncertainties in data are much larger than those in Monte Carlo and that $\epsilon_{\mathrm{MC}} = \epsilon_{\mathrm{data}} \equiv \epsilon$,

$$\delta(\epsilon_{\mathrm{MC}}/\epsilon_{\mathrm{data}} - 1) \approx (1-\epsilon)\left(\frac{\delta I_{\mathrm{data}}}{I_{\mathrm{data}}}\right) = \frac{\delta I_{\mathrm{data}}}{E_{\mathrm{data}} + I_{\mathrm{data}}} \tag{4.6}$$

We see that the scale of the efficiency systematic is determined by the uncertainty on the inefficient yield in data, as a fraction of the total number of missing particles considered. The systematic is relatively insensitive to variations in the efficient yield.

4.5 Data and Monte Carlo Samples

An 818 pb^{-1} sample of e^+-e^-collisions at the $\psi(3770)$ resonance, containing approximately 5 million $D\bar{D}$ events, is used to measure the efficiencies. Efficiencies in the simulation are measured in a generic Monte Carlo sample of simulated $D\bar{D}$ events, containing 20 times as many of these events as in data.

4.6 Event and Candidate Selection

In all of the selection criteria discussed below, charge conjugation is implicitly assumed. For example, reconstruction of a D^- and a π^+ implies an analogous treatment of D^+ and π^-.

The selection of π^+, π^0, K^+, K^0_S, D^0, and D^+ candidates uses standard selection requirements common to many CLEO-c analyses. These requirements were described in Chapter 3.

For the $\bar{D^0}$ reconstruction we use 3 decay modes: $\bar{D^0} \to K^+\pi^-$, $\bar{D^0} \to K^+\pi^-\pi^0$, and $\bar{D^0} \to K^+\pi^-\pi^+\pi^-$. We require the tag $\bar{D^0}$ to satisfy

$$|M_{\rm BC} - M_{D^0}| < 0.005 \text{ GeV},$$

$$|\Delta E| < 0.025 \text{ GeV},$$

where $M_{D^0} = 1.8645$ GeV [1]. Next we combine the $\bar{D^0}$ tag candidate with one of the following:

- K^- (to measure efficiency for the π^+ in $K^-\pi^+$)
- π^+ (to measure efficiency for the K^- in $K^-\pi^+$)

- π^+ and π^0 (to measure efficiency for the K^- in $K^-\pi^+\pi^0$)
- π^+ and π^- (to measure efficiency for the K^0_S in $K^0_S\pi^+\pi^-$)

For the D^- reconstruction we use 6 decay modes: $D^- \to K^+\pi^-\pi^-$, $D^- \to K^+\pi^-\pi^-\pi^0$, $D^- \to K^0_S\pi^-$, $D^- \to K^0_S\pi^-\pi^0$, $D^- \to K^0_S\pi^-\pi^-\pi^+$, and $D^- \to K^+K^-\pi^-$. We require

$$|M_{\rm BC} - M_{D^+}| < 0.005 \text{ GeV},$$

$$|\Delta E| < 0.025 \text{ GeV},$$

where $M_{D^+} = 1.8694$ GeV [1]. We combine the D^- candidate with one of the following:

- a pair of π^+s (to measure efficiency for the K^- in $K^-\pi^+\pi^+$)
- K^- and π^+ (to measure efficiency for the π^+s in $K^-\pi^+\pi^+$)

For each of these candidates the missing mass squared is calculated:

$$M^2_{\rm miss} = (p_{\rm tot} - p_{\bar{D}} - p_{\rm other})^2 \tag{4.7}$$

Here, $p_{\rm tot}$ is the four-momentum of the e^+e^- pair, $p_{\bar{D}}$ is the four-momentum of the tag $\bar{D}$, and $p_{\rm other}$ is the four-momentum of the other particles that were combined with the tag $\bar{D}$. We expect a peak at m^2_π if a pion was missing, m^2_K if a charged kaon was missing, or $m^2_{K^0_S}$ if a K^0_S was missing. In the missing mass squared calculation, we constrain the beam constrained mass of the tag $\bar{D}$ to the known $\bar{D}$ mass. That is, we rescale its momentum magnitude to the expected value based on the beam energy, but leave its direction unchanged. This constraint improves the $M^2_{\rm miss}$ resolution.

For K^0_S efficiency only, we introduce additionaly requirements to factor out tracking efficiency from the measurement. To remove events in which one or

both tracks from a K_S^0 were not found, we require that the remaining unused tracks in the event contain at least one pair of oppositely charged tracks loosely consistent with the hypothesis of a missing K_S^0. The track parameters are evaluated at the e^+-e^-interaction point and not at the K_S^0 decay vertex, and so for true K_S^0s the resolution on the momentum and invariant mass of the pair will be poor. The requirements for the pair of tracks are that the invariant mass must satisfy $0.3 < M(2\text{ tracks}) < 0.7$ GeV, and that the vector difference between the pair's momentum and the predicted K_S^0 momentum (based on the other particles in the event) must be less than 60 MeV. This requirement is approximately the resolution of the momentum for events in which the K_S^0 was found – see Figure 4.3. Events which do not contain a suitable pair of tracks are removed. In addition to removing $D^0 \to (K_S^0 \to \pi^+\pi^-)\pi^+\pi^-$ events in which one or both K_S^0 daughter pions were not found, this requirement eliminates $D^0 \to K_L^0\pi^+\pi^-$ and $D^0 \to (K_S^0 \to \pi^0\pi^0)\pi^+\pi^-$ events, both of which would also peak at the K_S^0 mass squared. It also removes many non-peaking backgrounds. With the requirement that a pair of suitable tracks was found, it is expected that the K_S^0 efficiency is near 100%. Essentially, all that is being measured is whether the found tracks were sufficiently well-measured to form a good K_S^0 vertex with the proper invariant mass.

We next consider, for tracking efficiency, all remaining tracks that pass the track quality requirements, ignoring particle identification requirements. For K_S^0 efficiency, we consider all K_S^0 candidates that do not overlap the particles used in forming M^2_{miss} and that pass the 12 MeV mass requirement. In each case we loop over the track or K_S^0 candidates to search for the missing particle. If we find this particle such that it forms a good D candidate when combined with the other D decay products, we have found the missing particle. The criteria for

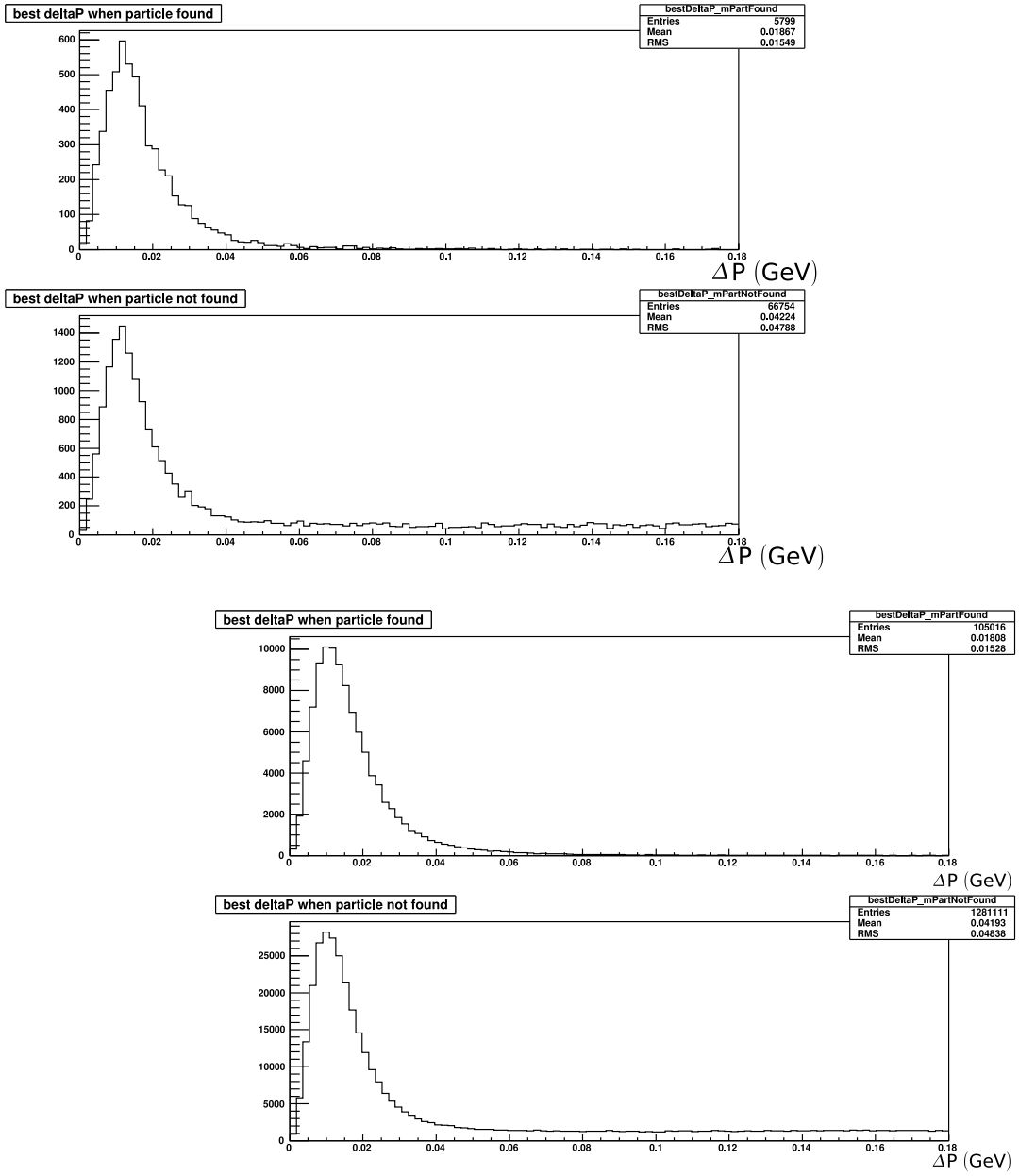

Figure 4.3: Distributions of each missing mass candidate's best $\Delta P \equiv |\vec{P}_{2\text{ tracks}} - \vec{P}_{\text{predicted}}|$. The top left pair of plots is for data and the plots to the bottom right are for the Monte Carlo simulation. The top plot in each pair shows the ΔP distribution when a K_S^0 was found. The bottom plot in each pair shows the distributon for the events where no K_S^0 was found. These bottom plots include background events in which no K_S^0 was present at all; in fact they include more background than is shown in later plots because they include a wider M^2_{miss} range. In this analysis, we require $\Delta P < 0.060$ GeV.

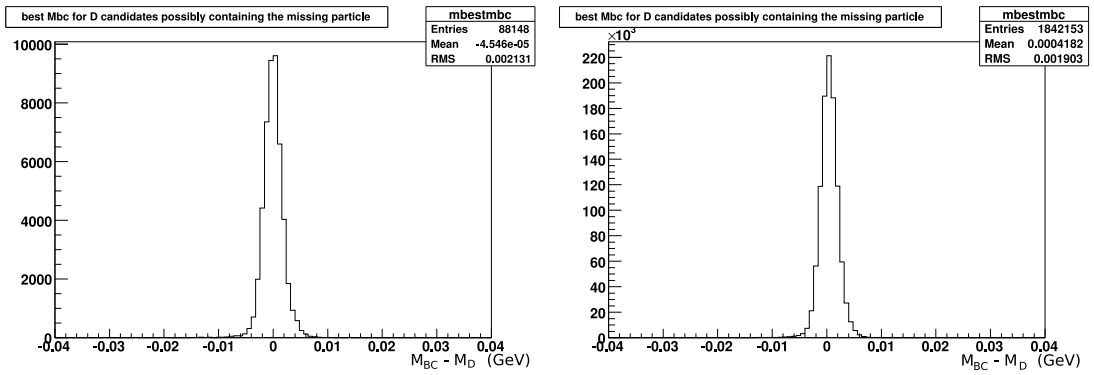

Figure 4.4: For each event, value of $M_{\rm BC} - M_D$ closest to zero. Data is on the left, and the Monte Carlo simulation is on the right. In this example, the missing particle is the π^+ in $D^+ \to K^-\pi^+\pi^+$; other modes are similar. The requirement used to determine whether the π^+ was found is $|M_{\rm BC} - M_D| < 0.01$GeV, wide enough to include the entire peak.

good D candidate is that

$$|M_{\rm BC} - M_D| < 0.01\text{GeV},$$

$$|\Delta E| < 0.05\text{GeV}.$$

If no good D candidate is found, then we did not find the missing particle. These requirements are chosen to be loose, so that a track is considered found even if its momentum is poorly measured. Figure 4.4 shows an example of the distribution of $M_{\rm BC} - M_D$. The accepted range is wide enough to include the entire peak, and no background is present, so our results are insensitive to this exact value of this requirement.

To determine background for the K^0_S efficiency study, we also consider K^0_S candidates in low and high sidebands of the K^0_S mass. These sidebands are defined to be 14-26 MeV from the K^0_S mass on either side. The sidebands are used to study how often fake K^0_S candidates are produced from random combinations of tracks. The mass distribution of fake K^0_S candidates does not peak in

the K_S^0 mass, so fakes that pass the 12 MeV mass requirement are well modeled by fakes with masses in the sidebands. The only difference is that their missing mass squared distributions will be shifted left or right, as discussed in Section 4.11.1.

Additionally, we split the candidates into bins of $|\cos\theta|$ and momentum according to the missing momentum. For the kaon and pion in $D^0 \to K^-\pi^+$, we consider only those candidates with $|\cos\theta| < 0.9$. Higher values of $|\cos\theta|$ are ignored because the $|\cos\theta|$ spectrum is cut off near 1 since the kaon and pion are nearly back-to-back. In the three-body tracking modes this spectrum is not cut off in this way, so we do use a bin with $|\cos\theta| \geq 0.9$ and $p \geq 0.2$GeV; this bin has low efficiency because the missing particle often goes down the beampipe. In the three-body tracking modes the pion and kaon candidates with $|\cos\theta| < 0.9$ are split into 5 momentum bins. For K_S^0 efficiency, we do not divide into angular bins. We study K_S^0 efficiency in four momentum bins, and with all bins combined.

4.7 Fits for Yields and Efficiencies

The distributions of M^2_{miss} are divided into the case of finding the missing particle (π^+, K^+, or K_S^0) and not finding it. We perform unbinned maximum likelihood fits to both of these distributions to extract the yields in the M^2_{miss} peak for the two cases. The efficiency is calculated from these yields.

Events where the missing particle was found have a clean M^2_{miss} peak at the particle mass squared. For pions and kaons this peak is free of background; for K_S^0s there is a small peaking background from fake K_S^0 candidates. The signal

peak, which represents the "efficient" events, is fit with a two-sided Crystal Ball shape [14].[1] This peak shape is a Gaussian core with longer power-law tails on each side.

Events in which the particle was not found are of two types: "inefficient" events in which the missing particle was present but not detected, and background events in which it was not present at all. The inefficient events form a peak at the particle mass squared. This peak should have the same shape as the peak in events where the particle was found. Therefore, the shape and position of the inefficient peak are fixed to match the efficient peak. The fit also includes one or more terms for the backgrounds. As will be clear below, the shapes of the background distributions are very different in different modes. Below, we discuss the backgrounds and how they are fit.

Fit parameters in data and Monte Carlo are always independent of each other, except in background shapes that are determined from signal Monte Carlo.

4.8 Pion Tracking Efficiency

4.8.1 Pion Efficiency from $D^0 \to K^-\pi^+$

In this section, we measure the pion tracking efficiency by looking for pions in the decay $D^0 \to K^-\pi^+$. Events with this decay correspond to a peak in M^2_{miss} at the pion mass squared.

[1] The two-sided Crystal Ball is implemented as a sum of two one-sided Crystal Balls, each with the same mean, width, and area but with tails on opposite sides.

Fits

Figure 4.5 shows the missing mass distributions and fits. When the pion track is not found, we observe a significant background. This background arises from the decay modes $D^0 \to K^- e^+ \nu_e$, $D^0 \to K^- \mu^+ \nu_\mu$, and $D^0 \to K^- \pi^+ \pi^0$. ($D^0 \to \pi^- \ell^+ \nu_\ell$ backgrounds are negligibly small; their efficiency is ~2% of the $D^0 \to K^- \ell^+ \nu_\ell$ efficiency.) All three of these backgrounds are modeled by error functions. The parameters that determine the locations and widths of these error functions are obtained by fitting Monte Carlo samples for these three modes, as shown in Figure 4.6. Also, we require that the backgrounds $D^0 \to K^- e^+ \nu_e$ and $D^0 \to K^- \mu^+ \nu_\mu$ have a fixed ratio determined by the efficiencies and branching fractions of these two decays. We also add a flat background term to absorb the small background at low $M^2_{\rm miss}$.

Fitting the generic Monte Carlo sample and the data to these backgrounds and the signal peak, we obtain the plots shown at the bottom of Figure 4.5. Note that the inefficient events produce a peak right at the threshold for $D^0 \to K^- \ell^+ \nu$.

Yields and Efficiencies

The yields and efficiencies from the fits are shown in Table 4.1.

Unfortunately, this measurement suffers from a background that turns on underneath the signal peak for inefficient events. Thus, we consider systematics for the background shapes due to possible differences in the background shapes between data and Monte Carlo. We evaluate this by redoing the fit to data (but not Monte Carlo) with two different variations on the error function parameters for $D^0 \to K^- e^+ \nu_e$, $D^0 \to K^- \mu^+ \nu_\mu$, and $D^0 \to K^- \pi^+ \pi^0$. We first increase the width

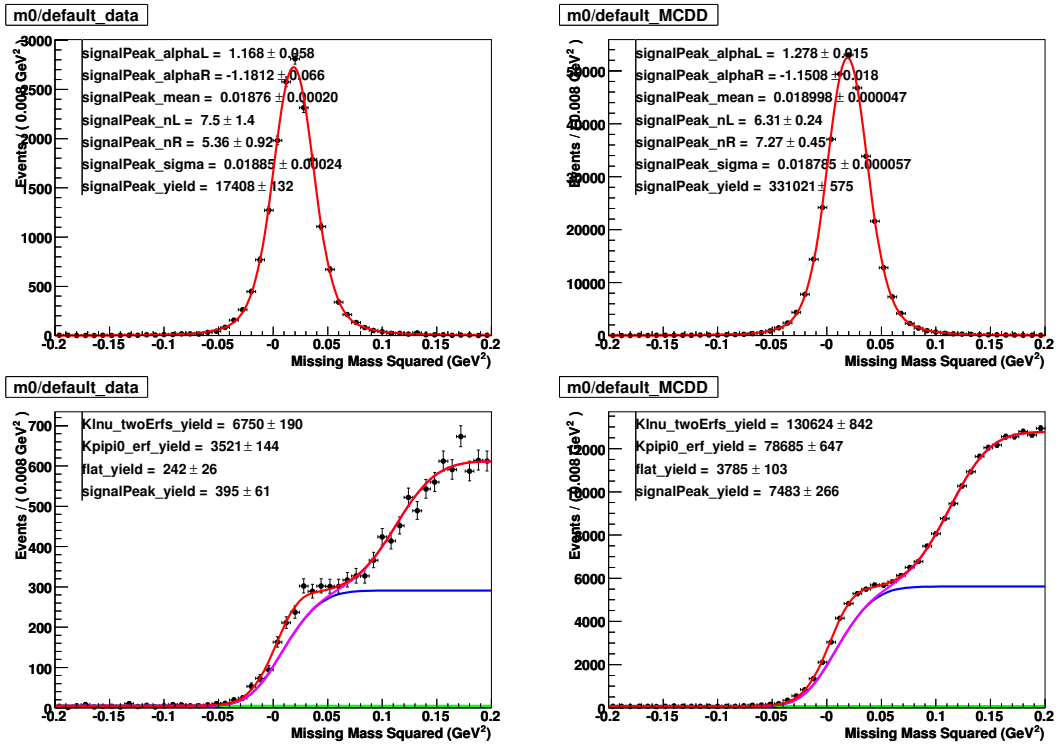

Figure 4.5: Pion efficiency from $D^0 \to K^-\pi^+$. The left plots are for data and the plots to the right are for the generic Monte Carlo simulation. The top row of plots shows a fit to the missing mass squared distribution when the pion was found. The bottom row of plots shows the distributon for the events where the pion was not found.

Table 4.1: Pion yields and tracking efficiencies from $D^0 \to K^-\pi^+$. The systematic uncertainty accounts for the uncertainty in the background shapes.

	Data	Monte Carlo
Number found	17408 ± 132	331021 ± 575
Number not found	395 ± 61 ± 9.22	7483 ± 266
Efficiency (%)	97.78 ± 0.34 ± 0.05	97.79 ± 0.08
$\epsilon_{MC}/\epsilon_{data} - 1$	+0.01 ± 0.35 ± 0.05 % (+0.0 σ)	

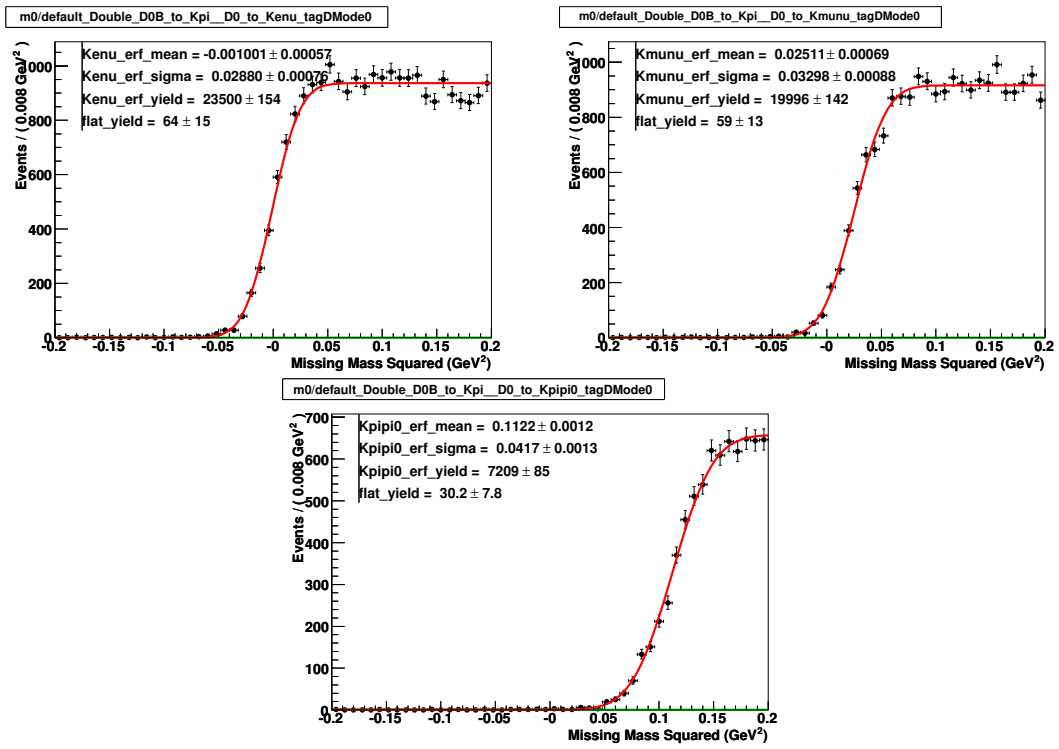

Figure 4.6: Fits to Monte Carlo samples for the modes $D^0 \to K^-e^+\nu_e$, $D^0 \to K^-\mu^+\nu_\mu$, and $D^0 \to K^-\pi^+\pi^0$, as analyzed while looking for events in which the pion in $D^0 \to K^-\pi^+$ was not found. The background shapes from these fits were used in the fits to data and generic Monte Carlo. The error function shapes for $D^0 \to K^-e^+\nu_e$ and $D^0 \to K^-\mu^+\nu_\mu$ are shifted with respect to each other due to the mass difference between the electron and muon.

of each error function by 10% and see how the inefficient yield changes. For the second variation, we shift the position of the error functions. The magnitude of the shift is determined by the difference between the positions of the efficient peaks in data and Monte Carlo (top of Figure 4.5); the difference and its uncertainty are combined in quadrature to determine the shift. With this shift, we see how the inefficient yield changes. The changes in the inefficient yield from these two variations are combined in quadrature to obtain the systematic uncertainty in Table 4.1.

Some other systematic variations in the fitting procedure were tested but turned out to be negligibly small. These variations were: widening the width of the inefficient peak in data by 10%, allowing the flat background component to have non-zero slope, and varying the background shape parameters within their uncertainties from the fits to the signal Monte Carlo samples.

4.8.2 Pion Efficiency from $D^+ \to K^-\pi^+\pi^+$

In this section, we measure the pion tracking efficiency by looking for pions in the decay $D^+ \to K^-\pi^+\pi^+$. Events with this decay correspond to a peak in $M^2_{\rm miss}$ at the pion mass squared. Since the momentum of the π^+ varies, we study the efficiency in the five momentum bins. We also study a bin of small polar angle.

Fits

The backgrounds in this mode are similar to those in $D^0 \to K^-\pi^+$, but with the addition of one extra π^+. $D^+ \to K^-\pi^+\pi^+\pi^0$ appears to the right of the signal peak, and the semileptonic decays $D^+ \to K^-\pi^+e^+\nu_e$ and $D^+ \to K^-\pi^+\mu^+\nu_\mu$ turn on under the signal peak. The fitting procedure is exactly the same as for $D^0 \to K^-\pi^+$, using the analogous background modes (each with an extra π^+).

Separate background shapes are determined in each momentum and angular bin.

Examples of plots for the background Monte Carlo samples are shown in Figure 4.7. Figures 4.8, 4.9, 4.10, 4.11, 4.12, and 4.13 show the plots for data and generic Monte Carlo in the 6 bins.

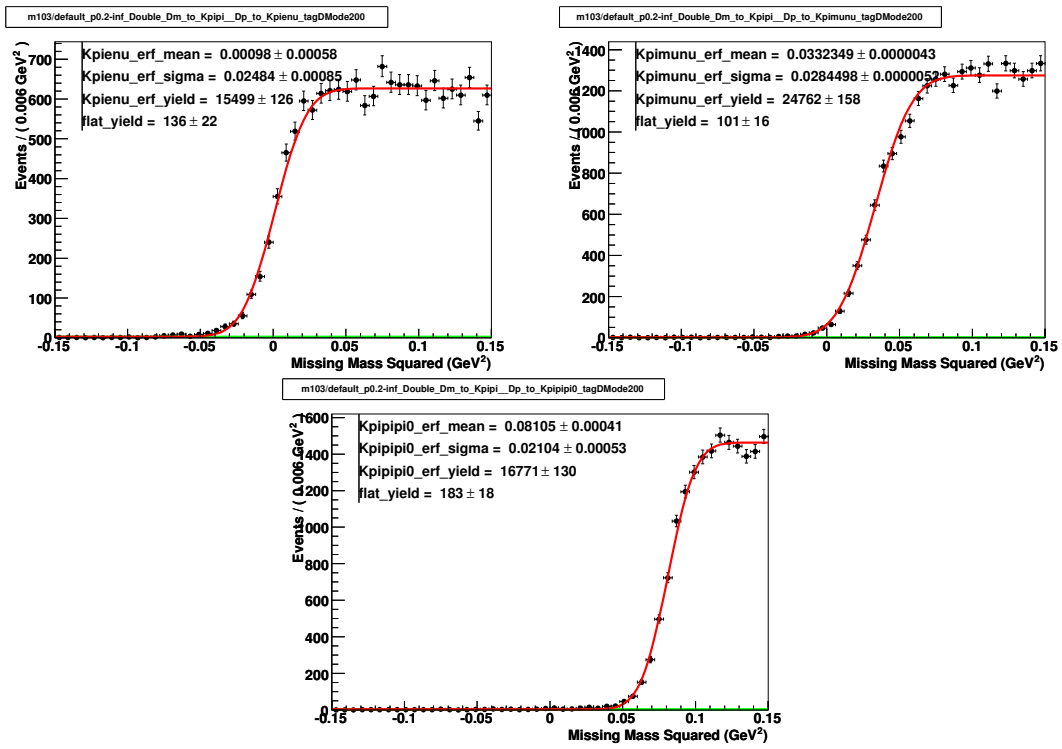

Figure 4.7: Fits to Monte Carlo simulations for the modes $D^+ \to K^-\pi^+e^+\nu_e$, $D^+ \to K^-\pi^+\mu^+\nu_\mu$, and $D^+ \to K^-\pi^+\pi^+\pi^0$, as analyzed while looking for events in which a pion in $D^+ \to K^-\pi^+\pi^+$ was not found. These plots show the 4 highest momentum bins together ($p_{\pi^+} \geq 0.2$ GeV); separate plots and fits for the individual momentum bins are similar.

Yields and Efficiencies

The yields and efficiencies from the fits are shown in Table 4.2.

As in $D^0 \to K^-\pi^+$, the semileptonic backgrounds turn on under the signal peak. We determine systematic uncertainties from these backgrounds in the same way – by varying the widths and positions of the two error functions in data.

Table 4.2: Pion yields and tracking efficiencies from $D^+ \to K^-\pi^+\pi^+$ in 6 bins. The systematic uncertainties in the efficiency differences come from varying the shape of the $D^+ \to K^-\pi^+ l^+\nu_l$ background in data.

	Data	Monte Carlo
$p_{\pi^+} < 0.2$ GeV		
Number found	2606 ± 51	50174 ± 224
Number not found	371 ± 20 ± 1.41	7539 ± 94
Efficiency (%)	87.54 ± 0.63 ± 0.04	86.94 ± 0.15
$\epsilon_{MC}/\epsilon_{data} - 1$	-0.69 ± 0.73 ± 0.05 % (-0.9 σ)	
$0.2 \leq p_{\pi^+} < 0.35$ GeV		
Number found	3857 ± 62	66701 ± 258
Number not found	171 ± 17 ± 1	2992 ± 85
Efficiency (%)	95.75 ± 0.41 ± 0.02	95.71 ± 0.12
$\epsilon_{MC}/\epsilon_{data} - 1$	-0.05 ± 0.44 ± 0.02 % (-0.1 σ)	
$0.35 \leq p_{\pi^+} < 0.5$ GeV		
Number found	12123 ± 110	255898 ± 506
Number not found	346 ± 26 ± 5	9042 ± 129
Efficiency (%)	97.23 ± 0.20 ± 0.04	96.59 ± 0.05
$\epsilon_{MC}/\epsilon_{data} - 1$	-0.66 ± 0.21 ± 0.04 % (-3.1 σ)	
$0.5 \leq p_{\pi^+} < 0.7$ GeV		
Number found	24325 ± 156	538011 ± 733
Number not found	687 ± 41 ± 23.09	15049 ± 185
Efficiency (%)	97.25 ± 0.16 ± 0.09	97.28 ± 0.03
$\epsilon_{MC}/\epsilon_{data} - 1$	+0.03 ± 0.17 ± 0.09 % (+0.2 σ)	
$p_{\pi^+} \geq 0.7$ GeV		
Number found	10012 ± 100	202160 ± 450
Number not found	149 ± 41 ± 4.12	4315 ± 174
Efficiency (%)	98.53 ± 0.40 ± 0.04	97.91 ± 0.08
$\epsilon_{MC}/\epsilon_{data} - 1$	-0.63 ± 0.41 ± 0.04 % (-1.5 σ)	
$\lvert\cos\theta\rvert \geq 0.9$, $p_{\pi^+} \geq 0.2$ GeV		
Number found	1324 ± 36	28709 ± 169
Number not found	3593 ± 67 ± 1	78226 ± 315
Efficiency (%)	26.93 ± 0.65 ± 0.01	26.85 ± 0.14
$\epsilon_{MC}/\epsilon_{data} - 1$	-0.30 ± 2.46 ± 0.02 % (-0.1 σ)	

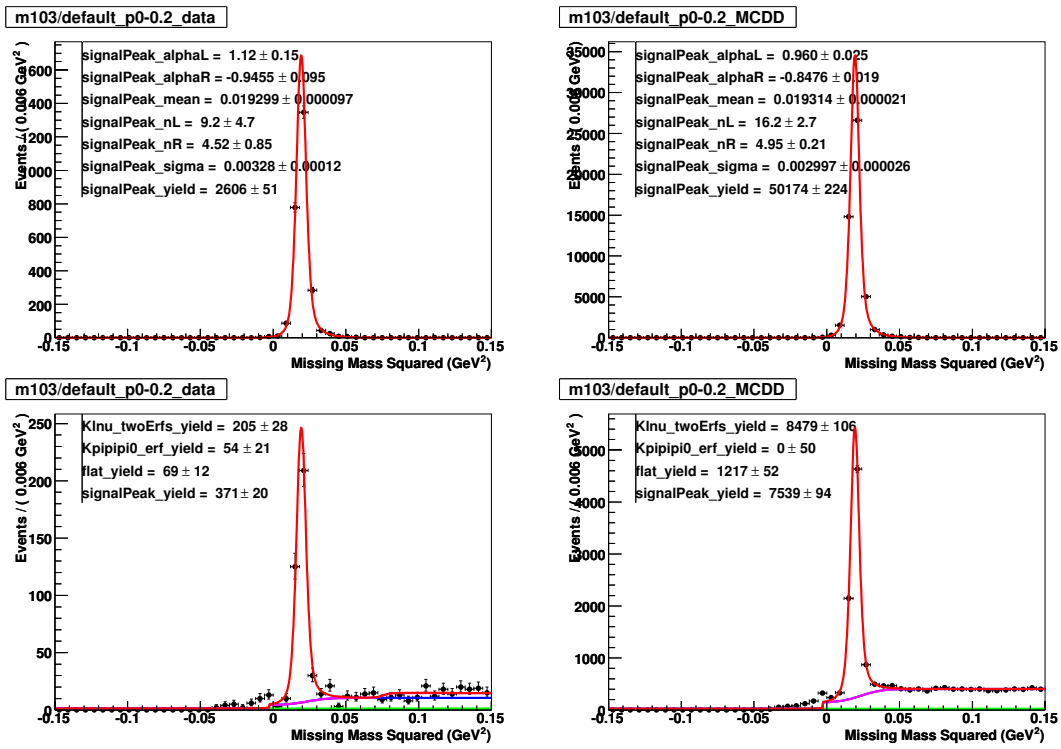

Figure 4.8: Pion efficiency from $D^+ \to K^-\pi^+\pi^+$ for $p_{\pi^+} < 0.2$ GeV. The left plots are for data and the plots to the right are for the generic Monte Carlo simulation. The top row of plots shows a fit to the missing mass squared distribution when the pion was found. The bottom row shows the distributon for the events where the pion was not found.

4.8.3 Pion Tracking Efficiency Summary

We have seven independent measurements of the difference in pion tracking efficiency between data and Monte Carlo – one from $D^0 \to K^-\pi^+$ and six from $D^+ \to K^-\pi^+\pi^+$. The seven measurements are shown in Table 4.3. All are consistent with zero discrepancy between data and Monte Carlo.

The dependence of the efficiencies and data-Monte Carlo discrepancies on pion momentum is shown in Figure 4.14. The efficiency varies across momentum bins, and this variation is modeled well in the Monte Carlo. We have added

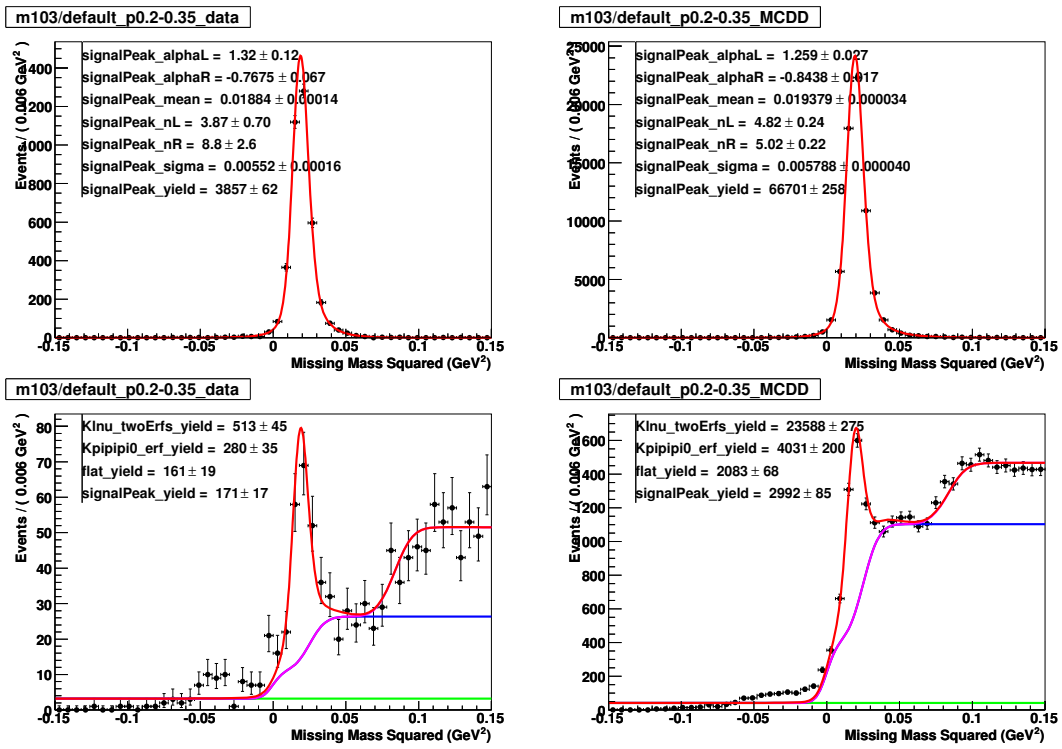

Figure 4.9: Pion efficiency from $D^+ \to K^-\pi^+\pi^+$ for $0.2 \leq p_{\pi^+} < 0.35$ GeV. The left plots are for data and the plots to the right are for the generic Monte Carlo simulation. The top row of plots shows a fit to the missing mass squared distribution when the pion was found. The bottom row shows the distributon for the events where the pion was not found.

one more data point to the discrepancy plot from a previous study of the low-momentum pions in $\psi(2S) \to J/\psi\pi^+\pi^-$ [13].

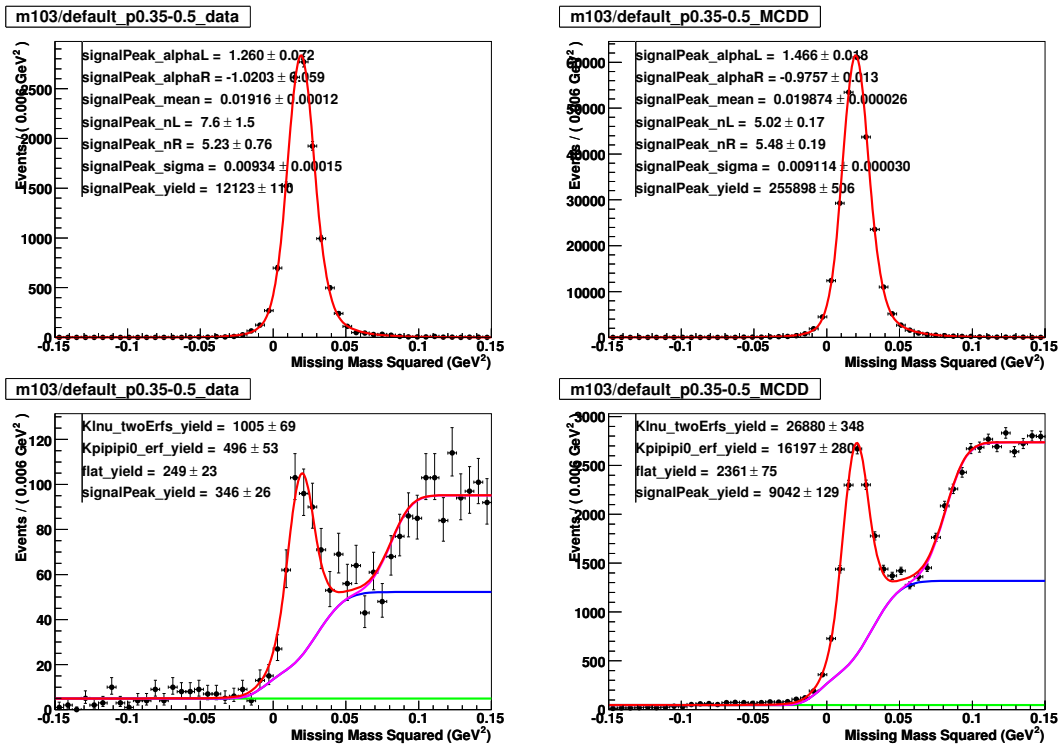

Figure 4.10: Pion efficiency from $D^+ \to K^-\pi^+\pi^+$ for $0.35 \leq p_{\pi^+} < 0.5$ GeV. The left plots are for data and the plots to the right are for the generic Monte Carlo simulation. The top row of plots shows a fit to the missing mass squared distribution when the pion was found. The bottom row shows the distributon for the events where the pion was not found.

Table 4.3: Measurements of the pion tracking efficiency difference $\epsilon_{\rm MC}/\epsilon_{\rm data} - 1$. In this table, statistical and systematic uncertainties are combined.

Mode & Bin	$\epsilon_{\rm MC}/\epsilon_{\rm data} - 1$
$K^-\pi^+\pi^+$, $\lvert\cos\theta\rvert \geq 0.9$, $p_{\pi^+} \geq 0.2$ GeV	-0.30 ± 2.46 %
$K^-\pi^+\pi^+$, $p_{\pi^+} < 0.2$ GeV	-0.69 ± 0.73 %
$K^-\pi^+\pi^+$, $0.2 \leq p_{\pi^+} < 0.35$ GeV	-0.05 ± 0.45 %
$K^-\pi^+\pi^+$, $0.35 \leq p_{\pi^+} < 0.5$ GeV	-0.66 ± 0.22 %
$K^-\pi^+\pi^+$, $0.5 \leq p_{\pi^+} < 0.7$ GeV	+0.03 ± 0.19 %
$K^-\pi^+\pi^+$, $p_{\pi^+} \geq 0.7$ GeV	-0.63 ± 0.41 %
$K^-\pi^+$ ($\sim 0.7 < p_{\pi^+} <\sim 1$ GeV)	+0.01 ± 0.36 %

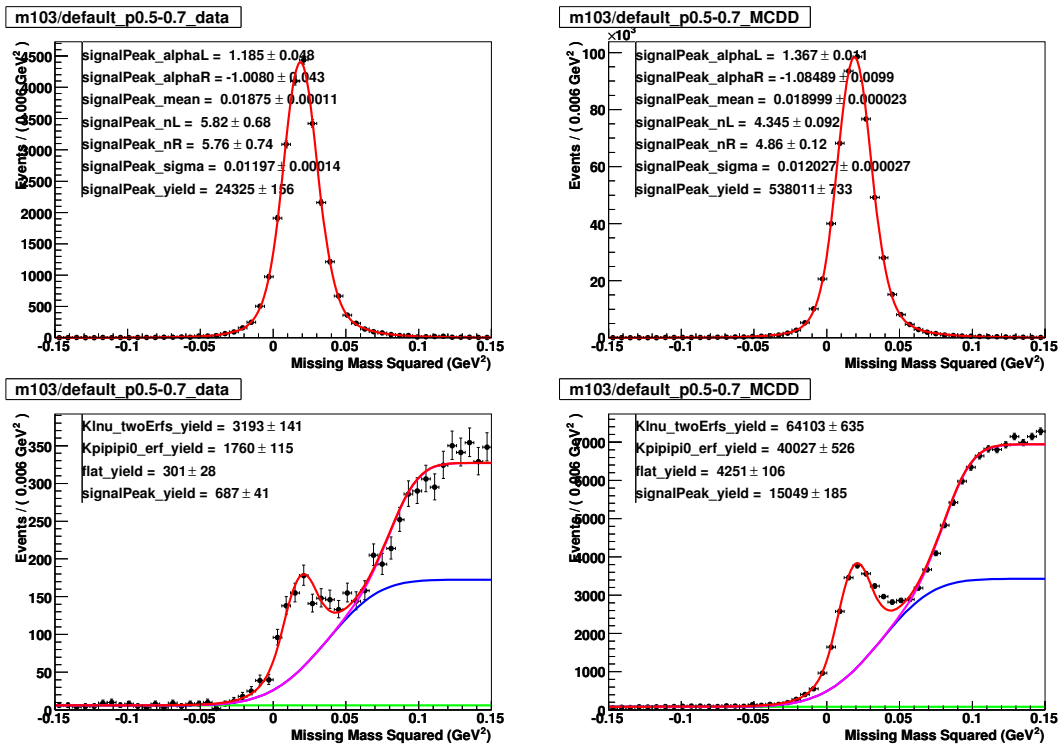

Figure 4.11: Pion efficiency from $D^+ \to K^-\pi^+\pi^+$ for $0.5 \leq p_{\pi^+} < 0.7$ GeV. The left plots are for data and the plots to the right are for the generic Monte Carlo simulation. The top row of plots shows a fit to the missing mass squared distribution when the pion was found. The bottom row shows the distributon for the events where the pion was not found.

4.9 Kaon Tracking Efficiency

4.9.1 Kaon Efficiency from $D^0 \to K^-\pi^+$

In this section, we measure the kaon tracking efficiency by looking for kaons in the decay $D^0 \to K^-\pi^+$. Events with this decay correspond to a peak in M^2_{miss} at the kaon mass squared.

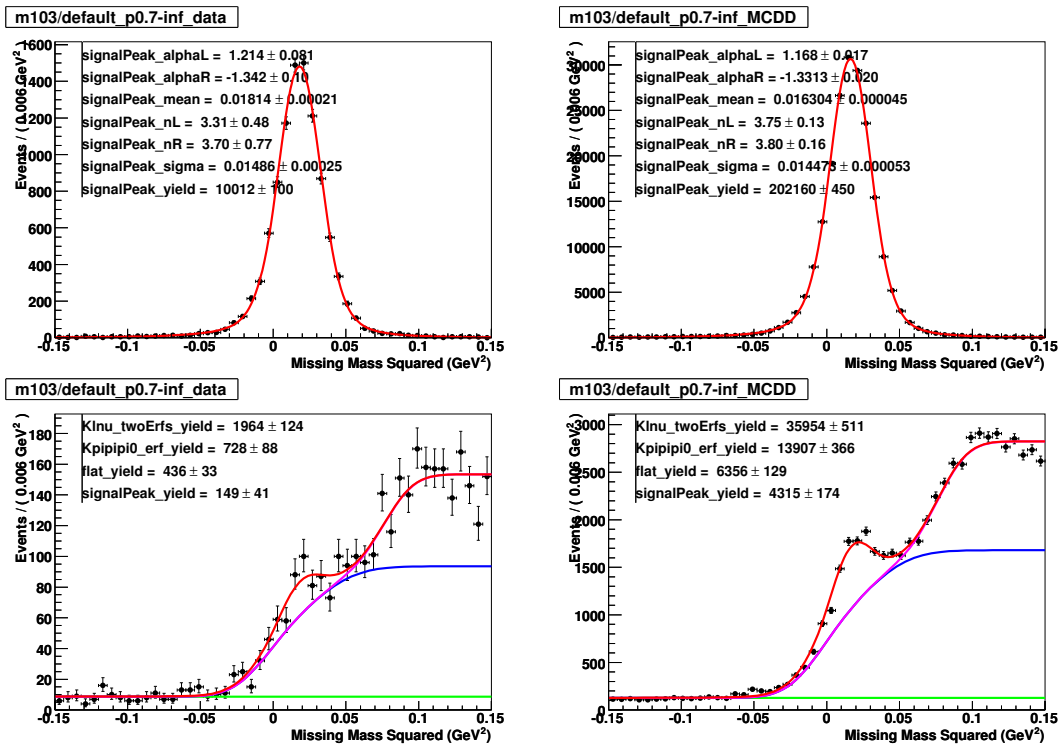

Figure 4.12: Pion efficiency from $D^+ \to K^-\pi^+\pi^+$ for $p_{\pi^+} \geq 0.7$ GeV. The left plots are for data and the plots to the right are for the generic Monte Carlo simulation. The top row of plots shows a fit to the missing mass squared distribution when the pion was found. The bottom row shows the distributon for the events where the pion was not found.

Fits

When the kaon track is not found, we observe significant background. This background arises from the decay modes $D^0 \to \pi^+\pi^-$, $D^0 \to K^-\pi^+\pi^0$, $D^0 \to \pi^-\mu^+\nu_\mu$, and $D^0 \to K^-\mu^+\nu_\mu$, with small contributions from other modes. The first background, $D^0 \to \pi^+\pi^-$, produces a peak at the pion mass squared, which is fit with a two-sided Crystal Ball peak. $D^0 \to K^-\pi^+\pi^0$ produces an error function. $D^0 \to K^-\mu^+\nu_\mu$ also produces an error function, but its yield is much smaller. The ratio of the $D^0 \to K^-\pi^+\pi^0$ and $D^0 \to K^-\mu^+\nu_\mu$ yields is fixed based on the efficien-

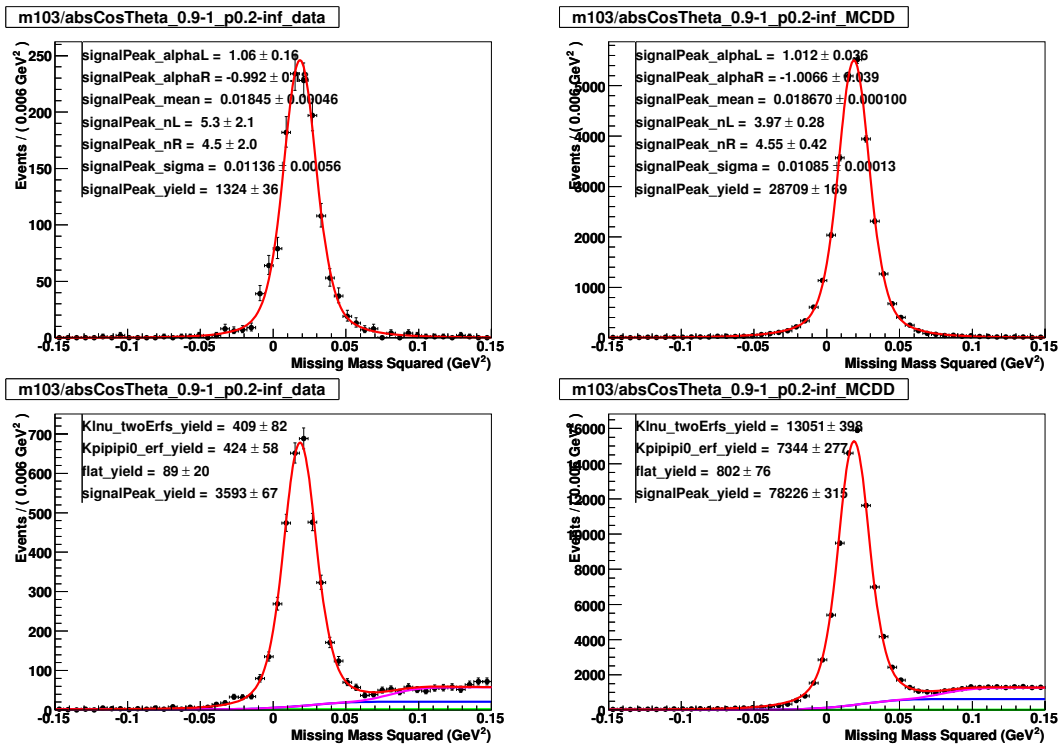

Figure 4.13: Pion efficiency from $D^+ \to K^-\pi^+\pi^+$ for 0.2 GeV $\leq p_{\pi^+}$, $|\cos\theta| \geq 0.9$. The left plots are for data and the plots to the right are for the generic Monte Carlo simulation. The top row of plots shows a fit to the missing mass squared distribution when the pion was found. The bottom row shows the distributon for the events where the pion was not found.

cies and branching fractions of these modes. The last background is a straight line rising from some cutoff in M^2_{miss}, and zero to the left of the cutoff. This shape works well empirically. The decay $D^0 \to \pi^-\mu^+\nu_\mu$ has this shape, but there are not enough events of this type to account for this entire background. Therefore this shape is also accounting for additional small backgrounds.

The parameters that determine the shapes of these backgrounds are obtained by fitting Monte Carlo simulations for these modes, as shown in Figure 4.15. For the rising straight line, we use simulated $D^0 \to \pi^-\mu^+\nu_\mu$ events to determine the

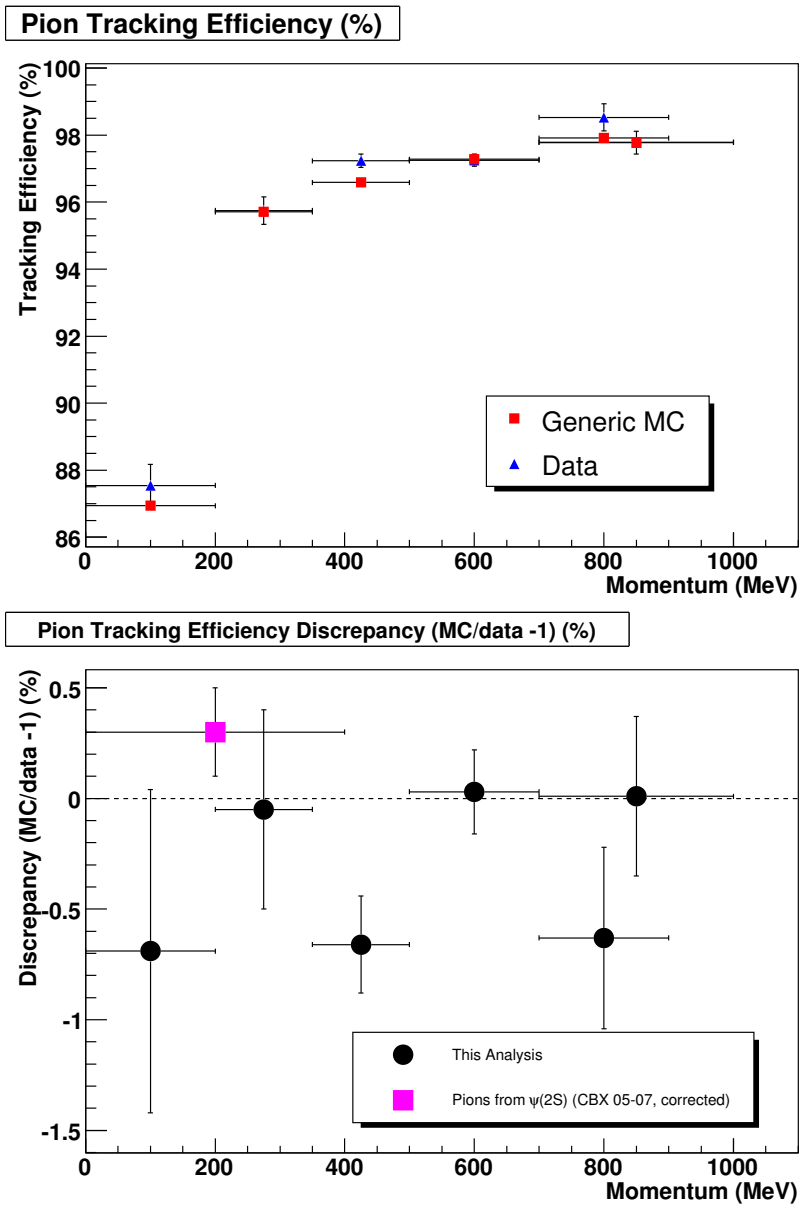

Figure 4.14: Measurements (in %) of the pion tracking efficiency (top) and the data-Monte Carlo discrepancy $\epsilon_{\mathrm{MC}}/\epsilon_{\mathrm{data}} - 1$ (bottom) in different momentum bins.

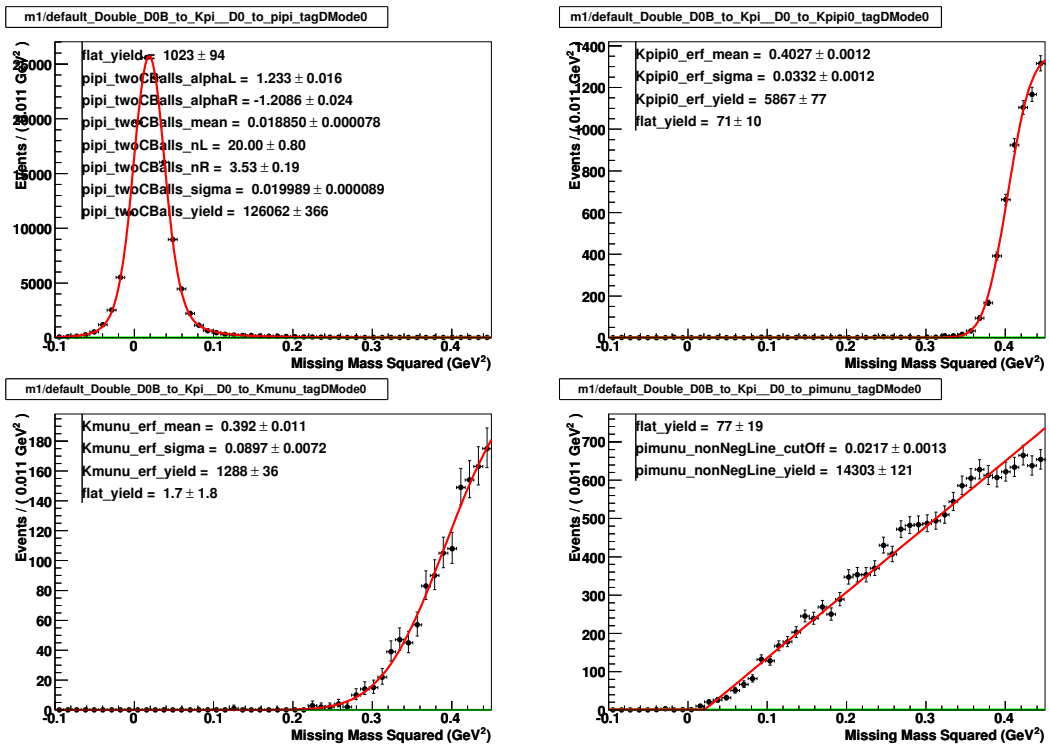

Figure 4.15: Fits to Monte Carlo simulations for the modes $D^0 \to \pi^+\pi^-$, $K^-\pi^+\pi^0$, $D^0 \to K^-\mu^+\nu_\mu$, and $D^0 \to \pi^-\mu^+\nu_\mu$, as analyzed while looking for events in which the kaon in $D^0 \to K^-\pi^+$ was not found. These shapes were used in the fits of the data and generic Monte Carlo.

cutoff. As a systematic uncertainty, we also try allowing the cutoff to float.

Fitting the generic Monte Carlo sample and the data to these backgrounds and the signal peak, we obtain the plots shown in Figure 4.16.

Yields and Efficiencies

The yields and efficiencies from the fits are shown in Table 4.4. The efficiencies in data and Monte Carlo are consistent.

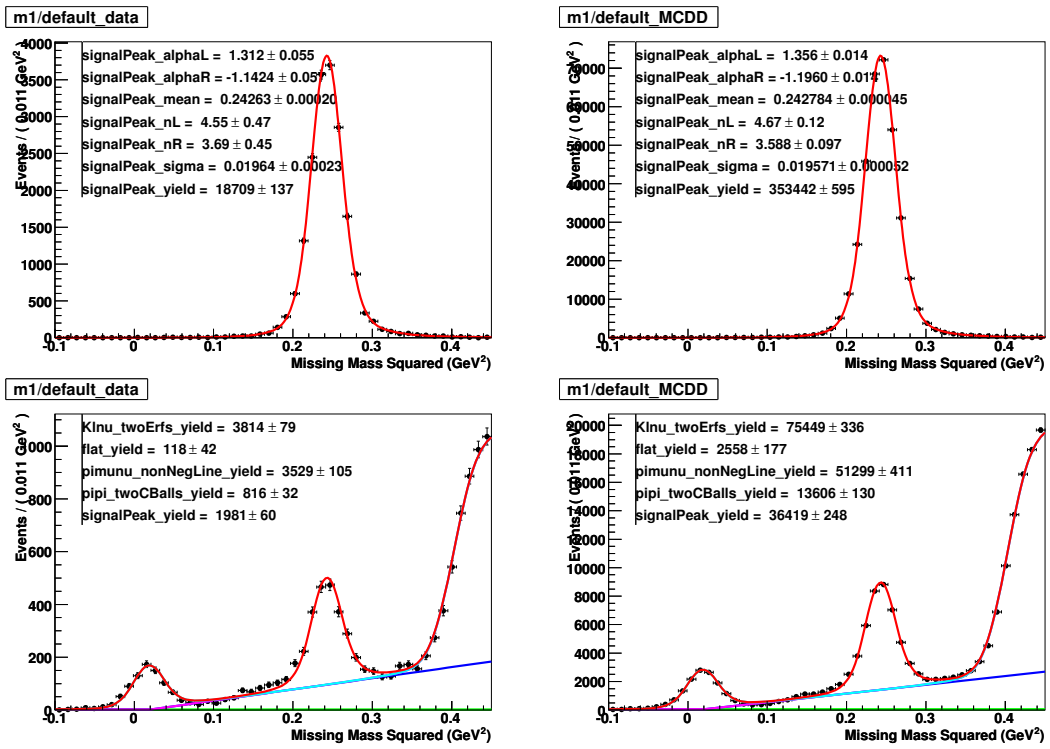

Figure 4.16: Kaon efficiency from $D^0 \to K^-\pi^+$. The left plots are for data and the plots to the right are for the generic Monte Carlo simulation. The top row of plots shows a fit to the missing mass squared distribution when the kaon was found. The bottom row of plots shows the distributon for the events where the kaon was not found.

As a systematic test, we tried allowing the cutoff of the rising linear background to float in both data and generic MC. We take the change in $\epsilon_{\text{MC}}/\epsilon_{\text{data}} - 1$ as the systematic uncertainty.

4.9.2 Kaon Efficiency from $D^0 \to K^-\pi^+\pi^0$

In this section, we measure the kaon tracking efficiency by looking for kaons in the decay $D^0 \to K^-\pi^+\pi^0$. Events with this decay correspond to a peak in M^2_{miss} at

Table 4.4: Kaon yields and tracking efficiencies from $D^0 \to K^-\pi^+$. The systematic uncertainty comes from allowing the cutoff of the rising linear background to float.

	Data	Monte Carlo
Number found	18709 ± 137	353442 ± 595
Number not found	1981 ± 60 ± 6	36419 ± 248 ± 147
Efficiency (%)	90.43 ± 0.27 ± 0.03	90.66 ± 0.06 ± 0.03
$\epsilon_{MC}/\epsilon_{data} - 1$	+0.26 ± 0.31 ± 0.01 % (+0.8 σ)	

the kaon mass squared. Since the momentum of the kaon varies, we study the efficiency in the five momentum bins. We also study a bin of small polar angle.

Fits

We do one set of fits for each momentum bin. The background underneath the signal peak for undetected kaons is fit with a linear background. The fits are shown in Figures 4.17, 4.18, 4.19, 4.20, 4.21, and 4.22.

Yields and Efficiencies

The yields and efficiencies from the fits are shown in Table 4.5. The efficiencies in Monte Carlo are consistent with the efficiencies in data.

We consider, as a systematic uncertainty, a change to the fit range. Unfortunately, we have used a small $M^2_{\rm miss}$ range because the background has other structures outside this range that are difficult to fit. As a variation, we also redo the analysis with the range tightened by 0.01 GeV^2 on each end. This alters the fitted shape of the background and hence the efficiencies. We take the change in

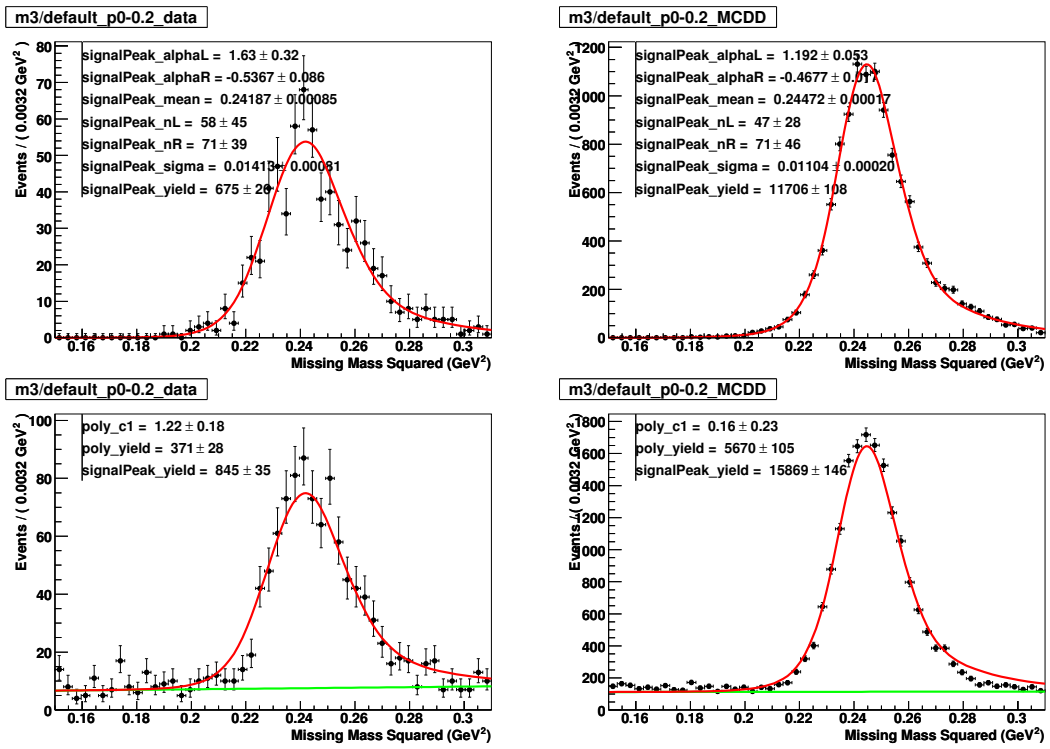

Figure 4.17: Kaon efficiency from $D^0 \to K^-\pi^+\pi^0$ for $p_{K^-} < 0.2$ GeV. The left plots are for data and the plots to the right are for the generic Monte Carlo simulation. The top row of plots shows a fit to the missing mass squared distribution when the kaon was found. The bottom row shows the distributon for the events where the kaon was not found.

$\epsilon_{\text{MC}}/\epsilon_{\text{data}} - 1$ as the systematic uncertainty.

4.9.3 Kaon Efficiency from $D^+ \to K^-\pi^+\pi^+$

In this section, we measure the kaon tracking efficiency by looking for kaons in the decay $D^+ \to K^-\pi^+\pi^+$. Events with this decay correspond to a peak in M^2_{miss} at the kaon mass squared. Since the momentum of the kaon varies, we study the efficiency in the five momentum bins. We also study a bin of small polar angle.

Table 4.5: Kaon yields and tracking efficiencies from $D^0 \to K^-\pi^+\pi^0$ in six bins. The systematics are determined by fitting over a slightly smaller $M^2_{\rm miss}$ range.

	Data	Monte Carlo
$p_{K^-} < 0.2$ GeV		
Number found	675 ± 26	11706 ± 108
Number not found	845 ± 35	15869 ± 146
Efficiency (%)	44.41 ± 1.40 ± 0.13	42.45 ± 0.32 ± 1.68
$\epsilon_{\rm MC}/\epsilon_{\rm data} - 1$	-4.41 ± 3.09 ± 3.52 % (-0.9 σ)	
$0.2 \le p_{K^-} < 0.35$ GeV		
Number found	2135 ± 46	37642 ± 194
Number not found	704 ± 42	12426 ± 163
Efficiency (%)	75.20 ± 1.18 ± 0.08	75.18 ± 0.26 ± 0.28
$\epsilon_{\rm MC}/\epsilon_{\rm data} - 1$	-0.03 ± 1.61 ± 0.48 % (-0.0 σ)	
$0.35 \le p_{K^-} < 0.5$ GeV		
Number found	2389 ± 49	32763 ± 181
Number not found	603 ± 59	7348 ± 221
Efficiency (%)	79.85 ± 1.61 ± 0.03	81.68 ± 0.46 ± 0.48
$\epsilon_{\rm MC}/\epsilon_{\rm data} - 1$	+2.30 ± 2.14 ± 0.57 % (+1.0 σ)	
$0.5 \le p_{K^-} < 0.7$ GeV		
Number found	15944 ± 126	283016 ± 532
Number not found	2042 ± 128	40387 ± 532
Efficiency (%)	88.65 ± 0.64 ± 0.02	87.51 ± 0.15 ± 0.00
$\epsilon_{\rm MC}/\epsilon_{\rm data} - 1$	-1.28 ± 0.73 ± 0.03 % (-1.8 σ)	
$p_{K^-} \ge 0.7$ GeV		
Number found	17201 ± 131	337248 ± 581
Number not found	2236 ± 157	39118 ± 620
Efficiency (%)	88.50 ± 0.72 ± 0.23	89.61 ± 0.15 ± 0.14
$\epsilon_{\rm MC}/\epsilon_{\rm data} - 1$	+1.25 ± 0.84 ± 0.43 % (+1.3 σ)	
$\lvert\cos\theta\rvert \ge 0.9$, $p_{K^-} \ge 0.2$ GeV		
Number found	691 ± 26	13444 ± 116
Number not found	2326 ± 90	40862 ± 378
Efficiency (%)	22.90 ± 0.95 ± 0.09	24.76 ± 0.24 ± 0.01
$\epsilon_{\rm MC}/\epsilon_{\rm data} - 1$	+8.09 ± 4.61 ± 0.46 % (+1.7 σ)	

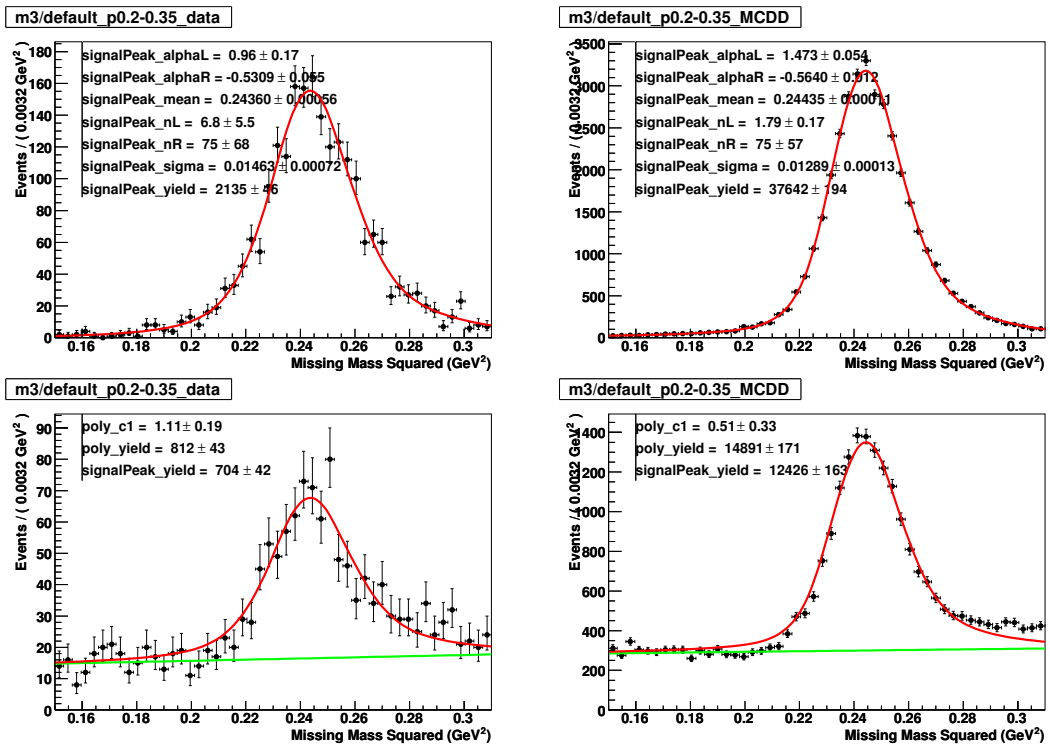

Figure 4.18: Kaon efficiency from $D^0 \to K^-\pi^+\pi^0$ for $0.2 \leq p_{K^-} < 0.35$ GeV. The left plots are for data and the plots to the right are for the generic Monte Carlo simulation. The top row of plots shows a fit to the missing mass squared distribution when the kaon was found. The bottom row shows the distributon for the events where the kaon was not found.

Fits

We do one set of fits for each momentum bin. The background underneath the signal peak for undetected kaons is fit with the sum of a flat background and an error function. The error function mean and width are fixed to be the same as the mean and width of the signal peak. The idea is to model a background turning on under the signal peak. This seems to work empirically, though we have not studied the background in detail.

The fits are shown in Figures 4.23, 4.24, 4.25, 4.26, 4.27, and 4.28.

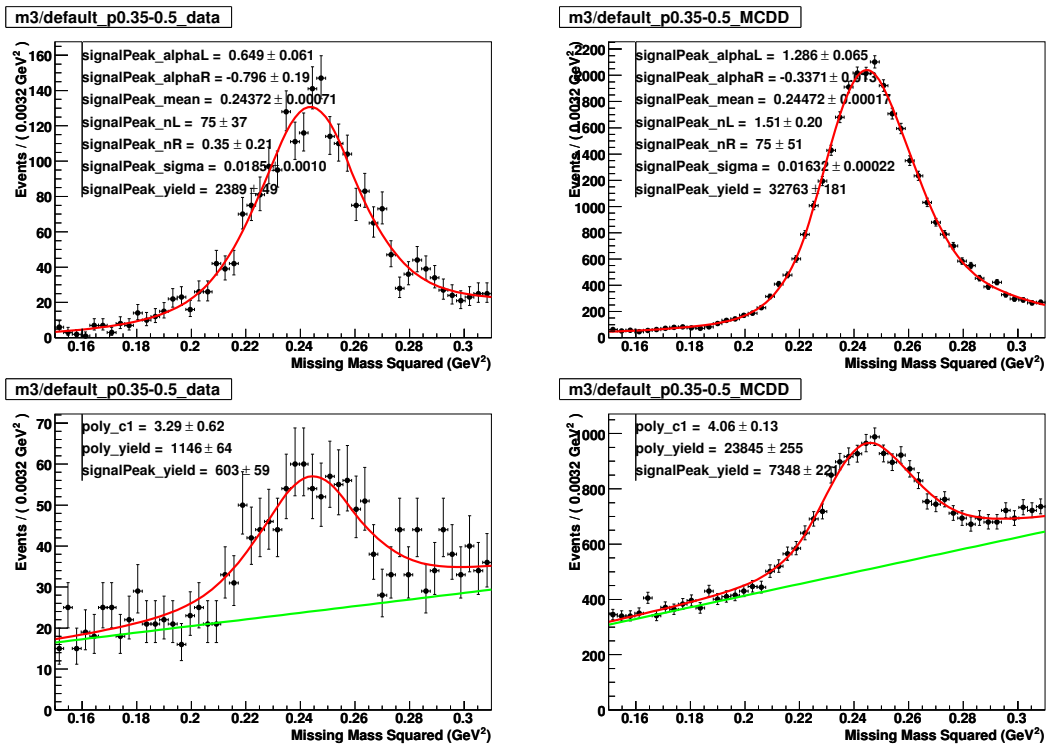

Figure 4.19: Kaon efficiency from $D^0 \to K^-\pi^+\pi^0$ for $0.35 \leq p_{K^-} < 0.5$ GeV. The left plots are for data and the plots to the right are for the generic Monte Carlo simulation. The top row of plots shows a fit to the missing mass squared distribution when the kaon was found. The bottom row shows the distributon for the events where the kaon was not found.

Yields and Efficiencies

The yields and efficiencies from the fits are shown in Table 4.6. The efficiencies in Monte Carlo are consistent with the efficiencies in data in 5 of the 6 bins. In one bin, $0.2 \leq p_{K^-} < 0.35$ GeV, they differ by 3.4 standard deviations. This bin will be significant when calculating the tracking systematic in Section 4.10 since it will be highly weighted.

Table 4.6: Kaon yields and tracking efficiencies from $D^+ \to K^-\pi^+\pi^+$ in six bins.

	Data	Monte Carlo
$p_{K^-} < 0.2$ GeV		
Number found	1095 ± 33	23817 ± 154
Number not found	1760 ± 44	37446 ± 204
Efficiency (%)	38.35 ± 0.93	38.88 ± 0.20
$\epsilon_{MC}/\epsilon_{data} - 1$	+1.36 ± 2.50 % (+0.5 σ)	
$0.2 \leq p_{K^-} < 0.35$ GeV		
Number found	4776 ± 69	98468 ± 314
Number not found	1457 ± 44	33530 ± 205
Efficiency (%)	76.62 ± 0.60	74.60 ± 0.13
$\epsilon_{MC}/\epsilon_{data} - 1$	-2.64 ± 0.78 % (-3.4 σ)	
$0.35 \leq p_{K^-} < 0.5$ GeV		
Number found	5721 ± 76	127050 ± 356
Number not found	1199 ± 45	26141 ± 195
Efficiency (%)	82.67 ± 0.57	82.94 ± 0.11
$\epsilon_{MC}/\epsilon_{data} - 1$	+0.32 ± 0.71 % (+0.5 σ)	
$0.5 \leq p_{K^-} < 0.7$ GeV		
Number found	8477 ± 92	182290 ± 427
Number not found	1157 ± 54	26213 ± 225
Efficiency (%)	87.99 ± 0.51	87.43 ± 0.10
$\epsilon_{MC}/\epsilon_{data} - 1$	-0.64 ± 0.58 % (-1.1 σ)	
$p_{K^-} \geq 0.7$ GeV		
Number found	8054 ± 90	149665 ± 387
Number not found	980 ± 53	17081 ± 205
Efficiency (%)	89.15 ± 0.53	89.76 ± 0.11
$\epsilon_{MC}/\epsilon_{data} - 1$	+0.68 ± 0.62 % (+1.1 σ)	
$\lvert\cos\theta\rvert \geq 0.9$, $p_{K^-} \geq 0.2$ GeV		
Number found	690 ± 26	14131 ± 119
Number not found	2574 ± 60	55345 ± 268
Efficiency (%)	21.14 ± 0.74	20.34 ± 0.16
$\epsilon_{MC}/\epsilon_{data} - 1$	-3.79 ± 3.44 % (-1.1 σ)	

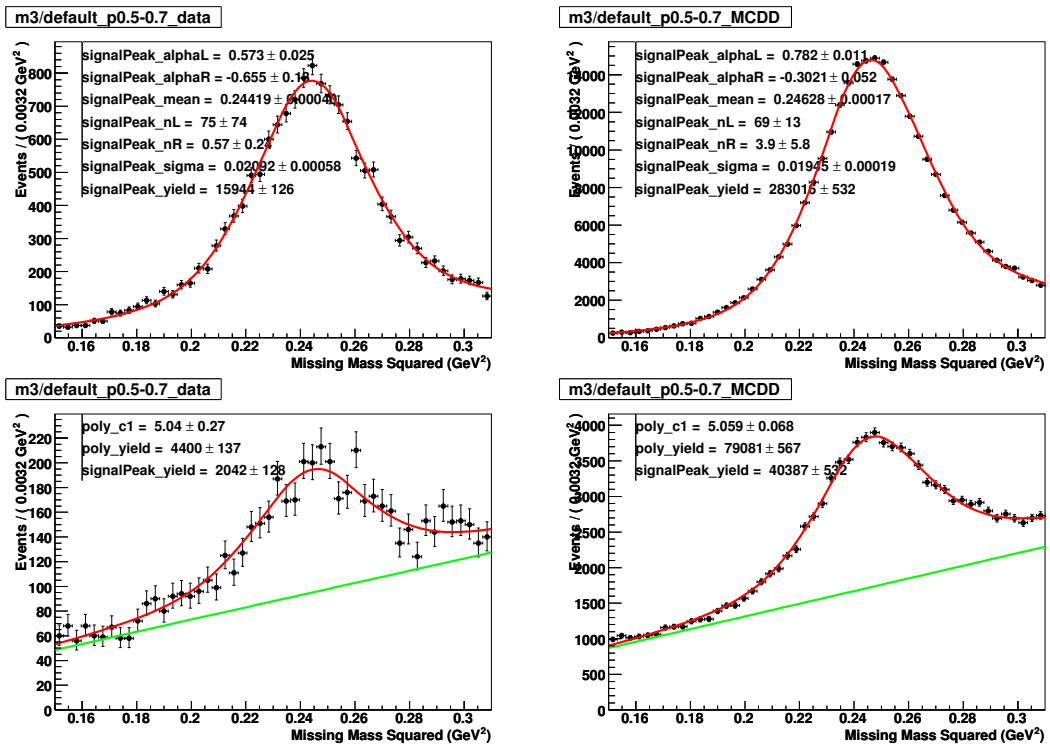

Figure 4.20: Kaon efficiency from $D^0 \to K^-\pi^+\pi^0$ for $0.5 \leq p_{K^-} < 0.7$ GeV. The left plots are for data and the plots to the right are for the generic Monte Carlo simulation. The top row of plots shows a fit to the missing mass squared distribution when the kaon was found. The bottom row shows the distributon for the events where the kaon was not found.

4.9.4 Kaon Tracking Efficiency Summary

We have 13 independent measurements of the difference in kaon tracking efficiency between data and Monte Carlo – one from $D^0 \to K^-\pi^+$ and six each from $D^0 \to K^-\pi^+\pi^0$ and $D^+ \to K^-\pi^+\pi^+$. These include two measurements in each of the momentum and angular bins. We average the $D^0 \to K^-\pi^+\pi^0$ and $D^+ \to K^-\pi^+\pi^+$ results within each bin. The measurements and averages are shown in Table 4.7. One bin, $0.2 \leq p_{K^-} < 0.35$ GeV, shows a discrepancy at a significance of 3 standard deviations; the other bins are consistent with zero discrepancy between

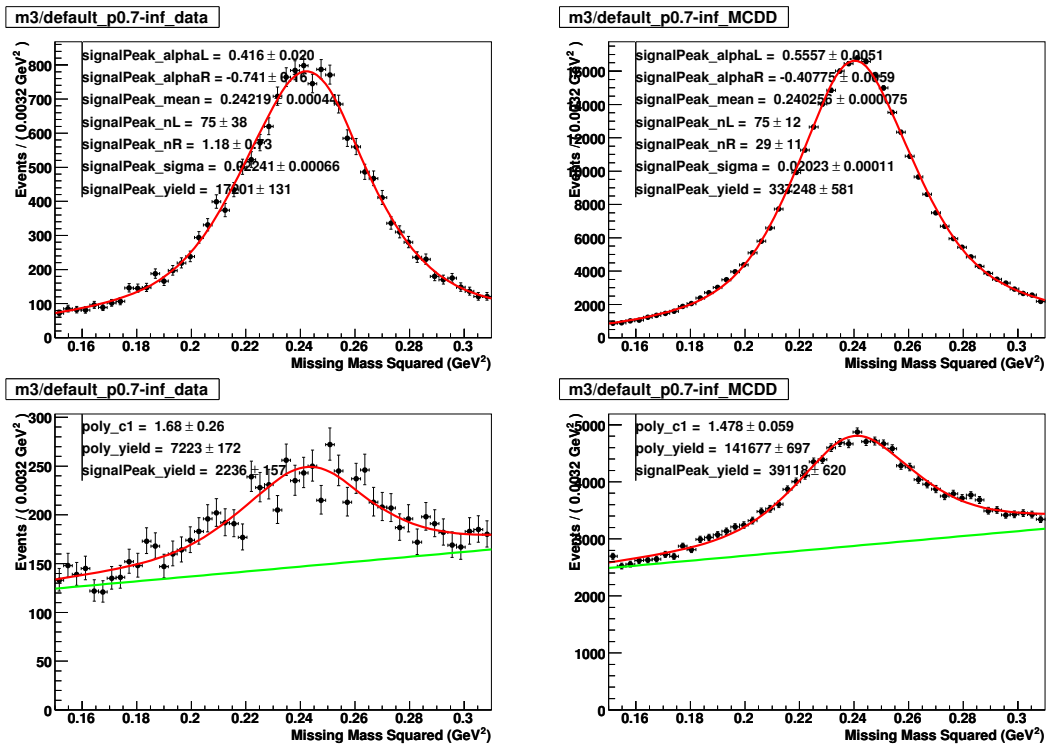

Figure 4.21: Kaon efficiency from $D^0 \to K^-\pi^+\pi^0$ for $p_{K^-} \geq 0.7$ GeV. The left plots are for data and the plots to the right are for the generic Monte Carlo simulation. The top row of plots shows a fit to the missing mass squared distribution when the kaon was found. The bottom row shows the distributon for the events where the kaon was not found.

data and Monte Carlo.

The dependence of the efficiencies and data-Monte Carlo discrepancies on kaon momentum is shown in Figure 4.29. The efficiency varies substantially across momentum bins, but the variation is modeled well in the Monte Carlo.

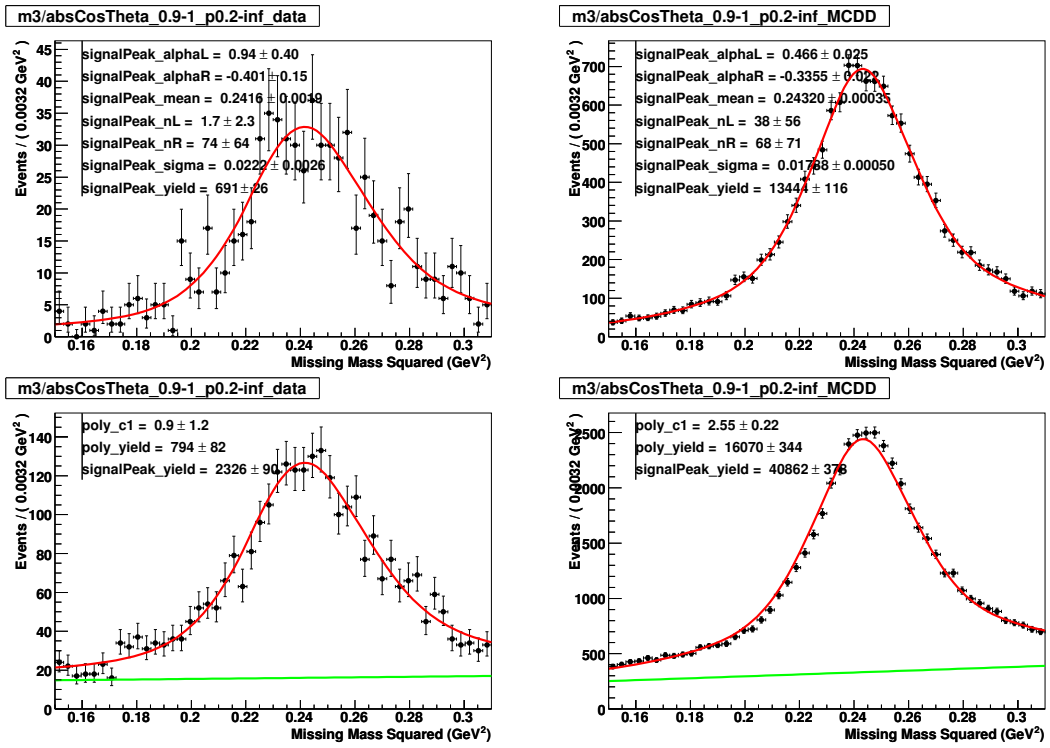

Figure 4.22: Kaon efficiency from $D^0 \to K^-\pi^+\pi^0$ for 0.2 GeV $\leq p_{K^-}$, $|\cos\theta| \geq 0.9$. The left plots are for data and the plots to the right are for the generic Monte Carlo simulation. The top row of plots shows a fit to the missing mass squared distribution when the kaon was found. The bottom row shows the distributon for the events where the kaon was not found.

Table 4.7: Measurements of the kaon tracking efficiency difference $\epsilon_{MC}/\epsilon_{data} - 1$ and averages within bins. In this table, statistical and systematic uncertainties are combined.

	$D^0 \to K^-\pi^+\pi^0$	$D^+ \to K^-\pi^+\pi^+$	Average
$\|\cos\theta\| \geq 0.9$, $p_{K^-} \geq 0.2$ GeV	+8.09 ± 4.64 %	-3.79 ± 3.44 %	+0.43 ± 2.76 %
$p_{K^-} < 0.2$ GeV	-4.41 ± 4.68 %	+1.36 ± 2.50 %	+0.08 ± 2.21 %
$0.2 \leq p_{K^-} < 0.35$ GeV	-0.03 ± 1.68 %	-2.64 ± 0.78 %	-2.18 ± 0.71 %
$0.35 \leq p_{K^-} < 0.5$ GeV	+2.30 ± 2.21 %	+0.32 ± 0.71 %	+0.50 ± 0.67 %
$0.5 \leq p_{K^-} < 0.7$ GeV	-1.28 ± 0.73 %	-0.64 ± 0.58 %	-0.89 ± 0.45 %
$p_{K^-} \geq 0.7$ GeV	+1.25 ± 0.94 %	+0.68 ± 0.62 %	+0.85 ± 0.52 %
		$K^-\pi^+$ ($\sim 0.7 \leq p_{K^-} \leq \sim 1$ GeV)	+0.26 ± 0.31 %

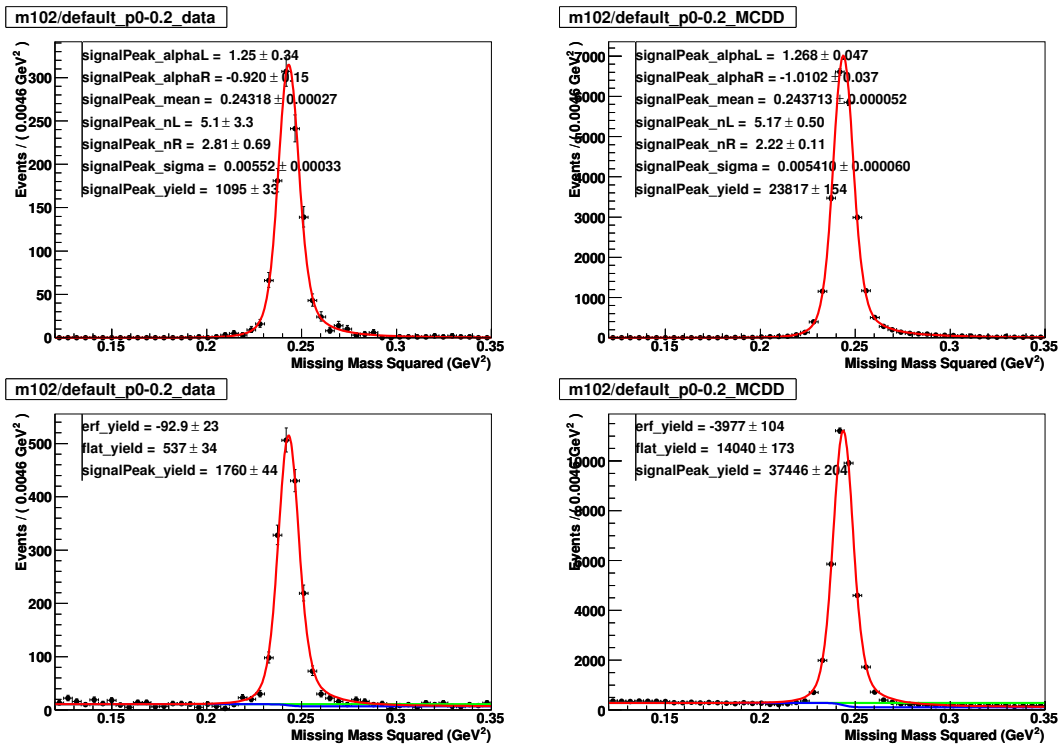

Figure 4.23: Kaon efficiency from $D^+ \to K^-\pi^+\pi^+$ for $p_{K^-} < 0.2$ GeV. The left plots are for data and the plots to the right are for the generic Monte Carlo simulation. The top row of plots shows a fit to the missing mass squared distribution when the kaon was found. The bottom row shows the distributon for the events where the kaon was not found.

4.10 Calculation of Tracking Systematic Uncertainty

The procedure for calculating the tracking efficiency systematic is based on the observation in Section 4.2.1 that tracks which pass through the entire drift chamber[2] before decaying[3] are almost always found. This leads to a systematic that varies depending on momentum and particle type.

[2] A particle has passed through the entire drift chamber if it either hits the outer radius of the drift chamber or if it hits one of the endplates. Both the outer radius and the endplates are considered in the implementation.

[3] In this section, we use "decay" as shorthand for "decay or interact" or "die."

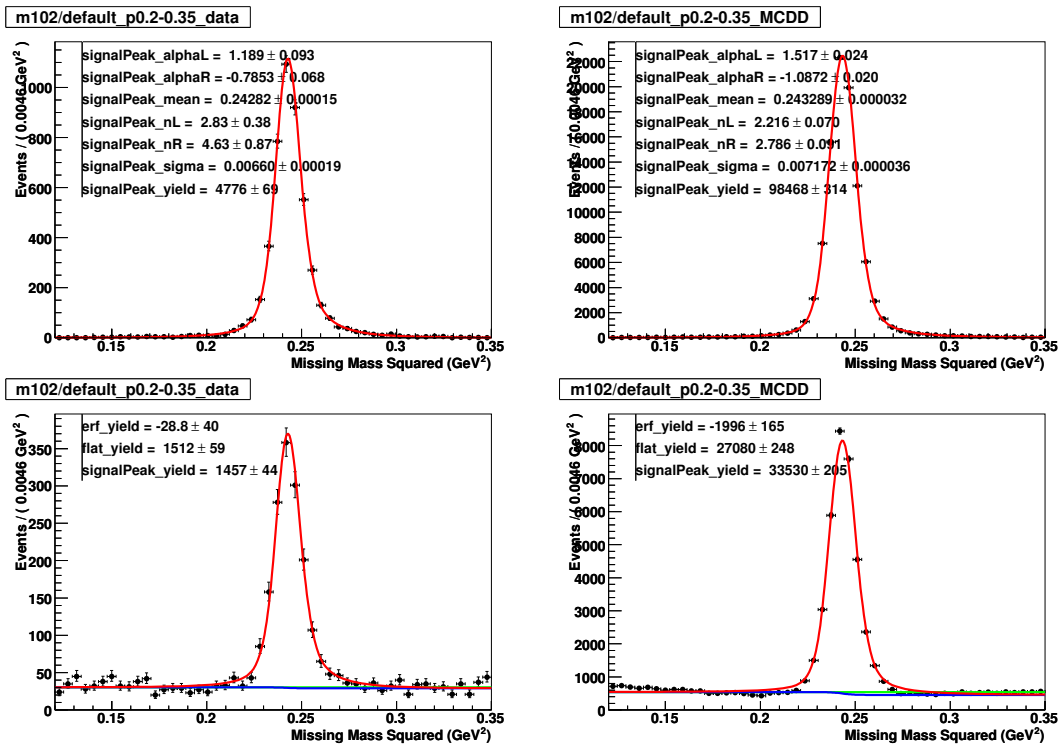

Figure 4.24: Kaon efficiency from $D^+ \to K^-\pi^+\pi^+$ for $0.2 \leq p_{K^-} < 0.35$ GeV. The left plots are for data and the plots to the right are for the generic Monte Carlo simulation. The top row of plots shows a fit to the missing mass squared distribution when the kaon was found. The bottom row shows the distributon for the events where the kaon was not found.

Tracks are divided into two classes – those that decay inside the drift chamber and those that do not. Tracks not decaying in the drift chamber have an efficiency of nearly 100%, regardless of particle type or momentum. Tracks that do decay have a lower efficiency. In the model we use to develop the tracking systematic, this efficiency is the same, regardless of particle type or momentum. Then the variation in tracking efficiency between different particle types and momentum ranges is simply a function of how often particles of that type and momentum decay within the drift chamber. The efficiency for a decaying

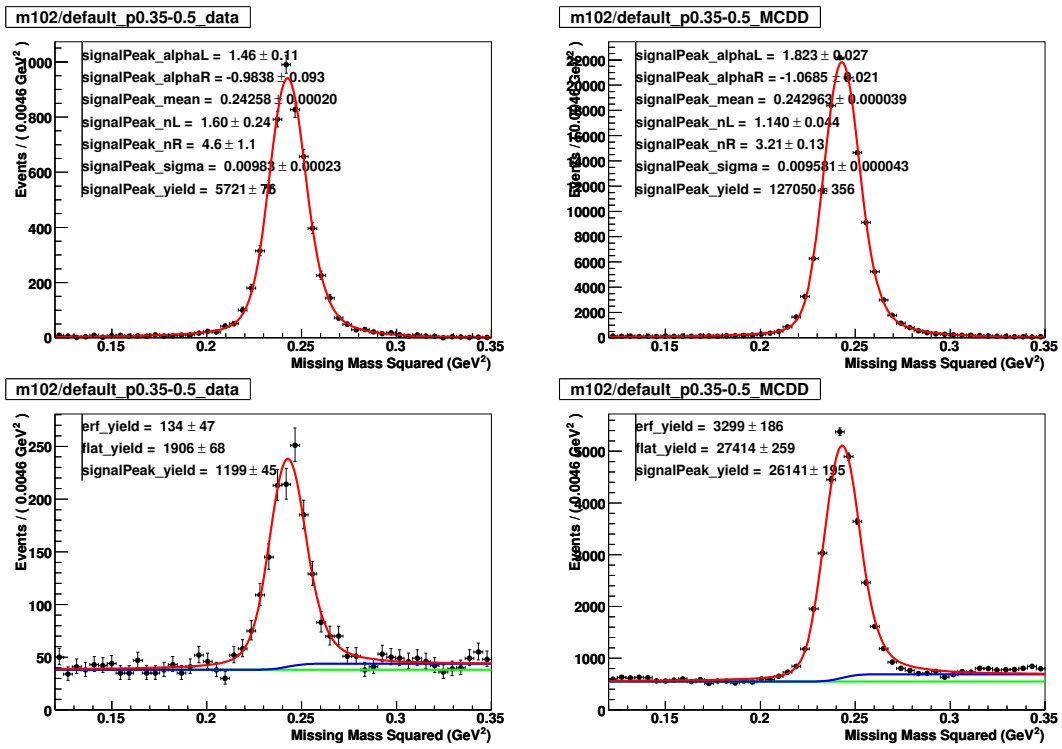

Figure 4.25: Kaon efficiency from $D^+ \to K^-\pi^+\pi^+$ for $0.35 \leq p_{K^-} < 0.5$ GeV. The left plots are for data and the plots to the right are for the generic Monte Carlo simulation. The top row of plots shows a fit to the missing mass squared distribution when the kaon was found. The bottom row shows the distributon for the events where the kaon was not found.

particle is related to the total efficiency for a given mode by

$$\epsilon_{\text{tot}} = (1 - f)(100\%) + f\epsilon_{\text{dec}} \tag{4.8}$$

where f is the fraction of particles decaying inside the drift chamber, ϵ_{dec} is the tracking efficiency for a particle decaying inside, and ϵ_{tot} is the total efficiency for a mode in which a fraction f of the particles decay inside. In this model, ϵ_{dec} is the same for all particles and momentum ranges, and tracking efficiency for a given particle and momentum is a function of f.

Tracking efficiencies in different bins sample the two classes of tracks differ-

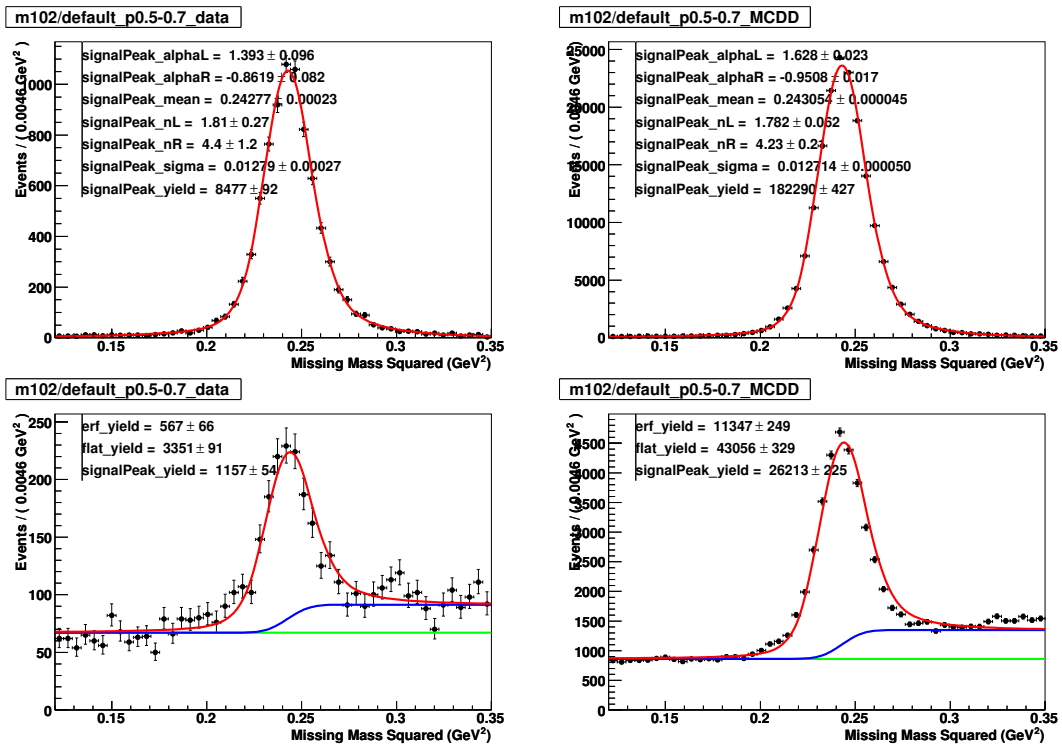

Figure 4.26: Kaon efficiency from $D^+ \to K^-\pi^+\pi^+$ for $0.5 \leq p_{K^-} < 0.7$ GeV. The left plots are for data and the plots to the right are for the generic Monte Carlo simulation. The top row of plots shows a fit to the missing mass squared distribution when the kaon was found. The bottom row shows the distributon for the events where the kaon was not found.

ently. Therefore measurements in different bins and different particle types are not directly comparable. For example, if decaying tracks were modeled poorly but tracks not decaying were modeled well, then pions (which seldom decay inside) would show little discrepancy between data and Monte Carlo, but kaons (which more often decay inside) would show a higher discrepancy. This affects both the averaging of effiency measurements between momentum bins and the calculation of the tracking systematics. Measurements in bins where f is large carry much more information about ϵ_{dec} than bins with small f; therefore low-momentum kaons are the most valuable measurement. At the end, the

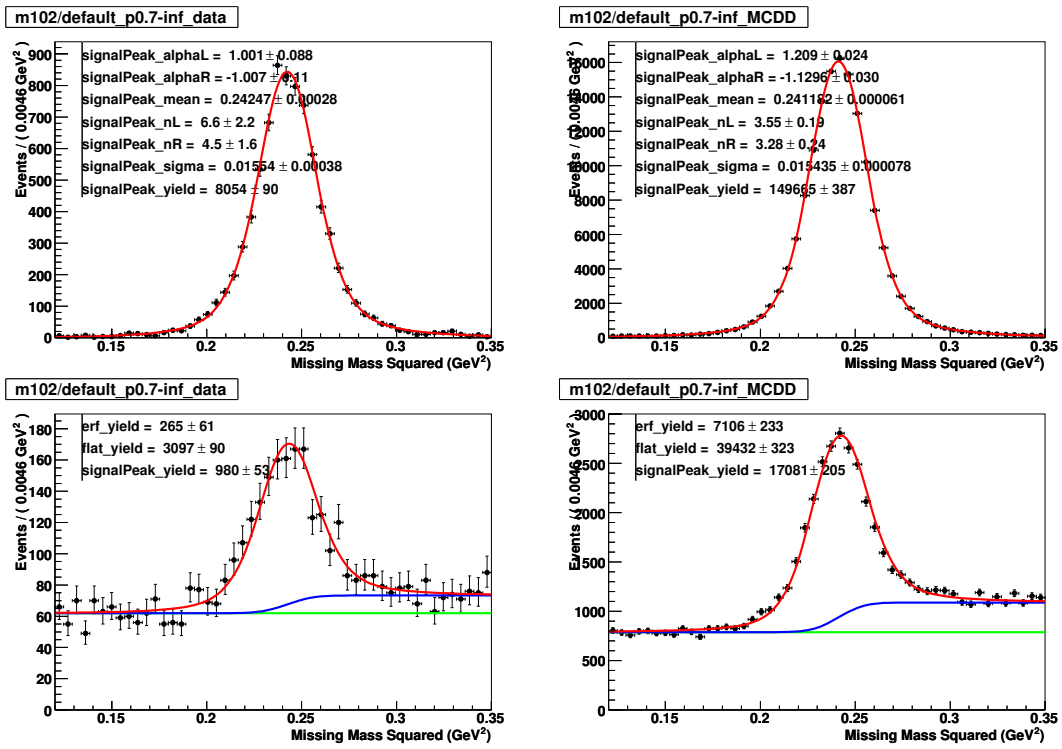

Figure 4.27: Kaon efficiency from $D^+ \to K^-\pi^+\pi^+$ for $p_{K^-} \geq 0.7$ GeV. The left plots are for data and the plots to the right are for the generic Monte Carlo simulation. The top row of plots shows a fit to the missing mass squared distribution when the kaon was found. The bottom row shows the distributon for the events where the kaon was not found.

final tracking systematic is different for different particle types and momentum ranges, according to how often those tracks decay inside the drift chamber.

The procedure for calculating the tracking systematic is as follows:

- For each decay mode, particle type, and momentum bin, determine the value of f for that particle from Monte Carlo simulation.
- Using Eq. 4.8, convert each measured value of ϵ_{tot} – the overall tracking efficiencies measured in Sections 4.8 and 4.9 – to a value of ϵ_{dec}. The uncertainty on ϵ_{dec} is inversely proportional to f; therefore low-momentum

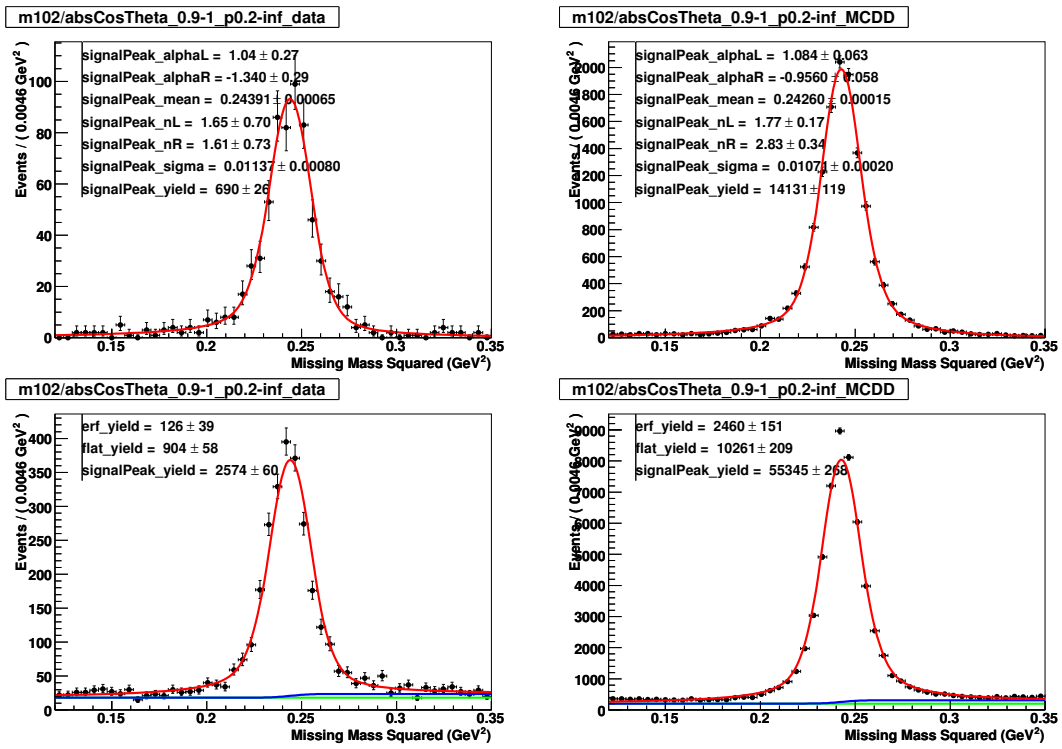

Figure 4.28: Kaon efficiency from $D^+ \to K^-\pi^+\pi^+$ for 0.2 GeV $\leq p_{K^-}$, $|\cos\theta| \geq 0.9$. The left plots are for data and the plots to the right are for the generic Monte Carlo simulation. The top row of plots shows a fit to the missing mass squared distribution when the kaon was found. The bottom row shows the distributon for the events where the kaon was not found.

kaons produce the smallest uncertainties. Calculate the data-Monte Carlo discrepancy $\epsilon_{\text{dec,MC}}/\epsilon_{\text{dec,data}} - 1$ in each bin.

- The values of $\epsilon_{\text{dec,MC}}/\epsilon_{\text{dec,data}} - 1$ calculated in each bin are measurements of the same quantity, the discrepancy in the efficiency for finding tracks that decay inside the drift chamber. Average these values across bins, weighted according to uncertainty, to determine a single value for the discrepancy. Because these uncertainties are lower for higher f, this gives greater significance to modes with high f. In particular, the average is dominated by measurements of low-momentum kaons.

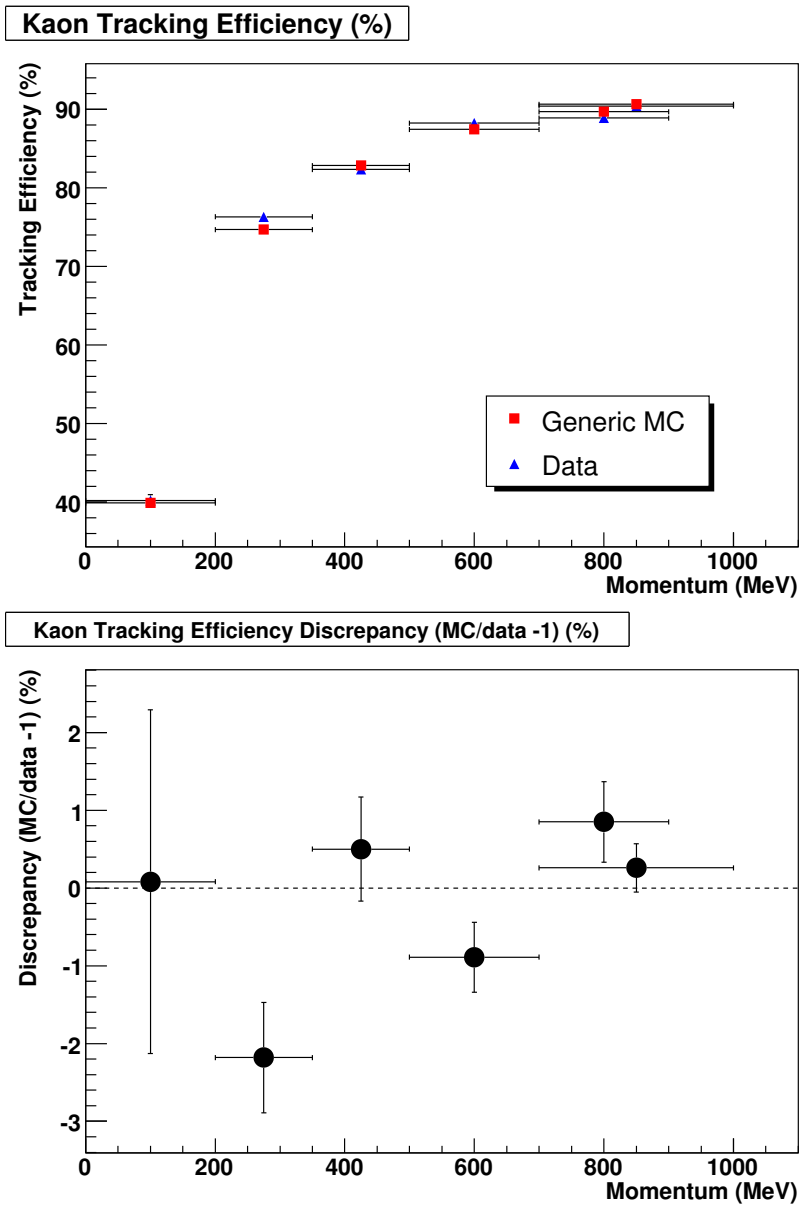

Figure 4.29: Measurements (in %) of the kaon tracking efficiency (top) and the data-Monte Carlo discrepancy $\epsilon_{\mathrm{MC}}/\epsilon_{\mathrm{data}} - 1$ (bottom) in different momentum bins.

- Calculate the discrepancy in the overall tracking efficiency using the following equation, which is derived from Eq. 4.8:

$$\epsilon_{\text{tot,MC}}/\epsilon_{\text{tot,data}} - 1 = \frac{\epsilon_{\text{dec,MC}}/\epsilon_{\text{dec,data}} - 1}{1 + \frac{1-f}{f}\frac{1}{\epsilon_{\text{dec,data}}}} \tag{4.9}$$

  This equation depends on f, which is in turn a function of momentum and particle type. Using values of f determined from Monte Carlo simulation, determine the discrepancy in overall tracking efficiency, $\epsilon_{\text{tot,MC}}/\epsilon_{\text{tot,data}} - 1$, as a function of momentum and particle type. In fact, the discrepancy and its uncertainty are roughly proportional to f. Thus, the discrepancy for a given particle is small for high-momentum pions and large for low-momentum kaons.

- Take the uncertainty and central value of the discrepancy in quadrature to determine the tracking efficiency systematic. Also add in quadrature systematic uncertainties for tracks that do not decay in the drift chamber and for tracks at small polar angles.

- To obtain a tracking systematic for a given particle, take an average of this momentum-dependent systematic, weighted by the particle's momentum spectrum.

This procedure uses an approximate model, and it should be understood not as a precise exercise, but rather a way to get a physically well-motivated and momentum-dependent systematic uncertainty.

Very low-momentum tracks will have a small radius of curvature that does not allow them to reach the outer wall of the drift chamber; instead their helical path may have several loops inside the detector. These tracks, called curlers, are a special case, and they are not included in this model. A curler at an angle close

to perpendicular with the beamline will necessarily decay inside the drift chamber, but as long as it completes its first half-loop it is likely to be reconstructed. A higher-momentum track that decays in the drift chamber may fail the requirement that at least half the detector layers along its helix contain hits, and may therefore be lost. But a curler that completes a half-loop will not fail this requirement even though it decayed inside. The procedure described above will be applied only to the momentum bins above 0.2 GeV. The lowest-momentum tracks will be treated separately.

4.10.1 Estimates of f

To estimate f, we measure it using Monte Carlo truth as a function of momentum for kaons and pions with $|\cos\theta| < 0.9$. This is plotted in Figure 4.30.

We will use these plots to estimate f for the various tracking efficiency measurments and later to determine a systematic as a function of momentum.

4.10.2 Calculations of ϵ_{dec}

Table 4.8 shows the values of ϵ_{tot}, estimates of f, and calculated values of ϵ_{dec} for each kaon tracking efficiency measurement. Given the crudity of the estimates of f, the values of ϵ_{dec} agree reasonably well between modes. When we average the data-Monte Carlo discrepancies for ϵ_{dec}, we find -5.99±2.18%. The average is dominated by the low-momentum kaons in $D^+ \to K^-\pi^+\pi^+$. Unfortunately, the significant discrepancy in the bin $0.2 \leq p_K < 0.35$ GeV is heavily weighted, and so the discrepancy in ϵ_{dec} is also significant.

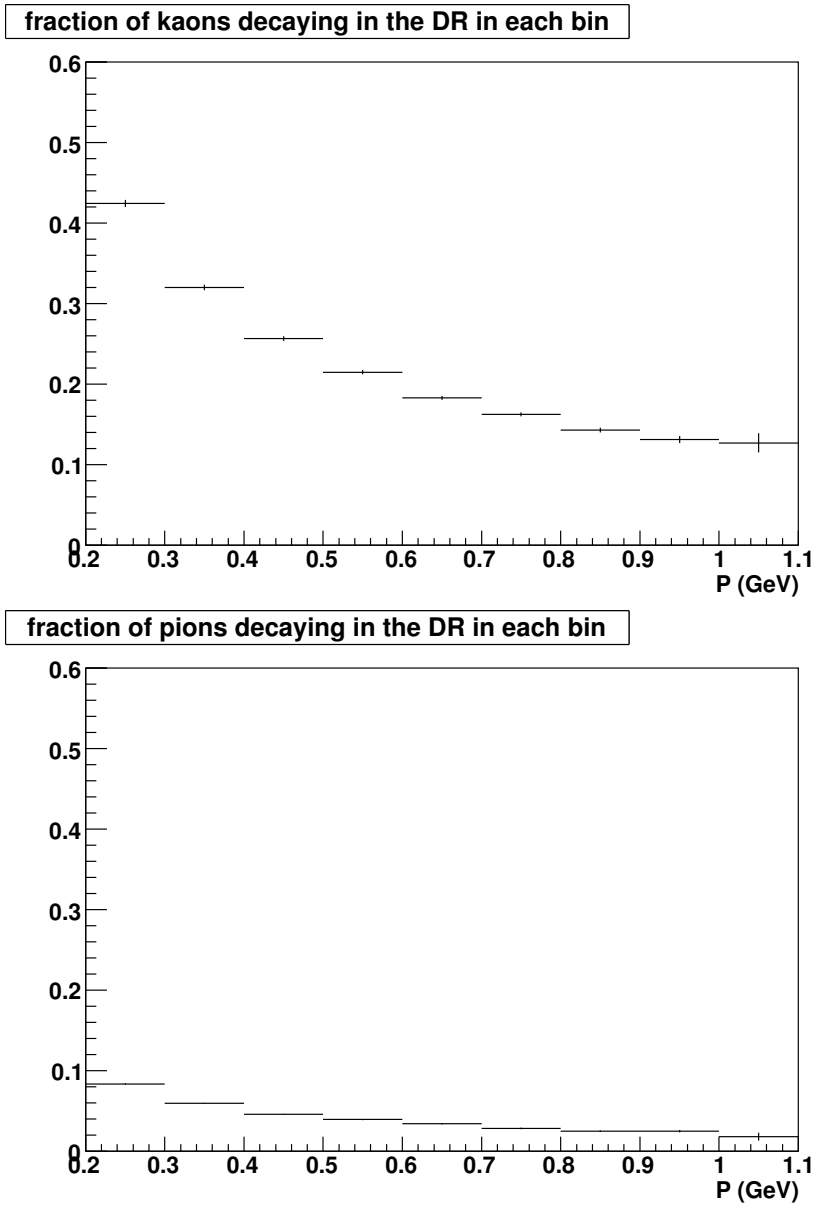

Figure 4.30: Fraction of kaons (top) and pions (bottom) decaying inside the drift chamber as a function of kaon momentum, for $|\cos\theta| < 0.9$. The numerical values in these plots are listed in Table 4.9. (The vertical scales are not percent; the top of the vertical axis is 0.6 = 60%.)

Table 4.8: Values (in %) of ϵ_{tot}, estimates of f, and calculated values of ϵ_{dec} for each kaon tracking efficiency measurement. In this table, statistical and systematic uncertainties are combined.

Mode	$\epsilon_{\text{tot,data}}$ $\epsilon_{\text{tot,MC}}$ $\epsilon_{\text{tot,MC}}/\epsilon_{\text{tot,data}} - 1$	f	$\epsilon_{\text{dec,data}}$ $\epsilon_{\text{dec,MC}}$ $\epsilon_{\text{dec,MC}}/\epsilon_{\text{dec,data}} - 1$
K in $K\pi$ ($p_K \sim 0.8$ GeV)	90.43±0.27 90.66±0.07 0.26±0.31	14%	31.61±1.94 33.27±0.49 5.27± 6.63
K in $K\pi\pi^0$ $0.2 \leq p_K < 0.35$ GeV	75.20±1.19 75.18±0.38 -0.03±1.66	39%	36.42±3.04 36.36±0.98 -0.15± 8.76
K in $K\pi\pi^0$ $0.35 \leq p_K < 0.5$ GeV	79.85±1.61 81.68±0.66 2.30±2.22	28%	28.02±7.75 35.57±2.37 23.38±26.68
K in $K\pi\pi^0$ $0.5 \leq p_K < 0.7$ GeV	88.65±0.64 87.51±0.15 -1.28±0.73	20%	43.23±3.18 37.56±0.73 -13.12± 6.61
K in $K\pi\pi^0$ $0.7 \leq p_K$	88.50±0.76 89.61±0.20 1.25±0.89	15%	23.31±5.04 30.71±1.36 31.76±29.07
K in $K\pi\pi$ $0.2 \leq p_K < 0.35$ GeV	76.62±0.60 74.60±0.13 -2.64±0.78	39%	40.06±1.54 34.87±0.34 -12.97± 3.44
K in $K\pi\pi$ $0.35 \leq p_K < 0.5$ GeV	82.67±0.57 82.94±0.11 0.32±0.71	28%	38.12±2.04 39.06±0.40 2.46± 5.58
K in $K\pi\pi$ $0.5 \leq p_K < 0.7$ GeV	87.99±0.51 87.43±0.10 -0.64±0.58	20%	39.95±2.53 37.14±0.49 -7.04± 6.02
K in $K\pi\pi$ $0.7 \leq p_K$	89.15±0.53 89.76±0.11 0.68±0.62	15%	27.68±3.56 31.71±0.75 14.55±14.98
Average	 -0.06±0.21		36.72±0.83 35.82±0.19 -5.99± 2.18

Pion efficiency measurements would provide very little additional information. Uncertainties in ϵ_{dec} are higher since f is much smaller ($\sim$ 5%) for pions. Therefore, we have not included pion measurements in the table or the average.

4.10.3 Calculation of Momentum-Dependent Efficiency Systematic

Having determined an average for $\epsilon_{\mathrm{dec,MC}}/\epsilon_{\mathrm{dec,data}} - 1$, we calculate the discrepancy in the total efficiencies by Eq. 4.9. This discrepancy, and hence the tracking efficiency systematic, depends on the value of f for the track in question. It is roughly proportional to f. Thus, pions will have a small systematic, and kaons will have a large systematic, especially at high momentum. The discrepancy is -0.11±0.04% for f = 5% (a typical value for pions in 2-body D decays) and -0.65±0.24% for f = 25% (a typical value for kaons from 3- or 4-body D decays). To calculate a systematic, we take the central value and uncertainty in quadrature. This gives a systematic of 0.12% for a typical pion and 0.69% for a typical kaon. The systematics will be smaller at higher momentum and larger at lower momentum. Figure 4.31 plots the pion and kaon systematics as a function of momentum, and Table 4.9 lists the numerical values of these systematics. The values of f come from Figure 4.30. The systematics in Figure 4.31 / Table 4.9 should be treated as fully correlated between particles.

This calculation has assumed 100% efficiency for particles that escape the drift chamber before decaying, but we must add a systematic uncertainty for these tracks. To get a systematic, we use the muon efficiency study [13], which found agreement between data and Monte Carlo to within 0.2%. Thus, in addition to the f-dependent systematic calculated above, we add in quadrature 0.2% per track. We have also neglected tracks with $|\cos\theta| \geq 0.9$, and we must add a systematic for them. We found that for both pions and kaons in this $|\cos\theta|$ bin, data and Monte Carlo agree to within 3%. Multiplying 3% by 0.03/0.93 (the fraction of the fiducial volume at polar angles with $|\cos\theta| > 0.9$), we get

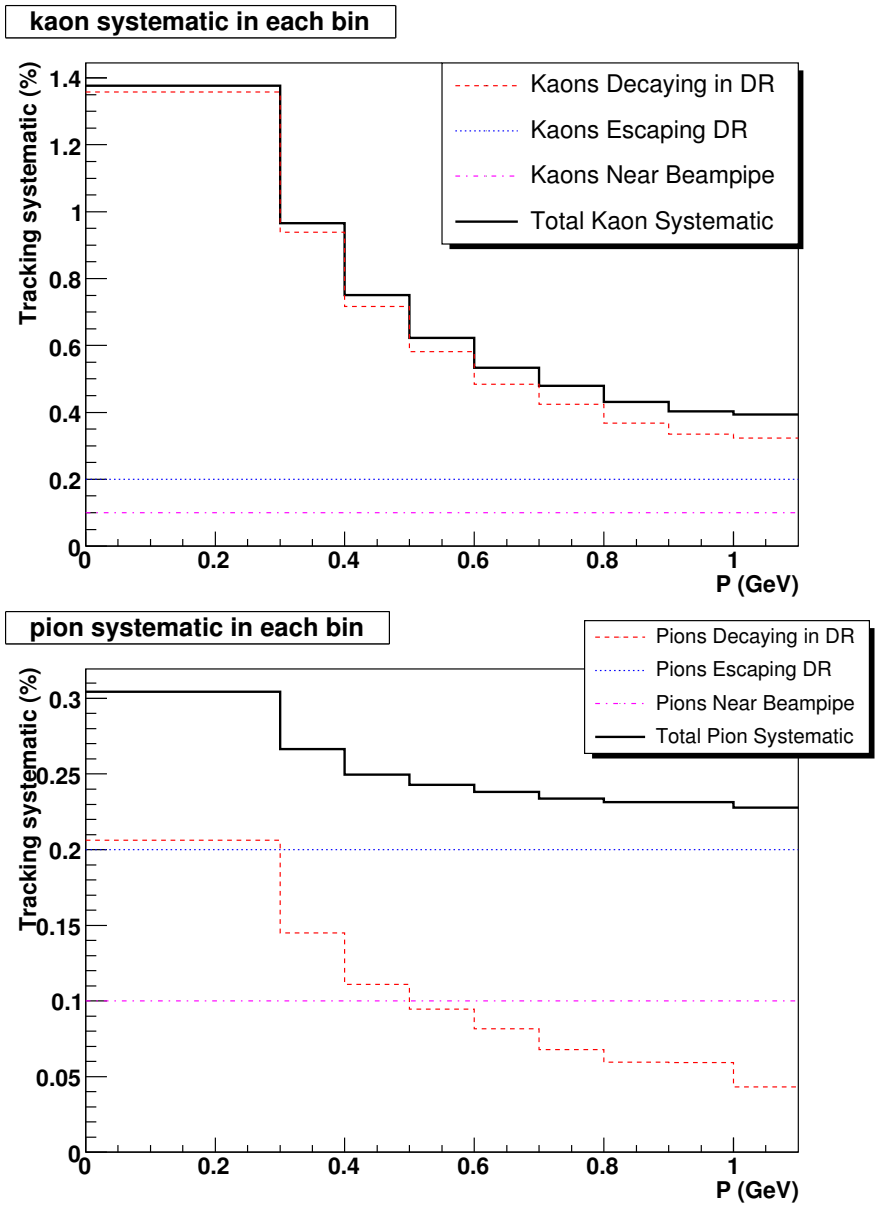

Figure 4.31: Tracking efficiency systematic uncertainties as a function of momentum for kaons (top) and pions (bottom). The values of f come from Figure 4.30. For values below 200 MeV, the systematic is taken from the 200-300 MeV bin, as discussed in the text. The numerical values in these plots are listed in Table 4.9.

Table 4.9: Values of f and momentum-dependent systematic uncertainties. These numbers come from the plots in Figures 4.30 and 4.31.

	KAONS			PIONS		
Momentum Range	f	Decaying K Syst.	Total Syst.	f	Decaying π Syst.	Total Syst.
0-200 MeV	N/A	1.36%	1.38%	N/A	0.21%	0.30%
200-300 MeV	42.4%	1.36%	1.38%	8.4%	0.21%	0.30%
300-400 MeV	32.0%	0.94%	0.97%	6.0%	0.15%	0.27%
400-500 MeV	25.7%	0.72%	0.75%	4.6%	0.11%	0.25%
500-600 MeV	21.5%	0.58%	0.62%	3.9%	0.09%	0.24%
600-700 MeV	18.3%	0.48%	0.53%	3.4%	0.08%	0.24%
700-800 MeV	16.3%	0.42%	0.48%	2.8%	0.07%	0.23%
800-900 MeV	14.3%	0.37%	0.43%	2.5%	0.06%	0.23%
900-1000 MeV	13.1%	0.33%	0.40%	2.5%	0.06%	0.23%
1000-1100 MeV	12.7%	0.32%	0.39%	1.8%	0.04%	0.23%

a systematic of 0.1%. This is added in quadrature for each track. Figure 4.31 shows these systematics along with their combination in quadrature with the momentum-dependent systematic.

This scheme is not applicable to low-momentum tracks, which are often curlers. For tracks below 200 MeV, we need additional input to determine a systematic. For pions, we have evidence from the low-momentum pions in $\psi(2S) \to J/\psi\pi^+\pi^-$ [13, 15] that the agreement between data and Monte Carlo is excellent at low momentum. Therefore we use the systematic from the 200-300 MeV bin for pions below 200 MeV. For kaons, we consider the direct measurements in the lowest-momentum bin to determine the systematic. Averaging the pion and kaon results in this bin, we get a discrepancy of -0.61 ± 0.69 %, or a systematic of 0.92%. This value is well below the systematic from the 200-300 MeV bin – 1.38% – and to be conservative we use 1.38% as the systematic at lower momentum. To summarize, for both pions and kaons we use the systematic for

the 200-300 MeV bin as the systematic below 200 MeV. This is reflected in Figure 4.31 and Table 4.9.

The pion or kaon tracking systematic depends on the particle's momentum. The systematics in Figure 4.31 / Table 4.9 should be combined in an average weighted by the particle's momentum spectrum. In a momentum-dependent analysis, these results should be used for a momentum-dependent systematic. In any analysis, these systematic uncertainties should be treated as correlated between all particles.

We performed a number of cross-checks to see whether the Monte Carlo simulation correctly models the dependence of tracking efficiency on track charge, track polar angle, and the number of particles in the tag D mode. We also checked the sensitivity of the efficiency to the requirement that half of the drift chamber layers traversed by a track contain a hit. All of these cross-checks showed consistency between data and Monte Carlo [16]; therefore they have not affected the tracking systematic.

4.11 K^0_S Reconstruction Efficiency

Measurement of K^0_S reconstruction efficiencies [17] follows a procedure similar to tracking efficiencies, using the $D^0 \to K^0_S\pi^+\pi^-$ decay mode. However, the treatment of the background is more complicated due to the features produced by fake K^0_S candidates.

4.11.1 Signal and Background Components

Fake K^0_S candidates resulting from random combinations of charged pions make the separation of M^2_{miss} distributions into signal and background quite complicated. The fitting procedure involves many steps. Figure 4.32 shows, schematically, the signal and background components present in the missing mass squared distribution, and how they are separated into cases where a K^0_S candidate is or is not found. Figure 4.33 shows the same distribution separated according to whether a K^0_S candidate is found with a mass in the low sideband – a K^0_S candidate mass 14-26 MeV below the nominal K^0_S mass.

Features Produced by Fake K^0_S Candidates

The overall M^2_{miss} distribution, before separation into events in which a K^0_S candidate was or was not found, includes a peak at the K^0_S mass squared ($\sim 0.25\,\text{GeV}^2$) for correct combinations of a tag $\bar{D}^0$ and the two pions from a $D^0 \to K^0_S\pi^+\pi^-$ decay. This peak is shown in red in the schematic at the top of Figure 4.32. There are also a number of backgrounds which do not peak, shown in blue in the schematic:

- $D^0 \to (K^0_S \to \pi^+\pi^-)\pi^+\pi^-$ events in which we (erroneously) use one or both pions from the K^0_S in forming M^2_{miss},
- $D^0 \to \pi^+\pi^-\pi^+\pi^-$ (see Figure 4.34),
- other D^0 decays, and
- fake tag $\bar{D}^0$ candidates.

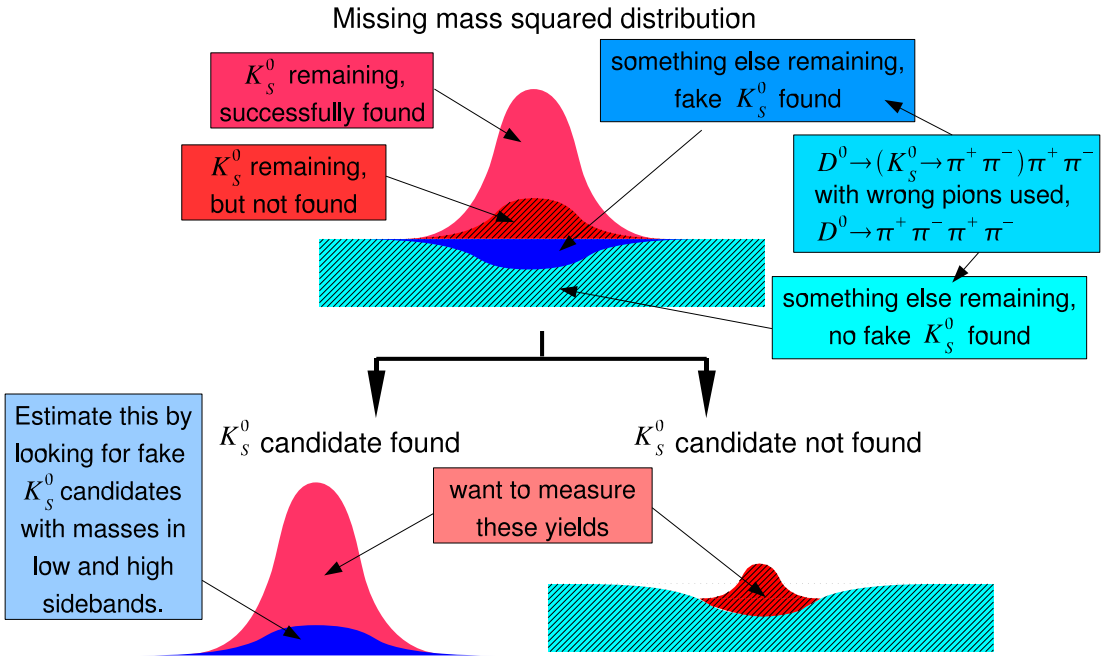

Figure 4.32: Schematic of signal and background components of the missing mass squared distribution, and separation according to whether a K^0_S candidate is or is not found. Signal is shown in red, and background in blue. Hatched areas are those for which no K^0_S candidate is found. The bottom plots show the separation into cases where a K^0_S candidate (whether real or fake) is or is not found. These are the two plots we will fit, with suitable background shapes to represent the dark blue background and the corresponding hole, to determine the number of true K^0_Ss found and not found.

These backgrounds are flat in the region near the signal peak at the K^0_S mass squared. The last two backgrounds, from other D^0 decays and fake tag $\bar{D}^0$ candidates, are greatly reduced by the requirement that there is an extra pair of tracks loosely consistent with the missing momentum.

Thus, the background is mostly $D^0 \to (K^0_S \to \pi^+\pi^-)\pi^+\pi^-$ and $D^0 \to \pi^+\pi^-\pi^+\pi^-$. In these events, the mass of the two pion tracks NOT included in the missing mass squared must equal the missing mass, to within resolution: $M^2_{\rm miss} \approx$

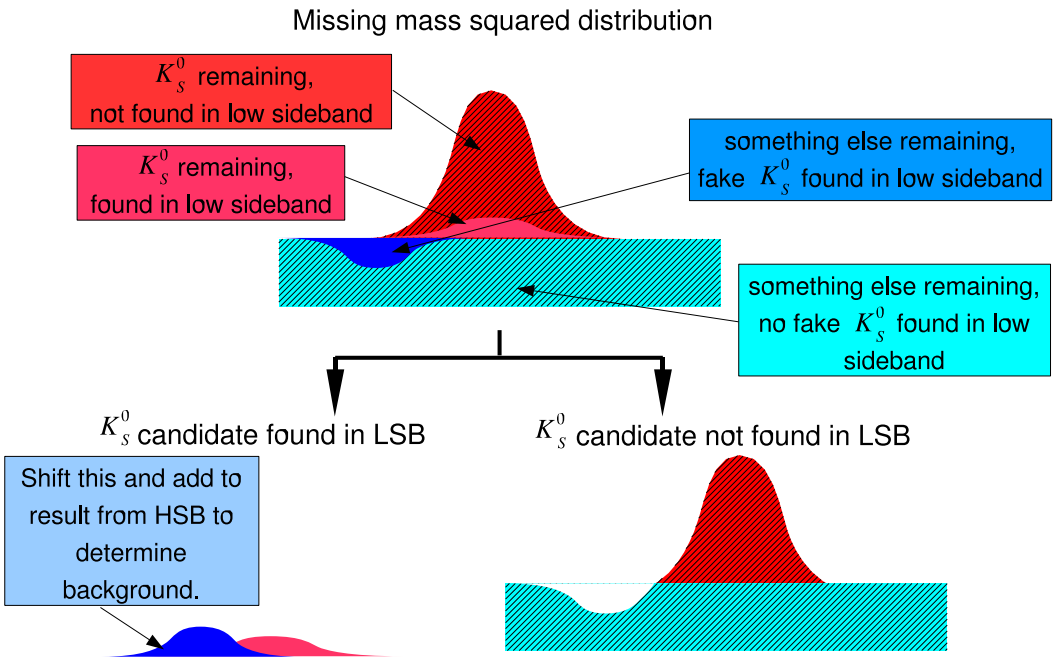

Figure 4.33: Schematic of signal and background components of the missing mass squared distribution, and separation according to whether a K^0_S candidate is or is not found with a mass in the low sideband of K^0_S mass. Signal is shown in red, and background in blue. Hatched areas are those for which no low-sideband K^0_S candidate is found. The bottom plots show the separation into cases where a low-sideband K^0_S candidate is or is not found. We will fit the plot on the bottom left to determine the blue peak yield – how often fake K^0_S candidates will be found. This shape will be shifted right and then used, along with a corresponding peak from the high sideband shifted left, to determine the missing mass distribution for fake K^0_S candidates that pass the K^0_S mass requirement.

$M(\pi^+\pi^-)^2$. If these two pions happen to have a mass near the K^0_S mass, they are likely to form a fake K^0_S candidate. If their mass is far from the K^0_S mass, they will not form a fake K^0_S candidate. Therefore, if we plot the missing mass squared for background events in which a fake K^0_S candidate was found, it will peak at the K^0_S mass squared. The remaining events, in which no K^0_S candidate was found, will form a flat distribution with a hole of the same size and shape

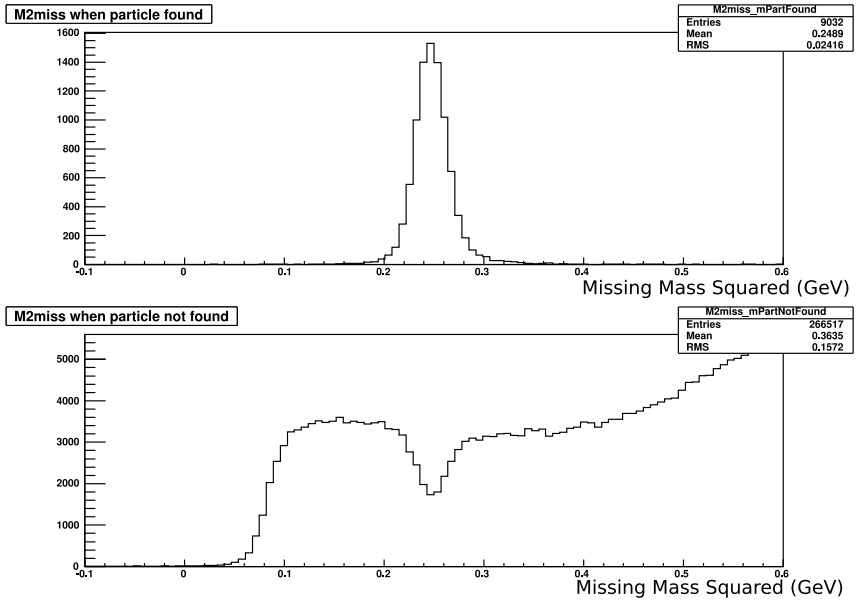

Figure 4.34: $M^2_{\rm miss}$ distributions in $D^0 \to \pi^+\pi^-\pi^+\pi^-$ Monte Carlo. The top plot shows the distribution when a (fake) K^0_S was found, and the lower plot shows the distributon for the events where no K^0_S was found. In this plot we do not require that a pair of extra tracks was found.

at the K^0_S mass squared. This is illustrated in Figure 4.34, which shows these distributions for $D^0 \to \pi^+\pi^-\pi^+\pi^-$ Monte Carlo.

Likewise, when we separate events into those for which a K^0_S candidate is or is not found, the signal peak is divided.

The bottom of Figure 4.32 shows the separation of signal and background components into cases where a K^0_S candidate is or is not found. The fake K^0_S candidates form a peaking background under the efficient peak and leave a hole in the background under the inefficient peak. When we fit for the number of true K^0_Ss found and not found, we will have to include fit components for these background features. We need a procedure to estimate their size and shape.

Estimating the Fake K_S^0 Background

In determining the fake K_S^0 background, we make no assumptions about the composition and resonant substructure of the background, and the procedure allows for differences in these parameters between data and Monte Carlo. Our method uses $\pi^+\pi^-$ pairs whose mass lies in sidebands of the K_S^0 mass. We search for K_S^0 candidates using the usual K_S^0 vertex finder, but look for a reconstructed mass between 14 and 26 MeV from the K_S^0 mass on the low or high side. Figure 4.33 illustrates schematically the separation of signal and background events into cases where a low-sideband K_S^0 candidate is or is not found. For a random pair of pions, the sideband mass ranges are not qualitatively different from the K_S^0 mass signal region (which extends 12 MeV above and below the K_S^0 mass). Fake K_S^0 candidates will be found at the same rate in these two sidebands as in the signal region. The only difference is that the missing mass squared distribution of these candidates will be shifted.

This shift occurs because $M^2_{\rm miss} \approx M(\pi^+\pi^-)^2$. When we shift the $M(\pi^+\pi^-)$ selection region away from $M_{K_S^0}$ by a distance ΔM, we shift $M^2_{\rm miss}$ by

$$\Delta M^2_{\rm miss} = 2M_{K_S^0}(\Delta M) + (\Delta M)^2 \approx (1\ {\rm GeV})(\Delta M) \tag{4.10}$$

where the approximation uses $M_{K_S^0} \approx 0.5$GeV and $\Delta M \ll M_{K_S^0}$. To model the $M^2_{\rm miss}$ distribution for events with a fake K_S^0 found with -12 MeV $<$ M(K_S^0 candidate) $-$ $M_{K_S^0}$ $<$ 0 MeV, we use the $M^2_{\rm miss}$ distribution for those found with -26 MeV $<$ M(K_S^0 candidate) $-$ $M_{K_S^0}$ < -14 MeV, but shift it to the right by (1 GeV)(14 MeV). To model 0 MeV $<$ M(K_S^0 candidate) $-$ $M_{K_S^0}$ $<$ +12 MeV, we use +12 MeV $<$ M(K_S^0 candidate) $-$ $M_{K_S^0}$ $<$ +26 MeV shifted left by (1 GeV)(12 MeV). The means of the shifted peaks are not equal; they should differ by (1 GeV)(12 MeV), since 12 MeV is the difference between the middle of the left and right halves of the

signal region. In summary, we determine the background from fake K^0_S candidates with masses in the K^0_S mass signal region by determining the backgrounds for fake K^0_Ss in the low and high sidebands, shifting those distributions left and right respectively, and summing them.

There is one further complication. Sometimes a real K^0_S is reconstructed with a mass in the low or high K^0_S mass sideband. (This can happen if, for example, one of its tracks is poorly reconstructed.) In this case, the missing mass squared is *not* shifted; $M^2_{\rm miss}$ is calculated from all the other particles in the event, so it still peaks at the K^0_S mass squared. When we plot $M^2_{\rm miss}$ for data or generic Monte Carlo events in which a K^0_S candidate was found in a K^0_S mass sideband, this plot will be the sum of a peak at the K^0_S mass squared from real K^0_Ss and a shifted peak from fake K^0_S candidates. This is illustrated for the low sideband at the bottom left of Figure 4.33; the high sideband is similar, but with the blue peak to the right of the red one. We want to determine the contribution from fake K^0_Ss (the blue component in the diagram), leaving out the real K^0_Ss (the red component), when determining the background. To do this, we first get peak shapes from Monte Carlo simulations of $D^0 \to K^0_S\pi^+\pi^-$ and $D^0 \to \pi^+\pi^-\pi^+\pi^-$ events, and then we use these shapes in data or generic Monte Carlo when determining background.

4.11.2 Fits

Due to the complexity of determining the backgrounds, the fitting procedure is fairly complicated. Below we list the steps and refer to corresponding plots. In these plots, there is no requirement on the magnitude of the missing (K^0_S)

momentum; later we will perform the analysis separately in momentum bins. The fitting steps are:

1. Fit M^2_{miss} for simulated $D^0 \to \pi^+\pi^-\pi^+\pi^-$ events in which a (fake) K^0_S candidate was found in the low sideband of the K^0_S mass. This is a peak to the left of the K^0_S mass squared. It is fit with a two-sided Crystal Ball shape. The peak shape obtained from this plot will be used in fitting data and generic Monte Carlo. See the top left plot of Figure 4.35.

2. Fit simulated $D^0 \to K^0_S\pi^+\pi^-$ events in which a (real) K^0_S candidate was found in the low sideband of the K^0_S mass. Events are included in the plot only if, according to Monte Carlo truth, the two pions used to form M^2_{miss} come from the D^0 and not from the K^0_S. This eliminates background events from this sample. The peak is fit with a two-sided Crystal Ball. The peak shape obtained from this plot will be used in fitting data and generic Monte Carlo. See the top right plot of Figure 4.35.

3. In both data and generic Monte Carlo, fit events in which a K^0_S candidate was found in the low sideband of the K^0_S mass. Use the two peak shapes obtained previously, but let the yields float. The shape and size of the peak on the left, from fake K^0_S candidates, will be used later in determining the background from fake K^0_S candidates with masses in the K^0_S mass signal region. See the top row of Figure 4.36.

4. Repeat the same procedure with K^0_S candidates in the high sideband of the K^0_S mass. See the bottom rows of Figures 4.35 and 4.36. Note that, on the left side of Figure 4.35, the difference between the means for the high and low sidebands is 0.0401 ± 0.0004 GeV^2, consistent with the expected difference of 0.04 GeV^2 based on the 40 MeV difference between the mid-

dle of the two sidebands: $2M_{K_S^0}(\Delta M) \approx 2(0.5\text{ GeV})(40\text{ MeV}) = 0.04\text{ GeV}^2$. This confirms that the analysis of the shifts in the sideband distributions is correct.

5. Separately for data and generic Monte Carlo, shift and then sum the two peaks from fake K_S^0 candidates in the sideband regions of the K_S^0 mass. Shift the low sideband right by 14 MeV and the high sideband left by 14 MeV. The sum of these shifted peaks is the M^2_{miss} distribution for fake K_S^0 candidates with masses in the signal region of the K_S^0 mass. This is the appropriate background for use when fitting events in which a K_S^0 candidate was found (with a mass in the signal region), and it is also the size and shape of the hole in the background for events in which no K_S^0 candidate was found.

6. Separately for data and generic Monte Carlo, fit events in which a K_S^0 candidate was found. Use the background shape obtained in the previous step. For the signal peak, use a two-sided Crystal Ball shape. The yield of this peak is the number of true K_S^0s found. See the top row of Figure 4.37.

7. Separately for data and generic Monte Carlo, fit events in which no K_S^0 candidate was found with a mass in the signal region. The background is a linear function with a hole removed. This hole is the same shape and size as the background used in the previous step; it represents the background events in which a fake K_S^0 candidate was found. For the signal peak, use the peak shape obtained in the previous step. The yield of this peak is the number of true K_S^0s not found. See the bottom row of Figure 4.37.

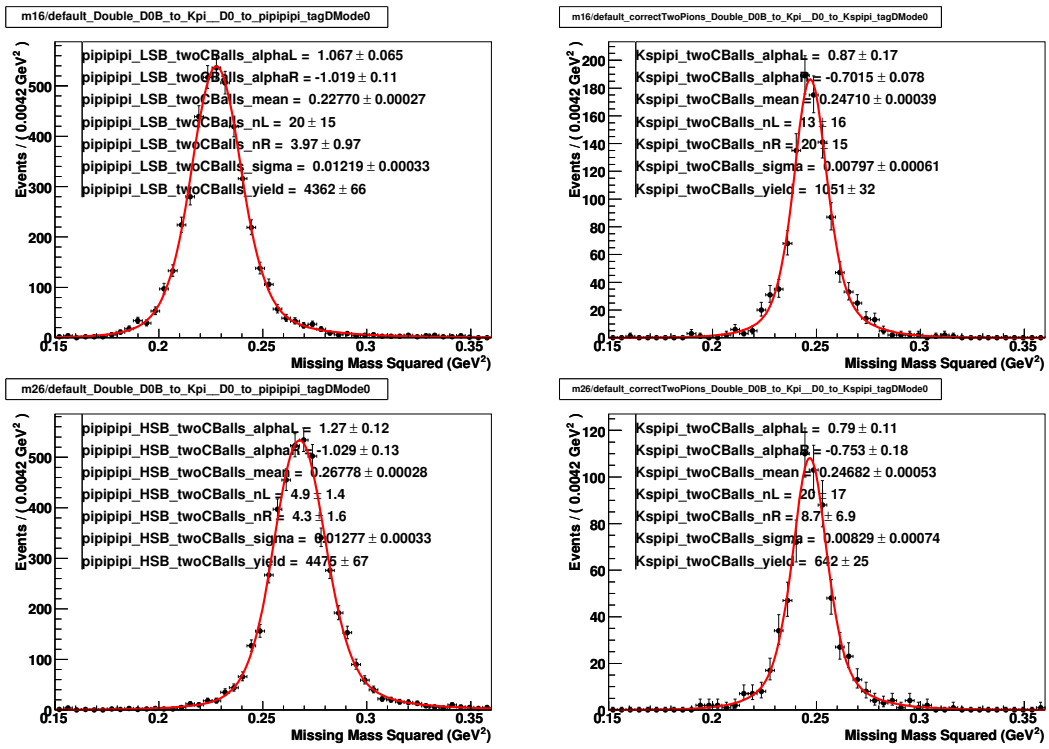

Figure 4.35: Fits to $D^0 \to \pi^+\pi^-\pi^+\pi^-$ (left column) and $D^0 \to K^0_S\pi^+\pi^-$ (right column) Monte Carlo for events in which a K^0_S candidate was found in the low (top row) or high (bottom row) sideband of the K^0_S mass. In $D^0 \to K^0_S\pi^+\pi^-$, events are included in the plot only if, according to Monte Carlo truth, the two pions used to form $M^2_{\rm miss}$ come from the D^0 and not from the K^0_S. These plots correspond to fitting steps 1, 2, and 4.

4.11.3 Calculation of K^0_S Reconstruction Efficiency

Having determined the number of true K^0_Ss found or not found, we can calculate the K^0_S-finding efficiency in data and generic Monte Carlo. The efficiency ϵ is calculated from the number of events in which the missing K^0_S is found, denoted E ("efficient"), and the number in which it is not found, denoted I ("inefficient"). Here we repeat Equations 4.1 and 4.2 for the efficiency and its uncertainty:

$$\epsilon \equiv \frac{E}{E+I} = \frac{1}{1+I/E} \tag{4.11}$$

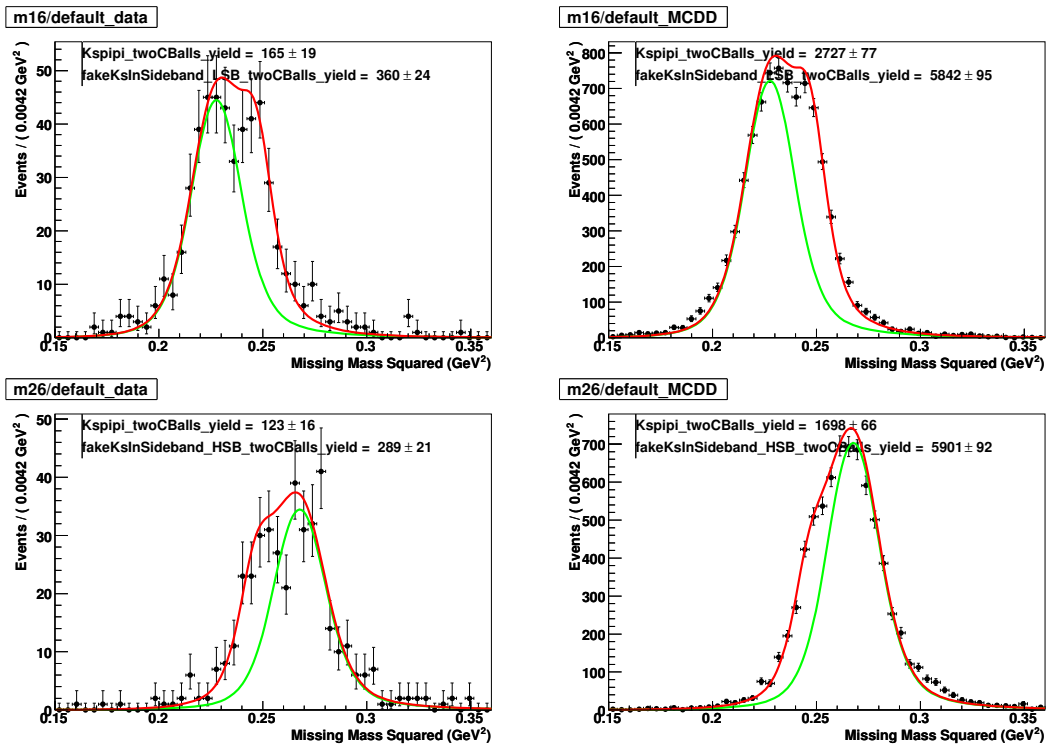

Figure 4.36: Fits to data (left column) and generic Monte Carlo (right column) for events in which a K^0_S candidate was found in the low (top row) or high (bottom row) sideband of the K^0_S mass. These fits use the peak shapes from Figure 4.35. The green curve is the contribution from fake K^0_S candidates; the remaining area is the contribution from true K^0_Ss with a reconstructed mass in the low or high sideband. These plots correspond to fitting steps 3 and 4.

$$\begin{aligned} \delta\epsilon &= \frac{1}{(E+I)^2}\sqrt{E^2(\delta I)^2 + I^2(\delta E)^2} \\ &= \epsilon(1-\epsilon)\sqrt{\left(\frac{\delta E}{E}\right)^2 + \left(\frac{\delta I}{I}\right)^2} \end{aligned} \tag{4.12}$$

Our fits take the size of the background peak and hole as given, with zero uncertainty. Therfore, in addition to the uncertainties reported by the final fits, there is an uncertainty due to the size of the background from fake K^0_S candidates. As this background becomes larger, it reduces E and increases I, and these changes are nearly identical to the change in the background. (That is, the size of the

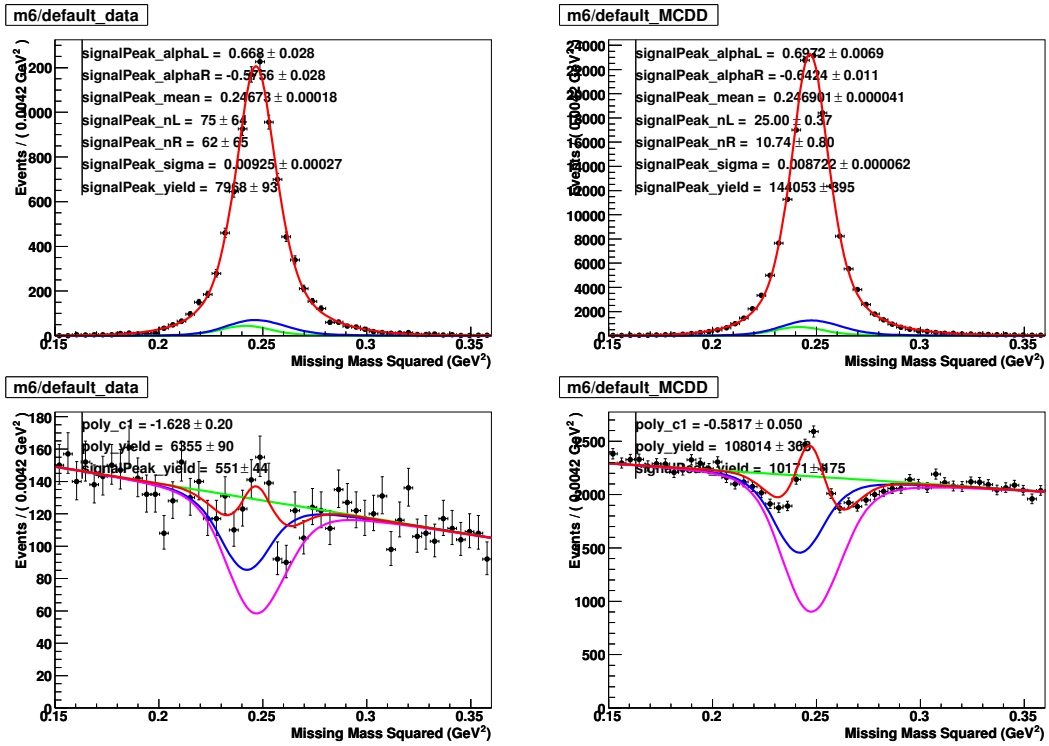

Figure 4.37: Fits to data (left column) and generic Monte Carlo (right column) for events in which a K^0_S candidate (in the K^0_S mass signal region) was found (top row) or was not found (bottom row). For the background peak and hole, these fits use shifted peak shapes from the left column of Figure 4.35 and yields from Figure 4.36. In the top plots, the blue curve is the contribution from fake K^0_S candidates. In the bottom plots, the green line is the linear background shape, the purple line is the background after removal of the events in which a fake K^0_S candidate was found, and the red line is the total fit function after adding the signal peak. These plots correspond to fitting steps 6 and 7.

background is almost perfectly anti-correlated with E and correlated with I.) Thus, $E + I$ is insensitive to the size of this background, and the uncertainty in E due to this background equals the uncertainty on the background yield. If we call this uncertainty δB, then the uncertainty on ϵ due to the background is $\delta B/(E + I)$. We add this in quadrature to the uncertainty in Eq. 4.12 to determine the uncertainty on the efficiency.

We also evaluate systematics due to uncertainties in the shape of the background. First, we consider the possibility that Monte Carlo does not accurately predict the width of the background in data. In data only, we try widening by 10% the background peak shapes obtained from signal Monte Carlo (from Figure 4.35); 10% is a conservative upper bound on the difference in peak widths between data and Monte Carlo. The rest of the analysis follows the usual procedure, and we take the difference between the resulting efficiency and the default as a systematic uncertainty.

We also considered the relative size of the contributions from the shifted low-sideband and high-sideband peaks. We have taken the yields of these two peaks from fits to the low and high sideband. We tried, as an alternate background shape, a sum of these two peaks with equal areas in each. The sum of their yields was left unchanged. We performed our fits for the efficient and inefficient yields with these altered shapes, and we computed the efficiencies in data and Monte Carlo. This systematic was found to be negligible.

Table 4.10 shows the yields and the calculated efficiencies. The efficiencies are high, as expected. In fact, much of the inefficiency may be explained by cases where the K^0_S daughter pions were found, but reconstructed poorly. Then they would pass the loose requirement on pairs of extra tracks, but not the tighter

Table 4.10: K_S^0 yields and efficiencies. The statistical uncertainties on the efficient and inefficient K_S^0 yields do not include uncertainty due to the number of fake K_S^0s; this uncertainty is included in evaluating the statistical uncertainty on the efficiency. The systematic uncertainty in data comes from widening the background shapes by 10%.

	Data	Monte Carlo
Number of fake K_S^0s	649 ± 32	11743 ± 132
Number of real K_S^0s found	7968 ± 93	144053 ± 395
Number of real K_S^0s not found	551 ± 44	10171 ± 175
Efficiency (%)	93.53± 0.62 ± 0.32	93.41 ± 0.14
$\epsilon_{MC}/\epsilon_{data} - 1$	-0.14 ± 0.67 ± 0.35 % (-0.2σ)	

K_S^0 selection requirements. For example, if one of the pions decayed to $\mu\nu_\mu$, the muon track may help produce a track with approximately correct momentum that passes the loose requirement but fails the vertex finder. Regardless of the source of inefficiency, data and Monte Carlo are consistent.

4.11.4 Results in Four Momentum Bins

To examine the possibility of momentum dependence in the K_S^0 reconstruction systematic, we perform this analysis in four momentum bins. They are separated according to the predicted momentum of the missing K_S^0 – that is, the magnitude of the missing momentum. The bins are $p_{K_S^0} < 300$ MeV, $300 \leq p_{K_S^0} < 500$ MeV, $500 \leq p_{K_S^0} < 700$ MeV, and 700 MeV $\leq p_{K_S^0}$. The fitting procedure is identical to the procedure described above for all momentum bins. The plots are not shown; they are very similar to the plots for all momentum bins together. The yields and efficiencies for all bins are shown in Table 4.11. In all momentum bins, data and Monte Carlo are consistent.

Table 4.11: K^0_S yields and efficiencies in four momentum bins. The statistical uncertainties on the efficient and inefficient K^0_S yields do not include uncertainty due to the number of fake K^0_Ss; this uncertainty is included in evaluating the statistical uncertainty on the efficiency.

	Data	Monte Carlo
$p_{K^0_S} < 300$ MeV		
Number of fake K^0_Ss	76 ± 10	908 ± 34
Number of real K^0_Ss found	1852 ± 44	34016 ± 187
Number of real K^0_Ss not found	177 ± 16	2839 ± 61
Efficiency (%)	91.28± 0.88 ± 0.04	92.30 ± 0.18
$\epsilon_{MC}/\epsilon_{data} - 1$	+1.12 ± 0.99 ± 0.04 % (+1.1σ)	
$300 \leq p_{K^0_S} < 500$ MeV		
Number of fake K^0_Ss	98 ± 12	2072 ± 53
Number of real K^0_Ss found	1801 ± 44	29121 ± 177
Number of real K^0_Ss not found	119 ± 17	2005 ± 67
Efficiency (%)	93.80± 1.04 ± 0.09	93.56 ± 0.27
$\epsilon_{MC}/\epsilon_{data} - 1$	-0.26 ± 1.14 ± 0.09 % (-0.2σ)	
$500 \leq p_{K^0_S} < 700$ MeV		
Number of fake K^0_Ss	179 ± 17	4140 ± 79
Number of real K^0_Ss found	1771 ± 44	39403 ± 209
Number of real K^0_Ss not found	105 ± 25	2547 ± 109
Efficiency (%)	94.40± 1.56 ± 0.29	93.93 ± 0.31
$\epsilon_{MC}/\epsilon_{data} - 1$	-0.50 ± 1.67 ± 0.30 % (-0.3σ)	
700 MeV $\leq p_{K^0_S}$		
Number of fake K^0_Ss	299 ± 23	4603 ± 89
Number of real K^0_Ss found	2544 ± 53	41584 ± 215
Number of real K^0_Ss not found	121 ± 33	2514 ± 127
Efficiency (%)	95.46± 1.47 ± 0.19	94.30 ± 0.34
$\epsilon_{MC}/\epsilon_{data} - 1$	-1.22 ± 1.57 ± 0.20 % (-0.8σ)	

The efficiencies and data-Monte Carlo discrepancies are plotted in Figure 4.38. The effciency has a modest dependence on momentum.

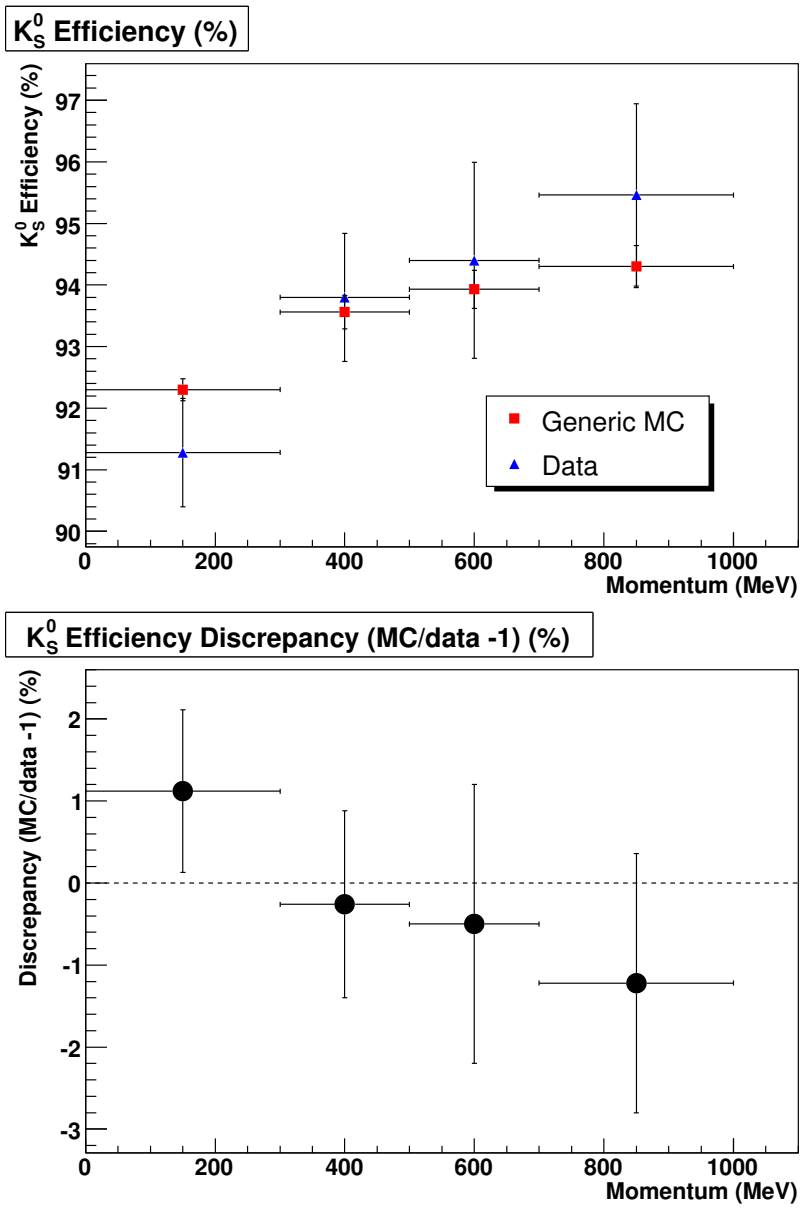

Figure 4.38: Measurements (in %) of the K^0_S efficiency (top) and the data-Monte Carlo discrepancy $\epsilon_{\mathrm{MC}}/\epsilon_{\mathrm{data}} - 1$ (bottom) in different momentum bins.

4.11.5 $K^0_S \to \pi^+\pi^-$ Reconstruction Systematic

We obtain the K^0_S reconstruction systematic from the data-Monte Carlo discrepancy determined with all momentum bins combined. This discrepancy is -0.14 ± 0.67 ± 0.35 %. We have no reason to expect a difference between data and Monte Carlo, and the measured discrepancy is consistent with zero. Therefore, we apply no correction to the Monte Carlo for K^0_S efficiency. We combine the central value and uncertainty of the discrepancy in quadrature to obtain a systematic. This gives a 0.8% systematic for K^0_S reconstruction, in addition to track-finding systematics for the two tracks.

CHAPTER 5

MEASUREMENT OF BRANCHING FRACTION FOR $D^+ \to K_L^0\pi^+$ AND COMPARISON TO $D^+ \to K_S^0\pi^+$

5.1 Introduction

In the past, it has typically been assumed that the branching fractions for $D^+ \to K^0_L\pi^+$ and $D^+ \to K^0_S\pi^+$ are equal. However, as Bigi and Yamamoto first pointed out [18], in fact quantum interference produces a small difference between them. This chapter describes the first measurement of the branching fraction $\mathcal{B}(D^+ \to K^0_L\pi^+)$ and compares the result to $\mathcal{B}(D^+ \to K^0_S\pi^+)$.

We expect an asymmetry in these branching fractions due to interference between the amplitudes for $D^+ \to \bar{K}^0\pi^+$ and $D^+ \to K^0\pi^+$, as shown in Figure 5.1. The primary process contributing to $D^+ \to K^0_L\pi^+$ and $D^+ \to K^0_S\pi^+$ is $D^+ \to \bar{K}^0\pi^+$. Two tree-level diagrams contribute to this process: an external spectator diagram and a (color-suppressed) internal spectator diagram. The second diagram interferes destructively with the first; this is an example of the destructive interference believed to reduce the D^+ decay rate relative to D^0.

If only $D^+ \to \bar{K}^0\pi^+$ contributed to the decays $D^+ \to K^0_L\pi^+$ and $D^+ \to K^0_S\pi^+$, then their branching fractions would be equal. However, there is also a small contribution from the doubly-Cabibbo-suppressed process $D^+ \to K^0\pi^+$. This process has a color-suppressed internal spectator diagram which contains factors of $\pm\sin\theta_C$ at the two W vertices, where θ_C is the Cabibbo angle. The corresponding Cabibbo-favored diagram contains two factors of $\cos\theta_C$ instead, so the two diagrams differ by a factor of $-\tan^2\theta_C$ in the SU(3) limit. A (helicity-suppressed) annihilation diagram also contributes to this decay.

The combination of amplitudes for $\bar{K}^0\pi^+$ and $K^0\pi^+$ produces interference in the formation of the physical final states $K^0_L\pi^+ = 1/\sqrt{2}(K^0 - \bar{K}^0)\pi^+$ and $K^0_S\pi^+ = 1/\sqrt{2}(K^0 + \bar{K}^0)\pi^+$. The sign of this interference is opposite for K^0_L and K^0_S, so

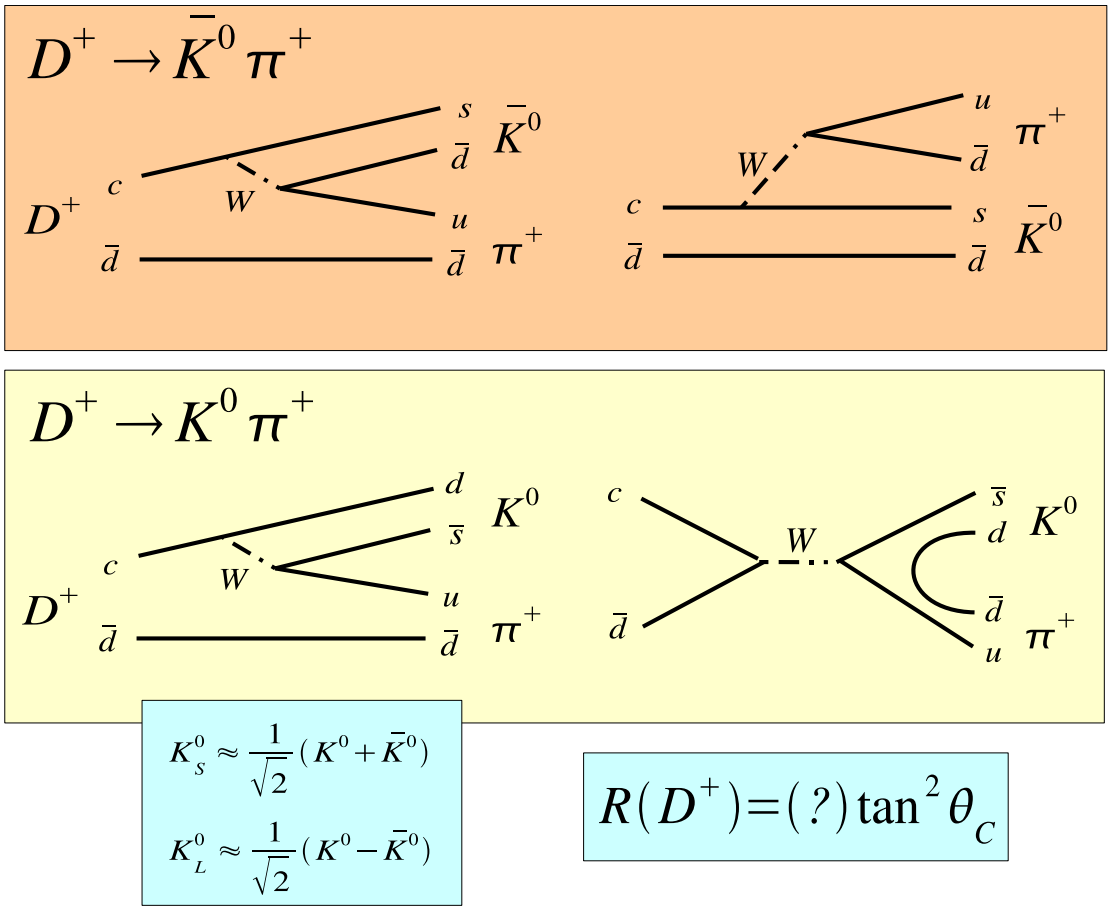

Figure 5.1: Diagrams contributing to $D^+ \to K_L^0\pi^+$ and $D^+ \to K_S^0\pi^+$.

$\mathcal{B}(D^+ \to K_L^0\pi^+)$ and $\mathcal{B}(D^+ \to K_S^0\pi^+)$ should not in general be equal. The scale of the asymmetry is set by the double Cabibbo suppression factor $\tan^2\theta_C \approx 0.05$. However, the exact asymmetry is difficult to predict theoretically.

In contrast, a simple prediction can be made for asymmetry between the corresponding neutral decays $\mathcal{B}(D^0 \to K_L^0\pi^0)$ and $\mathcal{B}(D^0 \to K_S^0\pi^0)$. The amplitudes for $D^0 \to \bar{K}^0\pi^0$ and $D^0 \to K^0\pi^0$ also have color-suppressed, internal spectator diagrams; they differ from the D^+ decays only in the identity of the spectator quark. Both decays also receive contributions from exchange diagrams. For both types of diagram, the two decay amplitudes differ only by the double Cabibbo sup-

pression factor $-\tan^2\theta_C$. This value for the amplitude ratio is also implied by symmetry under the U-spin subgroup of SU(3), which is relatively insensitive to SU(3) breaking [19]. This amplitude ratio predicts that the asymmetry between $\mathcal{B}(D^0 \to K^0_S\pi^0)$ and $\mathcal{B}(D^0 \to K^0_L\pi^0)$ is

$$R(D^0) \equiv \frac{\mathcal{B}(D^0 \to K^0_S\pi^0) - \mathcal{B}(D^0 \to K^0_L\pi^0)}{\mathcal{B}(D^0 \to K^0_S\pi^0) + \mathcal{B}(D^0 \to K^0_L\pi^0)} = 2\tan^2\theta_C = 0.109 \pm 0.001 \qquad (5.1)$$

where the value of θ_C is taken from the Particle Data Group [1]. The asymmetry has been measured to be $R(D^0) = 0.108 \pm 0.025 \pm 0.024$, consistent with this prediction [6].

For the corresponding D^+ asymmetry, no simple prediction can be made because the Cabibbo-favored and doubly-Cabibbo-suppressed decays have different diagrams, as shown in Fig. 5.1. (Equivalently, U-spin makes no prediction for the amplitude ratio.) $D^+ \to \bar{K}^0\pi^+$ includes an external spectator diagram, and $D^+ \to K^0\pi^+$ includes an annihilation diagram. These diagrams, combined with the topological analysis of Cabibbo-favored $D \to K\pi$ decays described in Chapter 1, suggest the potential that $R(D^+)$ may be larger than $R(D^0)$. For both D^0 and D^+, the doubly-Cabibbo-suppressed amplitude $D \to K^0\pi$ is dominated by the internal spectator diagram, and that amplitude equals the Cabibbo-favored internal diagram multiplied by $-\tan^2\theta_C \approx -0.05$. But for $D^+ \to \bar{K}^0\pi^+$, the external spectator diagram interferes destructively with the internal diagram, as discussed in Chapter 1. Therefore the magnitude of the amplitude ratio $\mathcal{A}(D \to K^0\pi)/\mathcal{A}(D \to \bar{K}^0\pi)$ should be larger for D^+ than for D^0, leading to a larger asymmetry $R(D^+)$. However, the asymmetry also depends on the relative phase between $D^+ \to \bar{K}^0\pi^+$ and $D^+ \to K^0\pi^+$; if this phase is close to 90 degrees, the asymmetry will be close to zero.

While no simple prediction of $R(D^+)$ is possible, it is possible to make a

prediction with more input data and a more sophisticated theoretical treatment [20, 4].

This analysis aims to measure the asymmetry between $\mathcal{B}(D^+ \to K^0_L\pi^+)$ and $\mathcal{B}(D^+ \to K^0_S\pi^+)$ by measuring $\mathcal{B}(D^+ \to K^0_L\pi^+)$ and comparing to a separate measurement of $\mathcal{B}(D^+ \to K^0_S\pi^+)$.

We find $D^+ \to K^0_L\pi^+$ events using the same missing mass technique used for the efficiency studies in the previous chapter. We form the missing mass squared of combinations of D^- and π^+ candidates:

$$M^2_{\text{miss}} = (p_{\text{tot}} - p_{D^-} - p_{\pi^+})^2 \tag{5.2}$$

where p_{tot} is the four-momentum of the initial state, p_{D^-} is the four-momentum of the reconstructed D^-, and p_{π^+} is the four-momentum of the pion candidate. A peak at the K^0_L mass squared corresponds to our signal events. The number of D^- tags is determined from the beam constrained mass distribution of D^- candidates.

$D^+ \to K^0_L\pi^+$ and $D^+ \to K^0_S\pi^+$ decays each produce a peak at the same location – the K^0 mass squared. To eliminate $D^+ \to K^0_S\pi^+$ decays, we veto events containing extra tracks or π^0s beyond those used to form the D^- and π^+. This removes most $D^+ \to K^0_S\pi^+$ events since the K^0_S produces two extra charged or neutral pions. The $D^+ \to K^0_S\pi^+$ events that survive this veto are treated as a background.

The remainder of this chapter is organized as follows: First, we describe the data and Monte Carlo samples used and the event selection criteria. Next, we describe the calculation used to obtain the branching fraction. We then show how yields and efficiencies are obtained from fitting beam constrained mass and missing mass squared distributions. Finally, we consider the systematic uncer-

tainties and give a final result for $\mathcal{B}(D^+ \to K^0_L\pi^+)$. By combining these results with a separate measurement of $\mathcal{B}(D^+ \to K^0_S\pi^+)$, we determine the asymmetry between $D^+ \to K^0_L\pi^+$ and $D^+ \to K^0_S\pi^+$.

5.2 Data and Monte Carlo Samples

The data sample represents an integrated luminosity of 281 pb^{-1}, smaller than the 818 pb^{-1} sample used for determining efficiency systematics. Statistical and systematic uncertainties make approximately equal contributions to this measurement, so tripling the dataset would not greatly improve the precision of the result.

We generate signal Monte Carlo samples to calculate efficiencies. A generic Monte Carlo sample representing 5.5 times the number of $D\overline{D}$ events as in data is used to test and validate the analysis procedure, but it has no impact on the final result.

5.3 Event and Candidate Selection

As in the efficiency analysis, analogous treatment of charge conjugates is implied in the selection criteria.

We use the standard requirements described in Chapter 3 to obtain tag D^- candidates in the following decay modes:

- $K^+\pi^-\pi^-$

Table 5.1: ΔE requirements used for each tag D^- mode.

Tag mode	Requirement
$D^- \to K^+\pi^-\pi^-$	-0.025 < ΔE < 0.025 GeV
$D^- \to K^+\pi^-\pi^-\pi^0$	-0.035 < ΔE < 0.035 GeV
$D^- \to K^0_S\pi^-$	-0.025 < ΔE < 0.025 GeV
$D^- \to K^0_S\pi^-\pi^0$	-0.040 < ΔE < 0.035 GeV
$D^- \to K^0_S\pi^-\pi^-\pi^+$	-0.018 < ΔE < 0.018 GeV
$D^- \to K^+K^-\pi^-$	-0.018 < ΔE < 0.018 GeV

- $K^+\pi^-\pi^-\pi^0$
- $K^0_S\pi^-$
- $K^0_S\pi^-\pi^0$
- $K^0_S\pi^-\pi^-\pi^+$
- $K^+K^-\pi^-$

We impose requirements on ΔE, as listed in Table 5.1. These ranges have been chosen to include the entire ΔE peak in each mode. If there are multiple D^- candidates satisfying $M_{\rm BC} > 1.83\,{\rm GeV}$ in an event with the same charge and decay mode, only the one with the smallest $|\Delta E|$ is kept for further analysis. We calculate $M_{\rm BC}$ for each candidate and use this variable to determine the number of tag D^-s.

Each D^- candidate that passes the $M_{\rm BC}$ requirements shown in Table 5.2 is then combined with one π^+ candidate, forming multiple candidates if there are multiple π^+s. The missing mass squared of this combination is then calculated, with the D^- momentum constrained to give $M_{\rm BC} = M_{D^-}$ in the same way as in the efficiency analysis. The peak in the $M^2_{\rm miss}$ distribution at the K^0 mass squared corresponds to $D^+ \to K^0_L\pi^+$ and $D^+ \to K^0_S\pi^+$ events.

Table 5.2: $M_{\rm BC}$ requirements used for each D^- tag mode.

Tag mode	Requirement
$D^- \to K^+\pi^-\pi^-$	$1.864 < M_{\rm BC} < 1.879$ GeV
$D^- \to K^+\pi^-\pi^-\pi^0$	$1.864 < M_{\rm BC} < 1.877$ GeV
$D^- \to K^0_S\pi^-$	$1.864 < M_{\rm BC} < 1.879$ GeV
$D^- \to K^0_S\pi^-\pi^0$	$1.863 < M_{\rm BC} < 1.877$ GeV
$D^- \to K^0_S\pi^-\pi^-\pi^+$	$1.865 < M_{\rm BC} < 1.876$ GeV
$D^- \to K^+K^-\pi^-$	$1.864 < M_{\rm BC} < 1.877$ GeV

The preceding requirements do not discriminate between $D^+ \to K^0_L\pi^+$ and $D^+ \to K^0_S\pi^+$ events (though the tag D^- reconstruction efficiency may be slightly lower when the signal side has a K^0_S rather than a K^0_L). Therefore, additional requirements are included to veto $D^+ \to K^0_S\pi^+$ decays. These vetoes look for the daughter pions of the K^0_S.

Approximately 2/3 of K^0_Ss decay to $\pi^+\pi^-$. To remove these decays, an event is vetoed if it contains at least one extra track not already used in the tag D^- or the π^+. This track must pass the following requirements:

- The distance from the interaction point must be less than 20 cm. This is looser than the standard track selection requirements because the K^0_S will travel some distance before decaying. However, it is still tight enough to ignore obvious garbage tracks far from the interaction point.
- The track must pass all other standard quality requirements, but no particle identification requirements.
- It must be approved by the Trkman software package, which rejects tracks that appear likely to be fake.

This veto is very effective. It removes over 99% of $D^+ \to (K^0_S \to \pi^+\pi^-)\pi^+$ events

and only about 2% of $D^+ \to K^0_L\pi^+$ events.

About 1/3 of K^0_Ss decay to $\pi^0\pi^0$. To remove these decays, an event is vetoed if it contains at least one extra π^0 not already used in the tag D^-. This π^0 must pass the following requirements:

- It must pass the standard π^0 requirements.
- Both showers have energy greater than 80 MeV. (This is tightened from the default value of 30 MeV.)
- It must be approved by the Splitoff software package, which rejects showers that appear to come from splitoffs of hadronic interactions in the calorimeter.

This veto removes approximately 60% of $D^+ \to (K^0_S \to \pi^0\pi^0)\pi^+$ events and about 2% of $D^+ \to K^0_L\pi^+$ events.

Overall the extra track and extra π^0 vetoes remove about 90% of $D^+ \to K^0_S\pi^+$ events and 4% of $D^+ \to K^0_L\pi^+$ events. They also reduce many of the other backgrounds present in the missing mass squared plot.

5.4 Calculation of Branching Fraction

If we ignore the possibility that the D^- tag reconstruction efficiency may depend on how the D^+ decays, the branching fraction $\mathcal{B}(D^+ \to K^0_L\pi^+)$ is

$$\mathcal{B}(D^+ \to K^0_L\pi^+) = \frac{Y(D^+ \to K^0_L\pi^+)}{Y(D^-)\,\epsilon} \tag{5.3}$$

where $Y(D^-)$ is the number of D^- tags reconstructed, $Y(D^+ \to K^0_L\pi^+)$ is the number of $K^0_L\pi^+$ decays found, and ϵ is the efficiency for reconstructing $D^+ \to K^0_L\pi^+$

given that the tag D^- was found. This efficiency is approximately equal to the π^+ reconstruction efficiency. However, Eq. 5.3 is not quite correct. In fact, the D^- reconstuction efficiency is higher in events where D^+ decays to $K^0_L\pi^+$ because this decay is relatively clean and does not interfere with D^- reconstruction as much as other D^+ decays. Thus the sample of events with a reconstructed tag has a higher proportion of $D^+ \to K^0_L\pi^+$ decays than a truly random sample of D^+s.

To deal with the bias in Eq. 5.3, we derive an expression with no assumption about the tag reconstruction efficiency:

$$\mathcal{B}(D^+ \to K^0_L\pi^+) = \frac{D^+ \to K^0_L\pi^+ \text{ produced}}{D^+ \text{ produced}} \tag{5.4}$$

$$= \frac{Y(D^+ \to K^0_L\pi^+)/\epsilon(D^+ \to K^0_L\pi^+)}{Y(D^-)/\epsilon(D^-)} \tag{5.5}$$

Here, $\epsilon(D^-)$ is the efficiency for reconstructing a tag D^- when the D^+ decays generically (that is, to any final state, not necessarily $K^0_L\pi^+$), and $\epsilon(D^+ \to K^0_L\pi^+)$ is the efficiency for reconstructing a tag D^- and then finding a $K^0_L\pi^+$ decay in an event where D^+ truly does decay to $K^0_L\pi^+$. We may divide the two efficiencies into constituent efficiencies:

$$\begin{aligned}\epsilon(D^-) &= \epsilon(D^-|D^+ \text{ decays to } K^0_L\pi^+)\mathcal{B}(D^+ \to K^0_L\pi^+) \\ &\quad +\epsilon(D^-|D^+ \text{ does not decay to } K^0_L\pi^+)[1 - \mathcal{B}(K^0_L\pi^+)] \end{aligned} \tag{5.6}$$

$$\epsilon(D^+ \to K^0_L\pi^+) = \epsilon(K^0_L\pi^+|D^- \text{ found })\epsilon(D^-|D^+ \text{ decays to } K^0_L\pi^+) \tag{5.7}$$

where $\epsilon(A|B)$ is the efficiency for reconstructing A given that B is true. Then

$$\frac{\epsilon(D^-)}{\epsilon(D^+ \to K^0_L\pi^+)} = \frac{R}{\epsilon} \tag{5.8}$$

where

$$\epsilon \equiv \epsilon(K^0_L\pi^+|D^- \text{ found }) \tag{5.9}$$

and

$$R \equiv \mathcal{B}(D^+ \to K_L^0\pi^+) + (1 - \mathcal{B}(D^+ \to K_L^0\pi^+))\frac{\epsilon(D^-|D^+ \text{ does not decay to } K_L^0\pi^+)}{\epsilon(D^-|D^+ \text{ decays to } K_L^0\pi^+)}. \quad (5.10)$$

Note that the definition of ϵ in equation Eq. 5.9 is the same as the efficiency used in Eq. 5.3. Using these expressions, we find

$$\mathcal{B}(D^+ \to K_L^0\pi^+) = \frac{Y(D^+ \to K_L^0\pi^+)}{Y(D^-)\,\epsilon} \times R \quad (5.11)$$

Using the fact that $\mathcal{B}(D^+ \to K_L^0\pi^+) \ll 1$, we may approximate R as

$$R \approx \frac{\epsilon(D^-|D^+ \text{ does not decay to } K_L^0\pi^+)}{\epsilon(D^-|D^+ \text{ decays to } K_L^0\pi^+)} \quad (5.12)$$

We will calculate the branching fraction from Eq. 5.11 using the approximation of R in Eq. 5.12. Note that the branching fraction calculated in Eq. 5.11 differs from the naive calculation in Eq. 5.3 only by a factor of R, which accounts for the bias in tag D^- reconstruction efficiency between signal ($D^+ \to K_L^0\pi^+$) and non-signal D^+ decays. R is the ratio of tag reconstruction efficiencies in the cases where D^+ does or does not decay to $K_L^0\pi^+$. This ratio is close to one, but is up to a few percent less since the relatively clean signal decay $D^+ \to K_L^0\pi^+$ will not interfere with the D^- reconstruction as much as a generic D^+ decay will.

The determination of a branching fraction requires the determination of two yields (tag D^- and signal $K_L^0\pi^+$) and three efficiencies (signal and two tag efficiencies). Yields and efficiencies are determined for each tag mode individually, and a branching fraction is calculated from each mode. The values from each of the modes are averaged for the final result.

Table 5.3: D^- yields in generic Monte Carlo.

Tag mode	D^- yield
$D^- \to K^+\pi^-\pi^-$	425658 ± 769
$D^- \to K^+\pi^-\pi^-\pi^0$	159602 ± 700
$D^- \to K^0_S\pi^-$	56329 ± 274
$D^- \to K^0_S\pi^-\pi^0$	113044 ± 599
$D^- \to K^0_S\pi^-\pi^-\pi^+$	105004 ± 570
$D^- \to K^+K^-\pi^-$	59096 ± 333
Sum	918733 ± 1397

5.5 Tag D^- Yield

The D^- yield is obtained by fitting the beam constrained mass of D^- candidates. The signal peak at the D^- mass is fit with the sum of a Gaussian and a Crystal Ball peak with a high-side tail, and the background is fit with an ARGUS function [21]. The yield is taken as the number of events within the $M_{\rm BC}$ range in Table 5.2; the peak function is integrated over this region to determine the number of events inside. Figure 5.2 shows the fits in generic Monte Carlo for each tag mode, and Figure 5.3 shows the fits in data. The yields are shown in Tables 5.3 (Monte Carlo) and 5.4 (data). In total, we find about 165000 tags in data, and the generic Monte Carlo sample is about 5.5 times larger.

5.6 Signal Detection Efficiency

We need efficiencies for reconstructing $D^+ \to K^0_L\pi^+$, given that the D^- was found, in each tag mode. We use signal Monte Carlo in which the D^+ decays to $K^0_L\pi^+$ and the D^- decays to one of the tag modes. The procedure for determining the

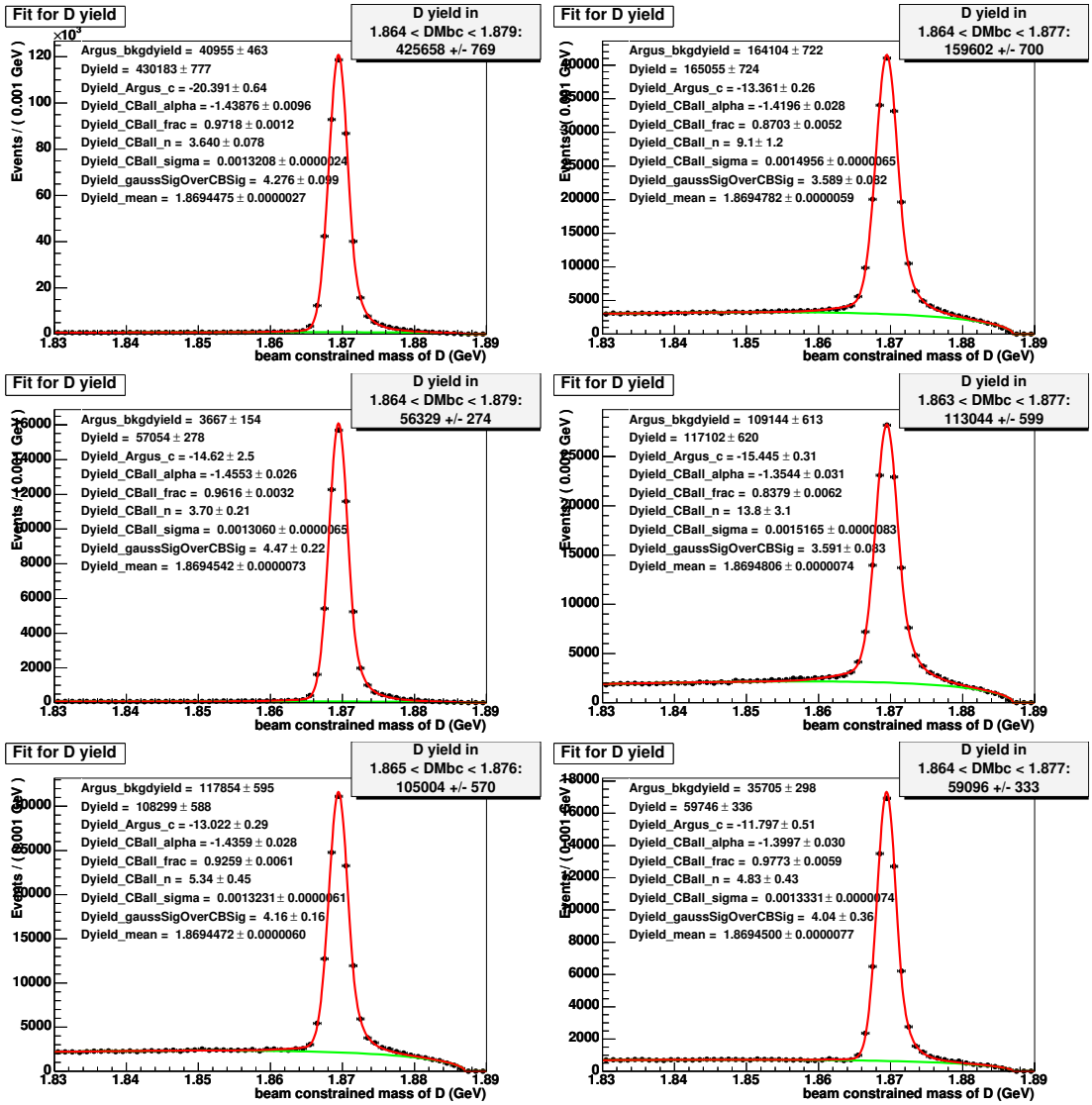

Figure 5.2: Fits for the D^- yield in generic Monte Carlo. From top left, the decay modes are: $D^- \to K^+\pi^-\pi^-$, $D^- \to K^+\pi^-\pi^-\pi^0$, $D^- \to K^0_S\pi^-$, $D^- \to K^0_S\pi^-\pi^0$, $D^- \to K^0_S\pi^-\pi^-\pi^+$, $D^- \to K^+K^-\pi^-$.

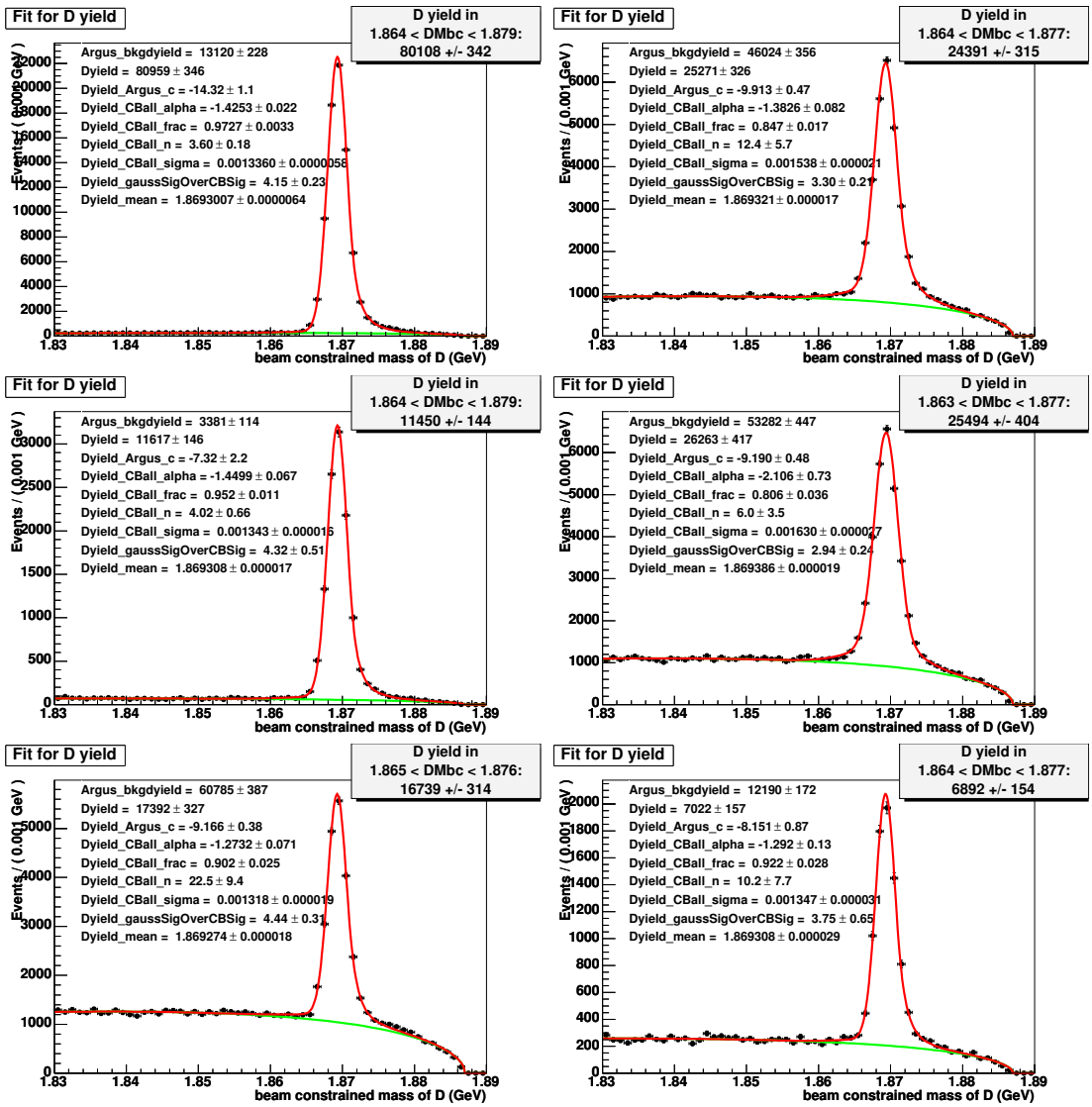

Figure 5.3: Fits for the D^- yield in data. From top left, the decay modes are: $D^- \to K^+\pi^-\pi^-$, $D^- \to K^+\pi^-\pi^-\pi^0$, $D^- \to K^0_S\pi^-$, $D^- \to K^0_S\pi^-\pi^0$, $D^- \to K^0_S\pi^-\pi^-\pi^+$, $D^- \to K^+K^-\pi^-$.

Table 5.4: D^- yields in data.

Tag mode	D^+ yield
$D^- \to K^+\pi^-\pi^-$	80108 ± 342
$D^- \to K^+\pi^-\pi^-\pi^0$	24391 ± 315
$D^- \to K^0_S\pi^-$	11450 ± 144
$D^- \to K^0_S\pi^-\pi^0$	25494 ± 404
$D^- \to K^0_S\pi^-\pi^-\pi^+$	16739 ± 314
$D^- \to K^+K^-\pi^-$	6892 ± 154
Sum	165074 ± 723

efficiency is as follows. We plot the beam constrained mass of the D^- candidates and fit for the yield in the peak using the procedure described in the previous section. We then plot the missing mass squared distribution. This distribution contains a signal peak at the K^0 mass squared and a very small background from fake tag D^- candidates.

The shape of the small background is determined from a fit to events in the $M_{\rm BC}$ sideband ($1.83 < M_{\rm BC} < 1.85$ GeV); the fit function is a second-order polynomial. (See Section 5.8 for more on the fake tag background.) The peak shape is fit with a two-sided Crystal Ball shape. The efficiency is just the yield in the signal peak divided by the D^- yield.

Figure 5.4 shows these fits for the tag mode $D^- \to K^+\pi^-\pi^-$. Table 5.5 lists signal Monte Carlo yields and efficiencies in all tag modes. (See Appendix A.1 for the equation used to calculate the uncertainties in the efficiencies.) Also shown in the table is the fraction of events removed by the veto on extra tracks and π^0s; it is calculated from the $K^0_L\pi^+$ yields before and after application of the veto. The veto rate varies slightly by tag mode. For instance, a charged kaon in the tag may decay inside the detector, so the extra π^0 veto removes more events

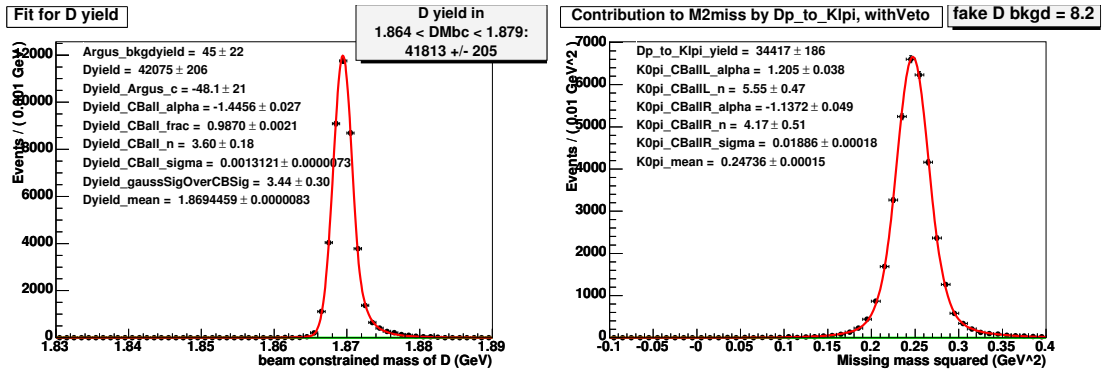

Figure 5.4: Fits used to determine the efficiency for $D^+ \to K^0_L\pi^+$, with tag mode $D^- \to K^+\pi^-\pi^-$. The left plot shows the $M_{\rm BC}$ distribution, and the right plot shows the $M^2_{\rm miss}$ distribution. Plots for efficiencies in other tag modes are similar.

Table 5.5: Yields and $D^+ \to K^0_L\pi^+$ efficiencies from Monte Carlo simulations in different tag modes. The last column shows the fraction of events that were removed by applying a veto on extra tracks or π^0s.

Tag mode	D^- yield	$K^0_L\pi^+$ yield	Efficiency (%)	Veto %
$D^- \to K^+\pi^-\pi^-$	41813 ± 205	34417 ± 186	82.31 ± 0.19	3.55 ± 0.10
$D^- \to K^+\pi^-\pi^-\pi^0$	21453 ± 148	17494 ± 132	81.55 ± 0.27	4.02 ± 0.15
$D^- \to K^0_S\pi^-$	34315 ± 186	28266 ± 168	82.37 ± 0.21	3.44 ± 0.11
$D^- \to K^0_S\pi^-\pi^0$	18019 ± 143	14765 ± 122	81.94 ± 0.37	3.62 ± 0.15
$D^- \to K^0_S\pi^-\pi^-\pi^+$	24857 ± 157	20216 ± 142	81.33 ± 0.24	4.33 ± 0.14
$D^- \to K^+K^-\pi^-$	35154 ± 187	28508 ± 169	81.09 ± 0.21	4.71 ± 0.13

from these tag modes, especially $D^- \to K^+K^-\pi^-$.

We can also use this procedure, with a different fit shape, to measure the efficiency for any other decay mode. These efficiencies are used to fix the yields of backgrounds in the missing mass squared fit, as discussed in Section 5.8.

To determine whether the efficiency is different for oppositely charged Ds, we also determine the efficiencies separately with all the charges conjugated in

Table 5.6: D^- reconstruction efficiencies (%) and ratios in signal Monte Carlo. The first three columns of numbers show the tag reconstruction efficiencies, given that the signal side decayed to $K^0_S\pi^+$, $K^0_L\pi^+$, or anything else. The last column is the branching-fraction-weighted average of $K^0_S\pi^+$ and non-$K^0_{S,L}\pi^+$ divided by $K^0_L\pi^+$.

Tag mode	$D^+ \to K^0_S\pi^+$	$D^+ \to K^0_L\pi^+$	$D^+ \to$ other	R
$D^- \to K^+\pi^-\pi^-$	54.95 ± 0.18	55.75 ± 0.18	55.48 ± 0.18	0.9949 ± 0.0032
$D^- \to K^+\pi^-\pi^-\pi^0$	27.95 ± 0.16	28.60 ± 0.17	27.39 ± 0.16	0.9579 ± 0.0055
$D^- \to K^0_S\pi^-$	45.28 ± 0.18	45.75 ± 0.18	45.33 ± 0.18	0.9908 ± 0.0039
$D^- \to K^0_S\pi^-\pi^0$	23.77 ± 0.16	24.03 ± 0.16	22.97 ± 0.15	0.9565 ± 0.0062
$D^- \to K^0_S\pi^-\pi^-\pi^+$	32.52 ± 0.17	33.14 ± 0.17	31.64 ± 0.17	0.9552 ± 0.0050
$D^- \to K^+K^-\pi^-$	46.78 ± 0.18	46.87 ± 0.18	46.25 ± 0.18	0.9870 ± 0.0038

both the Monte Carlo and the analysis. The results are described in Appendix A.2. The difference between D^+ and D^- is included as a systematic uncertainty, as discussed in Section 5.10.

5.7 Tag Reconstruction Efficiency Ratio

To calculate the tag reconstruction efficiency ratio R (Eq. 5.12), we generate three separate Monte Carlo samples for each tag mode. In all three, the D^- decays to a given tag mode. The samples differ in what the D^+ decays to: either $K^0_S\pi^+$, $K^0_L\pi^+$, or anything else. The tag reconstruction efficiency is found by fitting $M_{\rm BC}$ for the D^- yield just as in any other sample. Dividing by the number of events generated gives the efficiency. Then the ratio R is the non-signal efficiency divided by the signal efficiency. The non-signal efficiency is the branching-fraction-weighted average of the efficiencies for the $K^0_S\pi^+$ and non-$K^0_{S,L}\pi^+$ samples. Table 5.6 shows the efficiencies and ratio for each tag mode.

We find that the efficiencies are highest in $K^0_L\pi^+$ events, somewhat lower in $K^0_S\pi^+$ events, and lowest in non-$K^0_{S,L}\pi^+$ events. The reason for this is that the signal decays are relatively clean compared to generic D^+ decays. This makes it easier to reconstruct the tag.

If we ignored the difference between signal and non-signal efficiencies (*i.e.*, assumed $R = 1$), the measured branching fraction would be off by up to 5% for some tag modes.

5.8 Signal Yields from $M^2_{\rm miss}$ Fit

The signal yields are obtained by fitting the missing mass squared of combinations of D^- and π^+ candidates. These fits are shown in Figures 5.12-5.15.

The fits consist of many components – there are a number of peaking and non-peaking backgrounds. Each background shape is determined from a Monte Carlo simulation of that background.

- The $D^+ \to K^0_L\pi^+$ signal is a peak at the K^0 mass squared. It is fit with the same two-sided Crystal Ball function used in signal Monte Carlo. The parameter values are fixed to those determined in signal Monte Carlo, but the overall width is allowed to vary in the fit to reflect the possible change in resolution between data and Monte Carlo.
- A background peak from $D^+ \to \eta\pi^+$ sits on the right side of the signal peak, centered at the η mass squared. This peak partly overlaps the signal peak. Like the signal peak, it is fit with a two-sided Crystal Ball function, with the shape determined from Monte Carlo. Its width floats with the width

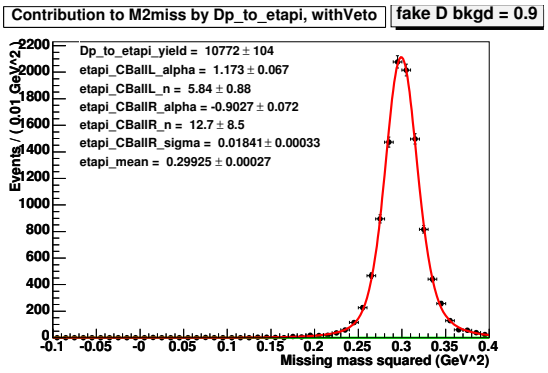

Figure 5.5: Fit to Monte Carlo simulation of the background $D^+ \to \eta\pi^+$. The tag mode is $D^- \to K^+\pi^-\pi^-$.

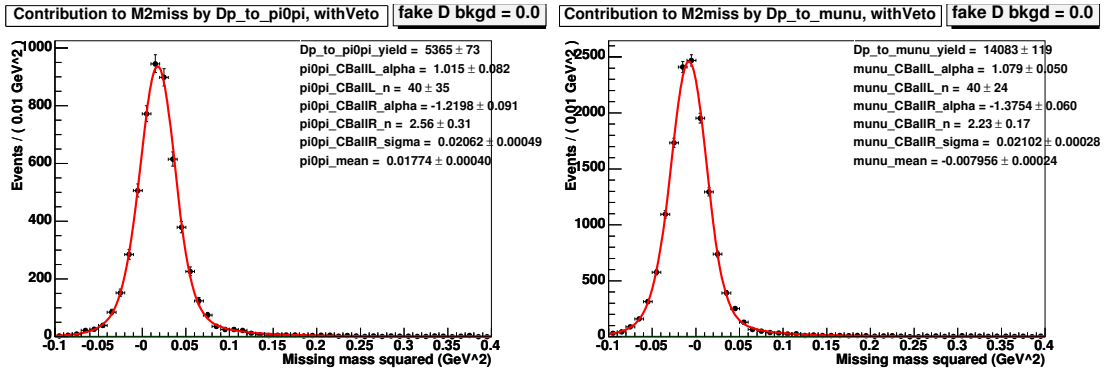

Figure 5.6: Fits to Monte Carlo simulations of the backgrounds $D^+ \to \pi^0\pi^+$ (left) and $D^+ \to \mu^+\nu_\mu$ (right). The tag mode is $D^- \to K^+\pi^-\pi^-$.

of the signal peak (that is, the ratio of the two peak widths is fixed), and the yield is also allowed to float. Figure 5.5 shows the simulation of this background.

- Background peaks from $D^+ \to \pi^0\pi^+$ and $D^+ \to \mu^+\nu_\mu$ are located at and just below the π^0 mass squared. Each one is fit with a two-sided Crystal Ball function. The shapes of these peaks, as well as their relative yields, are determined from Monte Carlo simulations. The total yield of both peaks is allowed to float. Figure 5.6 shows simulations of these backgrounds.

- Many other non-peaking backgrounds are present: $D^+ \to (\tau^+ \to \mu^+ \nu_\mu \bar{\nu}_\tau)\nu_\tau$, $(\tau^+ \to \pi^+ \bar{\nu}_\tau)\nu_\tau$, $\bar{K}^0 K^+$, $\pi^+\pi^0\pi^0\pi^0$, $\pi^+\pi^+\pi^-\pi^0$, $\pi^+\pi^+\pi^-$, $\pi^+\pi^0\pi^0$, $\rho^0\mu^+\nu_\mu$, $K^-\pi^+\pi^+$, $\pi^0\mu^+\nu_\mu$, $\bar{K}^0\mu^+\nu_\mu$, $\bar{K}^0 e^+\nu_e$, $\rho^0 e^+\nu_e$, $\bar{K}^0\pi^+\pi^0$, $K^+\pi^0$, and $(\tau^+ \to \rho^+ \bar{\nu}_\tau)\nu_\tau$. The shapes of these backgrounds are determined from fits to Monte Carlo simulations in which the tag side is always $D^- \to K^+\pi^-\pi^-$. (This tag mode was chosen because it has a very small background.) These fits are shown in Figures 5.7-5.9.

  The K^0_S veto, which removes an event if it contains at least one extra track or π^0, reduces many of these backgrounds, and some are almost totally removed. The veto does not alter the shape of the backgrounds – only their efficiencies. In cases where the number of events remaining after the veto is very small in signal Monte Carlo, the shape is fixed to the shape obtained when no veto is applied.

  Since the backgrounds lie mostly under the signal peak, in the fit for the signal yield it is difficult to accurately determine the background yields. Therefore, we fix their yields Y_i in data and generic Monte Carlo by

$$Y_i = Y_D \mathcal{B}_i \epsilon_i \tag{5.13}$$

  where Y_D is the D yield in data or generic Monte Carlo, $\mathcal{B}_i$ is the branching fraction for this background decay mode, and ϵ_i is the efficiency for this decay to show up in the background. Branching fractions are taken from the Particle Data Group [1]. ϵ_i is determined from a Monte Carlo simulation of decay mode i:

$$\epsilon_i = \frac{\text{\# of events in missing mass squared background}}{D^- \text{yield in this Monte Carlo sample}} \tag{5.14}$$

  Table 5.10 shows the branching fractions used for these backgrounds and the number of events each contributes to the missing mass squared plots

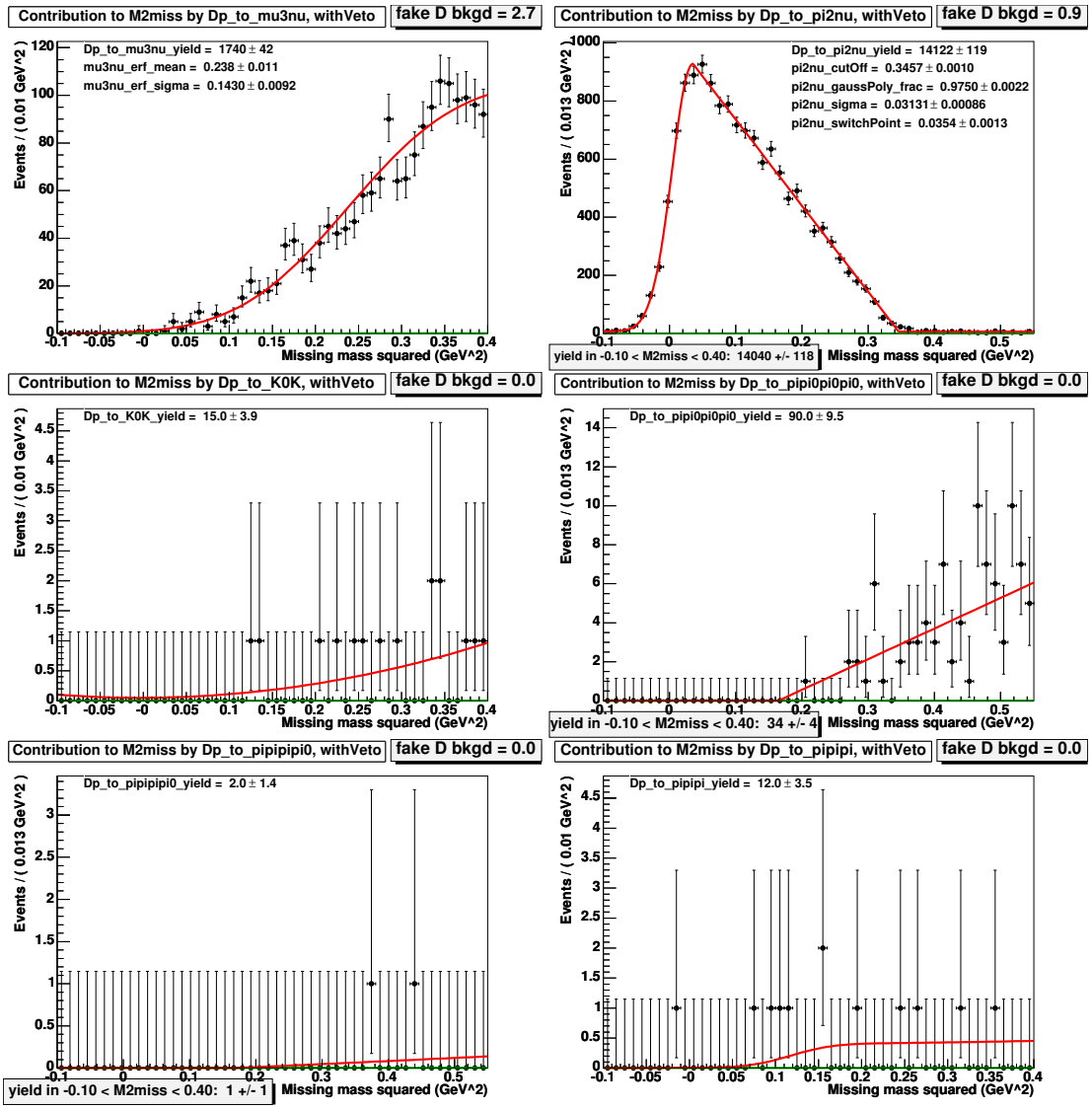

Figure 5.7: Fits to Monte Carlo simulations of the backgrounds (from top left) $D^+ \to (\tau^+ \to \mu^+\nu_\mu\overline{\nu}_\tau)\nu_\tau$, $(\tau^+ \to \pi^+\overline{\nu}_\tau)\nu_\tau$, $\bar{K}^0K^+$, $\pi^+\pi^0\pi^0\pi^0$, $\pi^+\pi^+\pi^-\pi^0$, and $\pi^+\pi^+\pi^-$. The tag mode is $D^- \to K^+\pi^-\pi^-$.

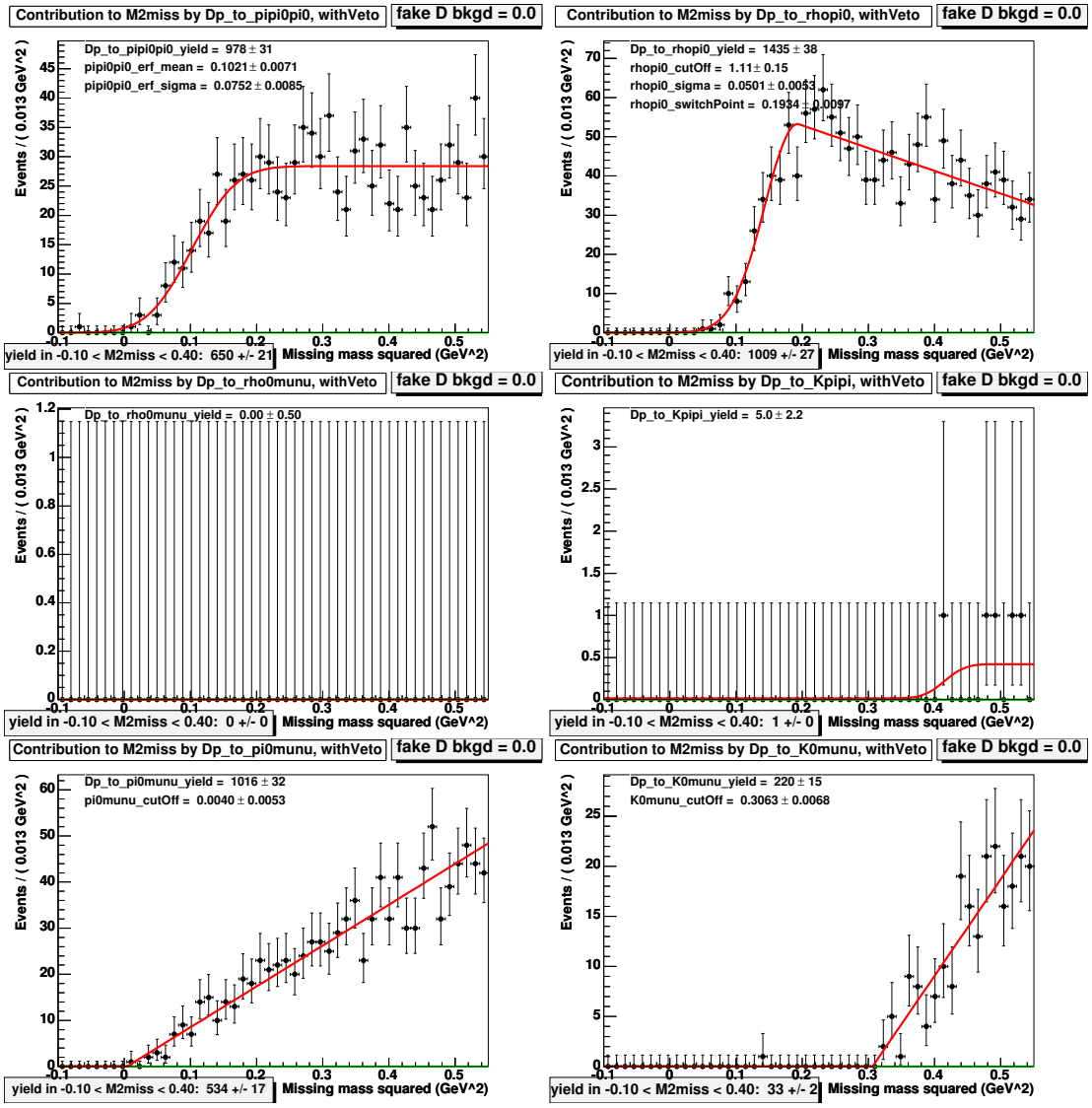

Figure 5.8: Fits to Monte Carlo simulations of the backgrounds (from top left) $D^+ \to \pi^+\pi^0\pi^0$, $\rho^+\pi^0$, $\rho^0\mu^+\nu_\mu$, $K^-\pi^+\pi^+$, $\pi^0\mu^+\nu_\mu$, and $\bar{K}^0\mu^+\nu_\mu$. The tag mode is $D^- \to K^+\pi^-\pi^-$. $D^+ \to \pi^+\pi^0\pi^0$ is simulated with a phase space distribution in generic Monte Carlo. However, we use $D^+ \to \rho^+\pi^0$ for this background when fitting data.

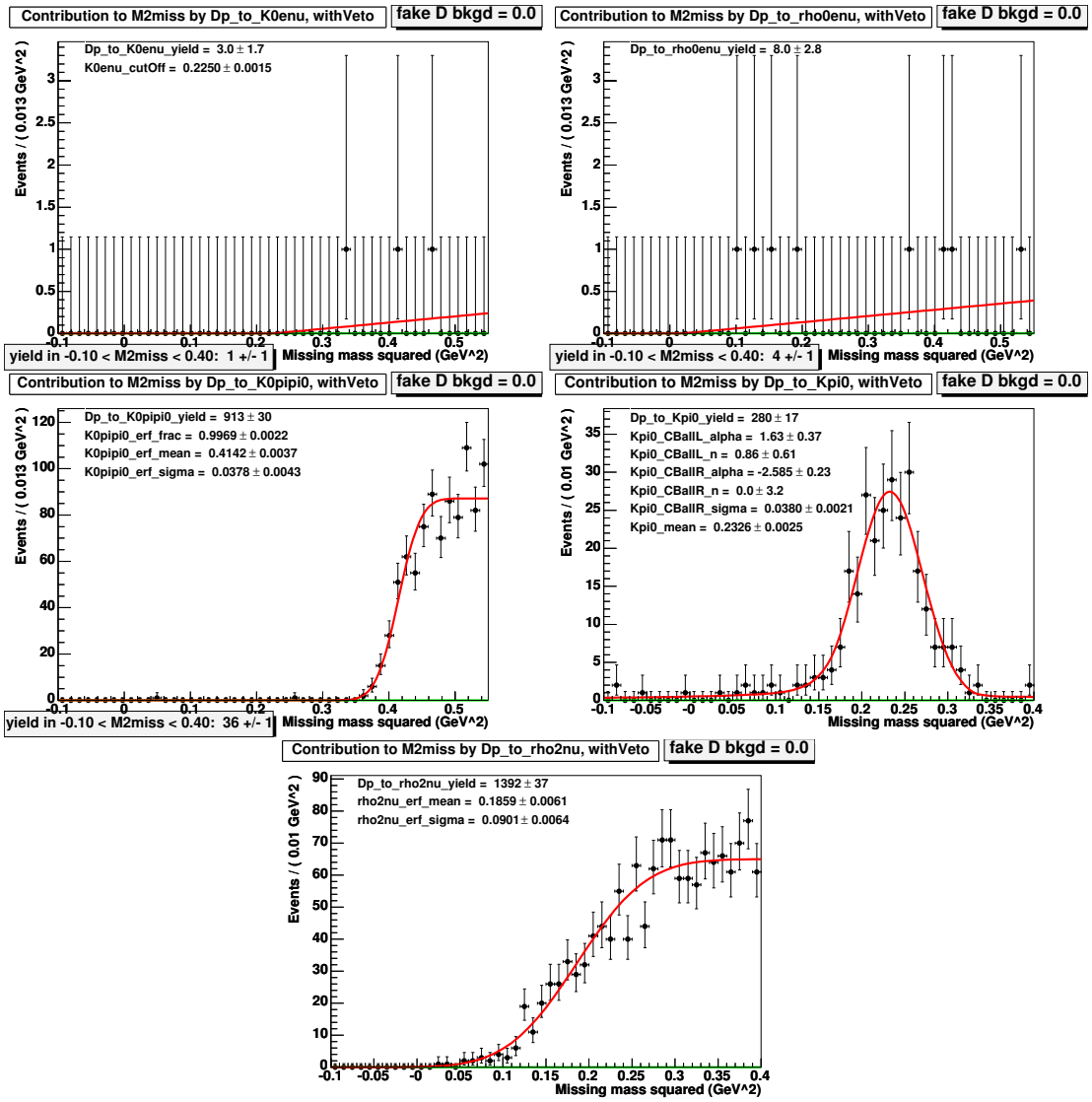

Figure 5.9: Fits to Monte Carlo simulations of the backgrounds $D^+ \to \bar{K}^0 e^+ \nu_e$, $\rho^0 e^+ \nu_e$, $\bar{K}^0 \pi^+ \pi^0$, $K^+ \pi^0$ and $(\tau^+ \to \rho^+ \bar{\nu}_\tau)\nu_\tau$. The tag mode is $D^- \to K^+ \pi^- \pi^-$.

in data.

There is one special case in these backgrounds. $D^+ \to \pi^+\pi^0\pi^0$ is simulated in generic Monte Carlo with a phase-space distribution. However, in reality most $\pi^+\pi^0\pi^0$ events come from $D^+ \to \rho^+\pi^0$. Therefore, in the fits to data, we use the shape and efficiency of $D^+ \to \rho^+\pi^0$ for the $D^+ \to \pi^+\pi^0\pi^0$ background. The $D^+ \to \rho^+\pi^0$ background has a higher efficiency and a somewhat different shape (see Figure 5.8).

- $D^+ \to K^0_S\pi^+$ is included as a background. Its shape is mostly the same as $D^+ \to K^0_L\pi^+$, but there is a small additional component. The K^0_S decays to $\pi^+\pi^-$ about 2/3 of the time, and the π^+ from the K^0_S is combined with the tag D^- to form an entry in the missing mass squared plot. Most of these entries are too large to enter the plot near the signal, but some of them appear as a small background to the right of the signal peak. This background is shown in Figure 5.10. It is, however, greatly reduced by the veto on extra tracks. The total $D^+ \to K^0_S\pi^+$ background is included in the fit as a background, using the same procedure as for the non-peaking backgrounds.

- Fake tag D^- candidates, when combined with π^+ candidates, produce a background in the missing mass squared plot. Most of these fake D^-s produce large $M^2_{\rm miss}$ values; only a small tail extends to the low-$M^2_{\rm miss}$ region near the signal.

  The shape and size of this background are estimated from tag D^- candidates in an $M_{\rm BC}$ sideband, 1.83 GeV $< M_{\rm BC} <$ 1.85 GeV. These are combined with π^+s to form a $M^2_{\rm miss}$ distribution for the fake D^-s in the sideband. However, there is a complication in using the sideband as a model for fake D^-s in the $M_{\rm BC}$ signal region. When calculating $M^2_{\rm miss}$, the $M_{\rm BC}$ of

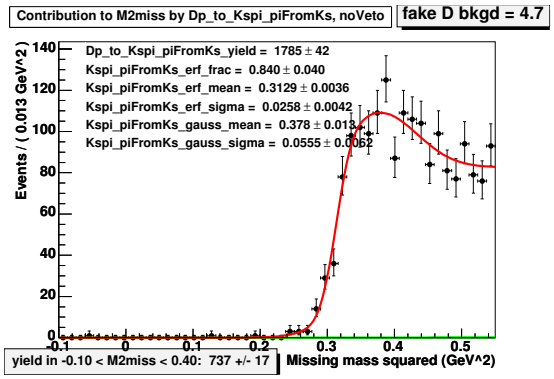

Figure 5.10: Missing mass squared for π^+s that come from the K^0_S in $D^+ \to K^0_S\pi^+$. In this plot the veto on extra tracks and π^0s is not applied because it greatly reduces this background, making it impossible to see the background shape.

the D^- candidate is constrained to the known D^- mass. This constraint essentially shifts the momentum magnitude of the D^- to the expected value without altering its flight direction. When the candidate is a real D^-, this is the correct procedure. However, when comparing fake D^-s in the signal and sideband region of $M_{\rm BC}$, the mass constraint will have different effects. Fake D^-s in the sideband region will have a large shift in momentum, while those in the signal region will see a relatively small shift. This difference is important since the shift in D^- momentum also shifts $M^2_{\rm miss}$, and this shift has a large effect on the number of events near the signal peak in $M^2_{\rm miss}$. As determined by studies of Monte Carlo simulations of non-$D\bar{D}$ and $D^0\bar{D}^0$ events, the efficiency for fake D^-s to show up in the $M^2_{\rm miss}$ plot (that is, below $M^2_{\rm miss} = 0.4$ GeV^2) is lower for candidates in the sideband region than for those in the signal region; the efficiencies differ by a factor of approximately 1.4.

To correct this problem, we define an alternate $M^2_{\rm miss}$ for use with D^- candidates in the sideband region. In this alternate $M^2_{\rm miss}$, the D^- mass is con-

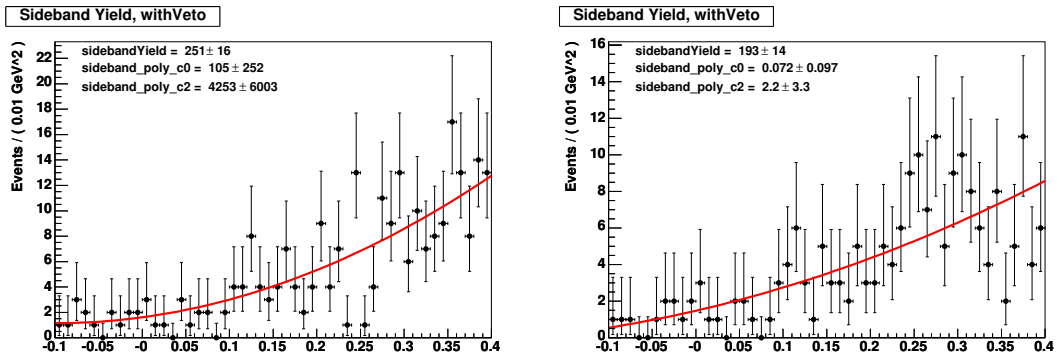

Figure 5.11: Fit for fake D^- background shape and yield in the $M_{\rm BC}$ sideband in generic Monte Carlo (left) and data(right), using all tag modes.

strained to the middle of the sideband, $M_{\rm BC}$ = 1.84 GeV, rather than to the D^- mass. Thus, fake D^-s in the sideband will see their momenta shifted by an amount similar to those in the signal region. The distribution of this alternate $M^2_{\rm miss}$ for sideband D^-s is a good model for the distribution of the normal $M^2_{\rm miss}$ for fake D^-s in the signal region. Repeating the study on simulated non-$D\bar{D}$ and $D^0\bar{D}^0$ events, we find that the sideband and signal efficiencies are the same; their ratio is $C = 1.0 \pm 0.1$. Therefore, we determine the shape and yield of the fake D^- background in $M^2_{\rm miss}$ by the distribution of the alternate $M^2_{\rm miss}$ for events in the $M_{\rm BC}$ sideband.

This background shape is fit with a second-order polynomial. The shape parameters are determined from a fit to sideband events in all tag modes together. Figure 5.11 shows this fit in generic Monte Carlo and in data.

The yield used in the final missing mass squared fit is fixed based on the yield of this sideband shape in the particular tag mode, the yield of the $M_{\rm BC}$ Argus function in the sideband, and the yield of the Argus function

in the signal region:

$$Y_{\text{fake } D\text{s}} = C \times (\text{\# of background events in the } M_{\text{BC}} \text{ signal region}) \times \frac{(\text{\# of } M_{\text{BC}} \text{ sideband events in alternate } M^2_{\text{miss}} \text{ plot})}{(\text{\# of } M_{\text{BC}} \text{ sideband events})} \quad (5.15)$$

Here, $C = 1.0 \pm 0.1$ is the ratio, described above, between signal and sideband efficiencies.

This fake D^- background also appears in signal Monte Carlo, but it is very small. (It is effectively zero for certain tag modes such as $D^- \to K^+\pi^-\pi^-$.) This background is included in signal Monte Carlo fits, using the same procedure.

Figures 5.12 and 5.13 show the missing mass squared fits for generic Monte Carlo. Figures 5.14 and 5.15 show the fits for data. The $D^+ \to K^0_L\pi^+$ signal yields from these fits are used to calculate the branching fraction.

5.9 Results Prior to Systematic Uncertainties and Corrections

Table 5.7 shows the yields and branching fractions in generic Monte Carlo for all 6 tag modes and for all tag modes together. The $D^+ \to K^0_L\pi^+$ branching fraction is calculated using Eq. 5.11. This Monte Carlo was generated with a branching fraction of 1.445 %, so we can compare our results to this number. The last column of the table shows how many standard deviations the calculated value is from the input value. The branching fractions match the input well.

Having verified that the analysis works correctly on generic Monte Carlo, we calculate the $D^+ \to K^0_L\pi^+$ branching fraction in data. Table 5.8 shows the

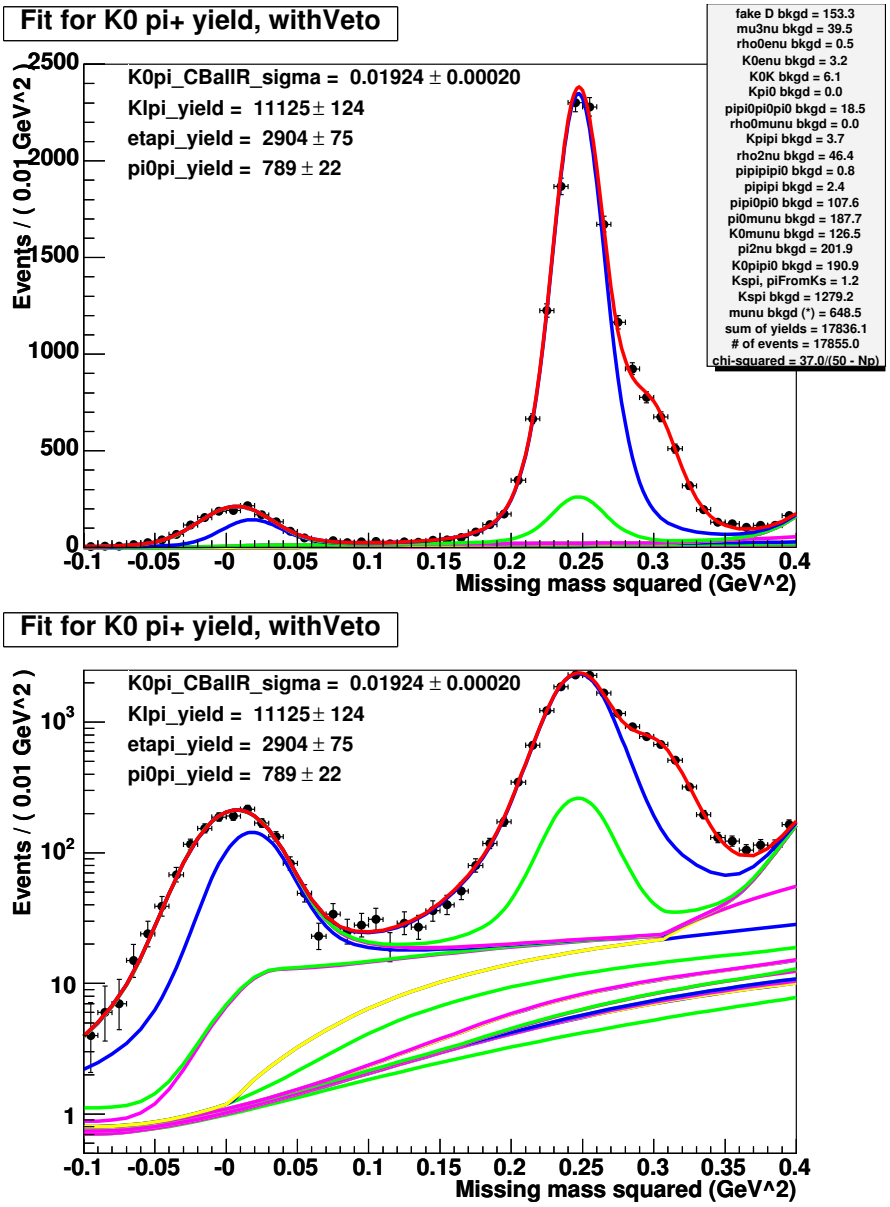

Figure 5.12: Fit for $D^+ \to K^0_L \pi^+$ yield in generic Monte Carlo using all tag modes. The green peak is the contribution of $D^+ \to K^0_S \pi^+$ events that were not vetoed. The top plot has a linear scale, and the bottom plot has a log scale.

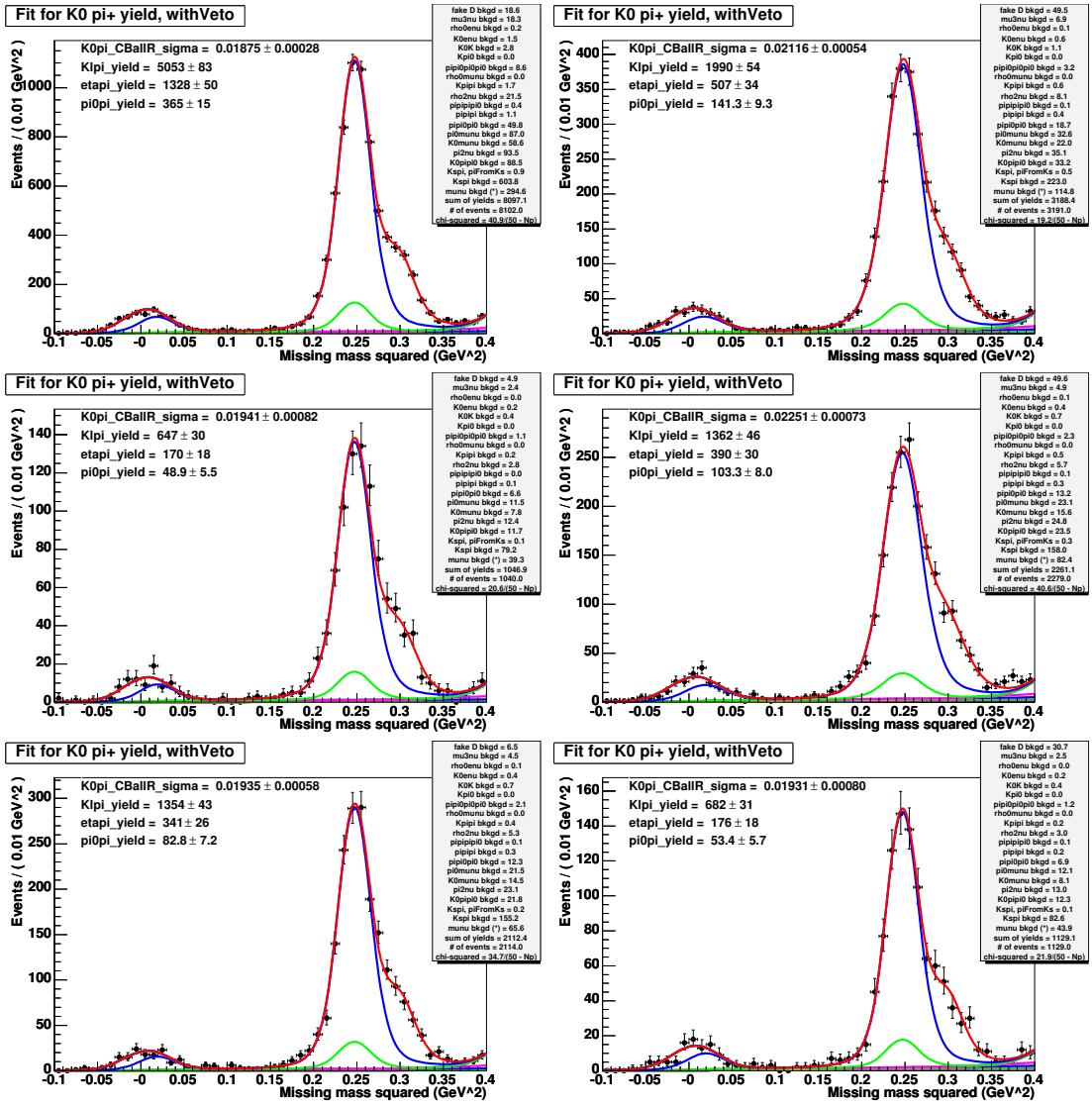

Figure 5.13: Fits for $D^+ \to K^0_L \pi^+$ yield in generic Monte Carlo for each tag mode. The green peak is the contribution of $D^+ \to K^0_S \pi^+$ events that were not vetoed. From top left, the tag modes are: $D^- \to K^+\pi^-\pi^-$, $D^- \to K^+\pi^-\pi^-\pi^0$, $D^- \to K^0_S\pi^-$, $D^- \to K^0_S\pi^-\pi^0$, $D^- \to K^0_S\pi^-\pi^-\pi^+$, and $D^- \to K^+K^-\pi^-$.

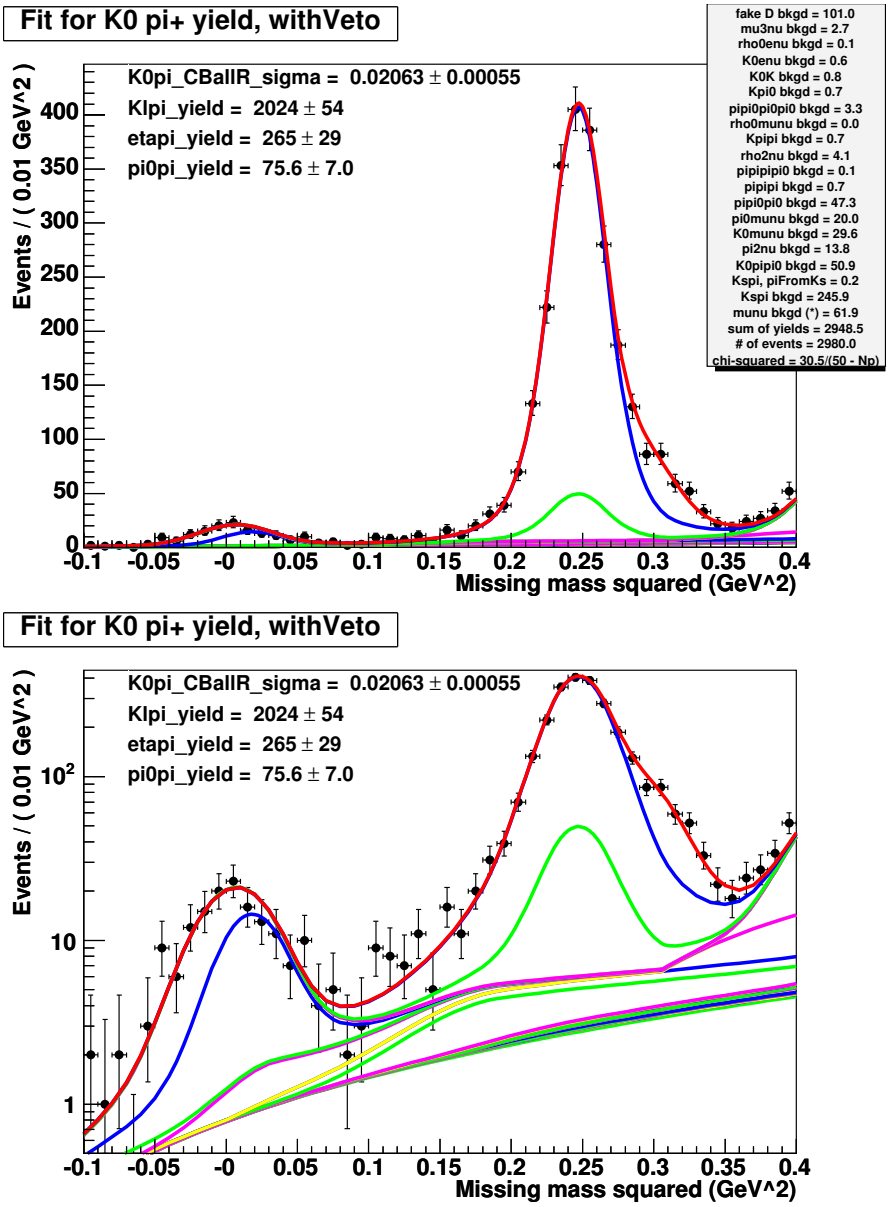

Figure 5.14: Fit for $D^+ \to K^0_L \pi^+$ yield in data using all tag modes. The green peak is the contribution of $D^+ \to K^0_S \pi^+$ events that were not vetoed. The top plot has a linear scale, and the bottom plot has a log scale.

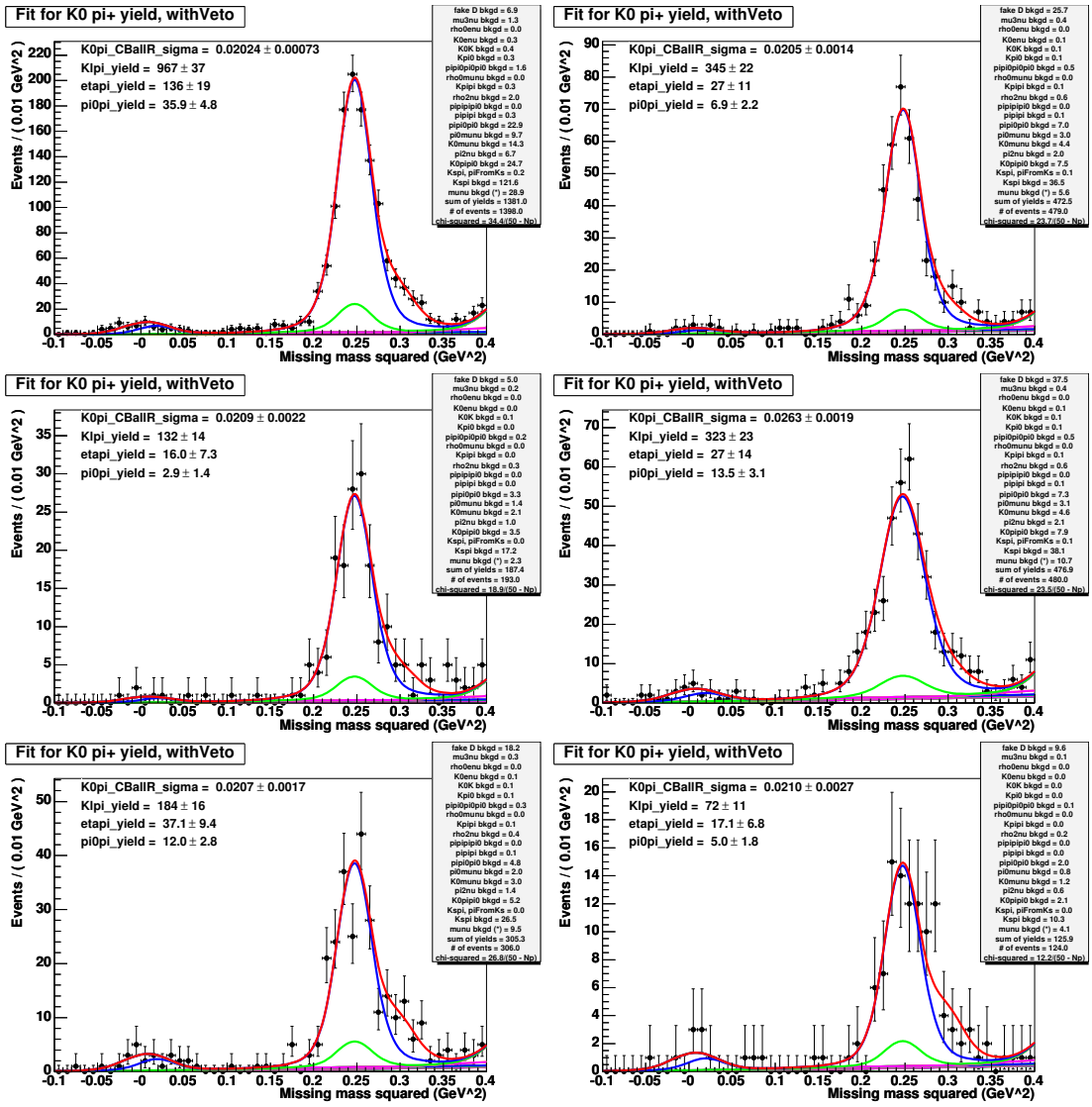

Figure 5.15: Fits for $D^+ \to K^0_L \pi^+$ yield in data for each tag mode. The green peak is the contribution of $D^+ \to K^0_S \pi^+$ events that were not vetoed. From top left, the tag modes are: $D^- \to K^+\pi^-\pi^-$, $D^- \to K^+\pi^-\pi^-\pi^0$, $D^- \to K^0_S\pi^-$, $D^- \to K^0_S\pi^-\pi^0$, $D^- \to K^0_S\pi^-\pi^-\pi^+$, and $D^- \to K^+K^-\pi^-$.

Table 5.7: Measurements of $\mathcal{B}(D^+ \to K^0_L\pi^+)$ from generic Monte Carlo. The branching fraction for each tag mode is calculated from the corresponding yields, efficiency (from Table 5.5), and tag efficiency factor R (from Table 5.6). The last column shows how many standard deviations the result is from the input branching fraction of 1.445 %.

Tag mode	D yield	$D^+ \to K^0_L\pi^+$ yield	Branching fraction (%)	Std. dev. off
$D^- \to K^+\pi^-\pi^-$	425658 ± 769	5053 ± 83	1.435± 0.024	-0.4 σ
$D^- \to K^+\pi^-\pi^-\pi^0$	159602 ± 700	1990 ± 54	1.465± 0.041	+0.5 σ
$D^- \to K^0_S\pi^-$	56329 ± 274	647 ± 30	1.382± 0.064	-1.0 σ
$D^- \to K^0_S\pi^-\pi^0$	113044 ± 599	1362 ± 46	1.406± 0.049	-0.8 σ
$D^- \to K^0_S\pi^-\pi^-\pi^+$	105004 ± 570	1354 ± 43	1.514± 0.049	+1.4 σ
$D^- \to K^+K^-\pi^-$	59096 ± 333	682 ± 31	1.405± 0.064	-0.6 σ
Sum or average	918733 ±1397	11088 ± 125	1.440± 0.017	-0.3 σ

efficiencies, yields, and branching fractions (without systematic uncertainties or corrections) for each mode. The best measurement comes from averaging the results from each tag mode (weighted by the statistical uncertainty). The $D^+ \to K^0_L\pi^+$ branching fraction, before any systematic correction, is measured to be (1.456± 0.040)%, a statistical precision of 2.7%.

5.10 Systematic Uncertainties and Corrections

The systematic uncertainties are listed below and summarized in Table 5.9.

- Pion tracking and particle identification: We must apply efficiency systematics for the π^+ in $D^+ \to K^0_L\pi^+$, but we do not need to correct for the D^- daughters since they appear in both the numerator and denominator of the efficiency. To account for the uncertainty in tracking efficiency, we

Table 5.8: Measurements of $\mathcal{B}(D^+ \to K^0_L\pi^+)$ from data. The branching fraction for each tag mode is calculated from the corresponding yields, efficiency, and tag efficiency factor R (from Table 5.6). This table does not include systematic uncertainties or corrections.

Tag mode	Efficiency (%)	D yield	$D^+ \to K^0_L\pi^+$ yield	Branching fraction (%)
$D^- \to K^+\pi^-\pi^-$	82.31 ± 0.19	80108 ± 342	967 ± 37	1.459± 0.056
$D^- \to K^+\pi^-\pi^-\pi^0$	81.55 ± 0.27	24391 ± 315	345 ± 22	1.662± 0.108
$D^- \to K^0_S\pi^-$	82.37 ± 0.21	11450 ± 144	132 ± 14	1.387± 0.147
$D^- \to K^0_S\pi^-\pi^0$	81.94 ± 0.37	25494 ± 404	323 ± 23	1.479± 0.108
$D^- \to K^0_S\pi^-\pi^-\pi^+$	81.33 ± 0.24	16739 ± 314	184 ± 16	1.291± 0.114
$D^- \to K^+K^-\pi^-$	81.09 ± 0.21	6892 ± 154	72 ± 11	1.271± 0.195
Sum or average	81.80 ± 0.09	165074 ± 723	2023 ± 54	1.456± 0.040

include a systematic uncertainty of 0.3% for the one π^+ track. This uncertainty is consistent with the results in Chapter 4, although it is actually based on an earlier version of the efficiency analysis [22]. Also, we apply a particle identification correction of 0.30 ± 0.25 % for the π^+ track. (The Monte Carlo is 0.3% too efficient, so we multiply the measured branching fractions by 1.003.)

- Tag reconstruction in signal vs. non-signal events: This is the systematic uncertainty in the tag reconstruction efficiency ratio R. We will take the result from an analysis of the same uncertainty in $D^0 \to K^0_L\pi^0$ [6], ± 0.2%. The approach used in that analysis is to study the variation in the tag reconstruction efficiency as the particle multiplicity is reweighted in the Monte Carlo simulation.

- D^+ vs. D^- tags: All of the Monte Carlo samples used to determine efficiencies use D^- as the tag. To evaluate whether the efficiencies are different when D^+ is the tag, we generate Monte Carlo with a tag D^+ and reevaluate

Table 5.9: Systematic uncertainties in the measurement of $\mathcal{B}(D^+ \to K^0_L\pi^+)$. The "signal yields" systematics are estimated by altering the $M^2_{\rm miss}$ fit of all tag modes together. Only the larger of the two "peak shape" systematics is included, as discussed in the text. The $D^+ \to K^0_S\pi^+$ background is not included in the "background yields" systematic; it is separated into the portion due to efficiency and statistical uncertainties and the portion due to the input branching fraction uncertainty.

Efficiencies	
Pion tracking	± 0.3%
Pion particle identification	0.30 ± 0.25%
Tag reconstruction: signal vs. non-signal	± 0.2%
D^+ vs D^- tags	± 0.5%
K^0_S veto systematics	± 1.1%
Signal yields	
$D^+ \to K^0_L\pi^+$ peak shape	± 0.35%
$D^+ \to \eta\pi^+$ peak shape	± 0.69%
Fake D^- background shape	± 0.15%
Fake D^- background yield	± 0.35%
Background yields	± 0.49%
$D^+ \to K^0_S\pi^+$ efficiency & statistics	± 0.80%
Fixed vs. floating peak width	± 1.63%
Tail of signal peak	± 0.25%
Total	± 2.42%
$D^+ \to K^0_S\pi^+$ branching fraction	± 0.33%

the efficiencies. The results are shown in Appendix A.2.

Averaged over all tag modes, the tag and charged pion reconstruction efficiencies agree to within 0.5% between D^+ and D^- tags. We take ±0.5% as the (conservative) value of this systematic uncertainty.

- K^0_S veto systematics: Appendix A.3 derives a formula (equation A.24) for the systematic uncertainties on $\mathcal{B}(D^+ \to K^0_L\pi^+) \equiv B_L$ associated with the K^0_S veto:

$$\frac{\delta B_{L,v}}{B_L} \approx \delta p_{fake} \oplus \frac{1}{6}\frac{\delta\epsilon_{\pi^0}}{\epsilon_{\pi^0}} \oplus \frac{2}{15}\frac{\delta\epsilon_{\pi^+}}{\epsilon_{\pi^+}} \tag{5.16}$$

where $\oplus$ denotes addition in quadrature and the variables are explained below.

δp_{fake} is the systematic uncertainty on the fraction of events in which a fake extra track or π^0 will be found. We evaluate this uncertainty by looking for extra tracks or π^0s in events in which both D and $\bar{D}$ were fully reconstructed. We use both $D^0\bar{D}^0$ and D^+D^- pairs. Suitable $D\bar{D}$ candidates are selected with requirements on the $M_{\rm BC}$ of the two candidates, and $M_{\rm BC}$ sidebands are used to subtract the contribution of fake $D\bar{D}$ candidates. For each $D\bar{D}$ candidate, we ask whether an extra track or π^0 is present and tabulate how often this occurs in both data and generic Monte Carlo. This calculation includes the subtraction of $M_{\rm BC}$ sidebands. Combining the results for all D and $\bar{D}$ decay modes, we find an extra track 0.83 ± 0.07 % of the time in data and 0.74 ± 0.03 % of the time in generic Monte Carlo, a difference of 0.10 ± 0.08 %. We find an extra π^0 1.50 ± 0.09 % of the time in data and 1.18 ± 0.03 % of the time in generic MC, a difference of 0.31 ± 0.10 %. Combining these results and being slightly conservative, we use a systematic of δp_{fake} = 0.5%.

The next term, $(1/6)(\delta\epsilon_{\pi^0}/\epsilon_{\pi^0})$, accounts for the reconstruction efficiency of the π^0s from $K^0_S \to \pi^0\pi^0$. $\delta\epsilon_{\pi^0}/\epsilon_{\pi^0}$ is the π^0 reconstruction systematic uncertainty. It has been measured to be 4 ± 2% for low-momentum π^0s [22]. Our requirements are tighter than the standard π^0 selection since we require both shower energies to be larger than 80 MeV. In principle, this means that the study using standard requirements is not directly applicable; however, the tighter requirement is more likely to improve data-Monte Carlo agreement than to worsen it. We use a π^0 efficiency systematic of 0 ± 6%, which leads to a 1% systematic on $\mathcal{B}(D^+ \to K^0_L\pi^+)$.

The final term, $(2/15)(\delta\epsilon_{\pi^+}/\epsilon_{\pi^+})$, accounts for the reconstruction efficiency of the π^+ and π^- from $K^0_S \to \pi^+\pi^-$. $\delta\epsilon_{\pi^+}/\epsilon_{\pi^+}$ is the π^+ tracking systematic uncertainty, which we again take to be ±0.3%. It is multiplied by the small factor of 2/15, so this uncertainty is negligible.

Combining these uncertainties in quadrature, we obtain a veto systematic of ± 1.1%.

The following systematics are estimated by altering the $M^2_{\rm miss}$ fit in some way – for instance, by raising a background yield by one standard deviation. In all of these cases, the $M^2_{\rm miss}$ distribution in data for all tag modes together is fit with and without the alteration, and the resulting change in the signal yield determines the magnitude of the systematic. Because each tag mode responds to a given alteration in the same way, we do not perform these variations on indivdual tag modes.

- Peak shape: If the Monte Carlo does not accurately simulate the peak shapes, the yields could be biased. In fact, the yields are very sensitive to the peak shapes since the $D^+ \to K^0_L\pi^+$ and $D^+ \to \eta\pi^+$ peaks overlap. To estimate this uncertainty, the fit was redone using the peak shape from each of the different tag modes. The largest of the (six) deviations obtained using the (six) different tag modes was taken as the value of this systematic. This was done for both the $D^+ \to K^0_L\pi^+$ and the $D^+ \to \eta\pi^+$ peaks.

  The peak shape parameters are a width and two parameters for each of the Crystal Ball tails. The tail parameters are similar in all tag modes. The width is the main difference between tag modes – it is wider for modes with a π^0. Since the width floats in the final $M^2_{\rm miss}$ fit, what we are varying

here is essentially the ratio between the $K^0_L\pi^+$ and $\eta\pi^+$ peak widths. Thus, the $K^0_L\pi^+$ and $\eta\pi^+$ peak shape systematics are, to a large extent, measuring the same thing, and so we include only the larger of the two as a systematic uncertainty.

- Fake tag D^- background shape: The fake tag D^- background shape is determined by a $M^2_{\rm miss}$ fit to events in the $M_{\rm BC}$ sideband. Fixing the shape parameters at different (but still reasonable) values produces a change in the signal yield. Here, the alternate shape parameters that we used were the values from the fit in generic Monte Carlo.

- Fake tag D^- background yield: The number of fake D^-s appearing in the missing mass squared plot is uncertain due to statistical fluctuations in this yield and due to the uncertainty in the "correction factor" $C = 1.0 \pm 0.1$. We vary this yield by one standard deviation and take the resulting change in the signal yield as the systematic uncertainty.

- Background yields: The many backgrounds from non-signal D^+ decays introduce a number of systematic uncertainties.

  First, the background efficiencies are not precisely known. We use the statistical uncertainty in the Monte Carlo samples as the uncertainty in the efficiencies.

  More importantly, we must know the branching fractions of these background modes in order to fix their yields. These values, and their uncertainties, are taken from the Particle Data Group [1]. In one case, $D^+ \to \pi^+\pi^0\pi^0\pi^0$, no branching fraction is available. For this mode, the branching fraction is assumed to be $1 \pm 1\%$.

  The final source of uncertainty in the background yields is the possibility

of statistical fluctuations from the value used in the fit. For each background, this uncertainty is the square root of the yield.

Each background yield, one by one, is varied by one standard deviation, and the resulting change in the signal yield is taken as a systematic uncertainty.

The $D^+ \to K^0_S \pi^+$ background is treated like the other backgrounds, except that the uncertainty on $\mathcal{B}(D^+ \to K^0_S \pi^+)$ is kept separate from the other background uncertainties so that its contribution may be quoted separately.

Table 5.10 shows the backgrounds whose yields are fixed in the fit along with their branching fractions, yields, and systematic uncertainties.

- Fixed vs. floating peak width: We find that the value of the signal peak width from the Monte Carlo simulation differs from the fitted width in data by more than one standard deviation. As a systematic variation, we refit the $M^2_{\rm miss}$ distribution with the peak width fixed to the Monte Carlo value. The shift in the peak yield is taken as the value of this systematic, with a small correction: The uncertainty in the signal yield reported by the default fit includes some component due to the uncertainty in the floating peak width. We do not want to double-count this component. Therefore, the value of this systematic is given by

$$\begin{aligned} (\text{systematic})^2 \;=\; & (\text{shift in peak yield})^2 \\ & -[(\text{peak yield uncertainty with floating width})^2 \\ & -(\text{peak yield uncertainty with fixed width})^2] \end{aligned} \quad (5.17)$$

- Tail of signal peak: The tails of the $M^2_{\rm miss}$ peak shapes, which arise primarily from poorly reconstructed π^+s, may not be modeled correctly in

Table 5.10: Fixed backgrounds. For each background, the table lists the branching fraction, sum of background yields in all tag modes, and the systematic uncertainty it produces in the $K^0_L\pi^+$ yield. Branching fraction uncertainties in the smallest one or two significant figures are shown in parentheses. The total systematic (9.9) is divided by the signal yield (2023) to obtain the "Background yields" systematic of 0.49% in Table 5.9.

Background	Branching fraction (%)	Events in data	Resulting $K^0_L\pi^+$ yield uncertainty
$\bar{K}^0 e^+\nu_e$	7.20(80)	0.6	0
$\bar{K}^0 K^+$	0.57(5)	0.8	0.5
$\bar{K}^0\mu^+\nu_\mu$	9.10(90)	29.6	1
$\bar{K}^0\pi^+\pi^0$	14.40(61)	50.9	2
$K^+\pi^0$	0.025(7)	0.7	1
$K^-\pi^+\pi^+$	9.11(20)	0.7	0.5
$\mu^+\nu_\mu\bar{\nu}_\tau\nu_\tau$	0.016(6)	2.7	1
$\pi^0\mu^+\nu_\mu$	0.38(19)	20.0	6
$\pi^+\bar{\nu}_\tau\nu_\tau$	0.010(4)	13.8	4
$\pi^+\pi^0\pi^0$	0.477(46)	47.3	6
$\pi^+\pi^0\pi^0\pi^0$	1(1)	3.3	1
$\pi^+\pi^+\pi^-$	0.335(22)	0.7	0.5
$\pi^+\pi^+\pi^-\pi^0$	1.16(8)	0.1	0
$\rho^0 e^+\nu_e$	0.25(10)	0.1	0
$\rho^0\mu^+\nu_\mu$	0.33(8)	0.0	0
$\rho^+\bar{\nu}_\tau\nu_\tau$	0.030(1)	4.1	1
Total		175.4	9.9
$K^0_S\pi^+$	1.526(44)	245.9	17

Monte Carlo. In fact, we have some evidence from plots in the tracking efficiency analysis that the tails are larger in data than the Monte Carlo predicts. First, we compare the $M^2_{\rm miss}$ distributions in data and Monte Carlo for events where the K^- in $D^0 \to K^-\pi^+$ was found. That is, we form the missing mass of a $\bar{D}^0$ and a π^+, and take only the events where the missing K^- was found. This distribution should be very similar to the missing mass of the K^0_L in $D^+ \to K^0_L\pi^+$. We count the number of events in a region to

the left of the peak, $0.08 < M^2_{\rm miss} < 0.17{\rm GeV}^2$, and a region in the center of the peak, $0.22 < M^2_{\rm miss} < 0.27{\rm GeV}^2$. The ratio of the tail region to the peak region is 1.38 ± 0.20 times larger in data than in Monte Carlo. We also form similar ratios for the K^- in $D^0 \to K^-\pi^+\pi^0$ and the π^+ in $D^0 \to K^-\pi^+$, finding that the tail in data is 1.77 ± 0.09 and 1.76 ± 0.33 times larger, respectively. Thus, it seems that the Monte Carlo underestimates the tail size by a factor of ~1.5.

Also, returning to the $D^+ \to K^0_L\pi^+$ analysis, we see more events in data in the region to the left of the signal peak than the fit shapes predict. Consider the $M^2_{\rm miss}$ fit for all tag modes (Figure 5.14). In the region $0.10 < M^2_{\rm miss} < 0.15$ GeV^2, there are 40 histogram entries. The area of the fit function in this region is 30.3 events, of which 11.5 come from the tail of the signal peak. If we allow the peak's left-side-tail power parameter to vary in the fit, the left-side tail increases so that the area of the fit function in this region is 38.7 events, of which 20.0 come from the tail of the signal peak. The signal yield increases by a small amount, and this increase is taken as a systematic uncertainty.

5.11 Final Results and Conclusion

The final result for the branching fraction $\mathcal{B}(D^+ \to K^0_L\pi^+)$, with systematics, is $\mathcal{B}(D^+ \to K^0_L\pi^+) = (1.460 \pm 0.040 \pm 0.035 \pm 0.005)\%$ [6]. The final uncertainty is the systematic due to the input value of $\mathcal{B}(D^+ \to K^0_S\pi^+)$.

$\mathcal{B}(D^+ \to K^0_L\pi^+)$ can be compared to the value of $\mathcal{B}(D^+ \to K^0_S\pi^+) = (1.526 \pm$

$0.022 \pm 0.038)\%$[1] from a separate CLEO-c analysis [22]. Using these two measurements (and remembering to account for the correlation between them), the asymmetry between $\mathcal{B}(D^+ \to K^0_S\pi^+)$ and $\mathcal{B}(D^+ \to K^0_L\pi^+)$ is

$$R(D^+) \equiv \frac{\mathcal{B}(D^+ \to K^0_S\pi^+) - \mathcal{B}(D^+ \to K^0_L\pi^+)}{\mathcal{B}(D^+ \to K^0_S\pi^+) + \mathcal{B}(D^+ \to K^0_L\pi^+)} = 0.022 \pm 0.016 \pm 0.018.$$

The statistical uncertainty on $R(D^+)$ due to the $D^+ \to K^0_S\pi^+$ measurement is about half that from $D^+ \to K^0_L\pi^+$. The two measurements make approximately equal contributions to the systematic uncertainty.

As a consistency check, we also performed the analysis without the veto on extra tracks and π^0s. This leaves $D^+ \to K^0_S\pi^+$ events in the signal peak, and so we measure $\mathcal{B}(D^+ \to K^0_S\pi^+) + \mathcal{B}(D^+ \to K^0_L\pi^+)$; here the background term for $D^+ \to K^0_S\pi^+$ is omitted from the fit. We find $\mathcal{B}(D^+ \to K^0_S\pi^+) + \mathcal{B}(D^+ \to K^0_L\pi^+) = (3.104 \pm 0.056 \pm 0.071)\%$. We can also compute the asymmetry from the branching fraction sum and the independent $\mathcal{B}(D^+ \to K^0_S\pi^+)$ measurement:

$$R(D^+) = -0.017 \pm 0.023 \pm 0.033$$

This calculation is consistent with the result above, but with poorer precision.

This analysis finds no measureable difference between $\mathcal{B}(D^+ \to K^0_L\pi^+)$ and $\mathcal{B}(D^+ \to K^0_S\pi^+)$. This is consistent with theoretical expectations, which allow for but do not require a large difference. The measurement $R(D^+) = 0.022 \pm 0.016 \pm 0.018$ rules out scenarios of maximal interference between $K^0\pi^+$ and $\bar{K}^0\pi^+$ amplitudes, which, as discussed in Section 5.1, would be expected to produce an asymmetry with absolute value greater than $2\tan^2\theta_C = 0.109 \pm 0.001$. In fact, Bigi and Yamamoto [18] originally predicted, based far less data than is now

[1] This result includes a K^0_S reconstruction systematic uncertainty of 1.8%. If that systematic is reduced to the updated value of 0.8% from Sec. 4.11.5, the branching fraction becomes $\mathcal{B}(D^+ \to K^0_S\pi^+) = (1.526 \pm 0.022 \pm 0.029)\%$ and the asymmetry becomes $R(D^+) = 0.022 \pm 0.016 \pm 0.016$.

available, an asymmetry of $R(D^+) \approx 2\tan^2\theta_C \times -1.2$; our measurement refutes that value.

Theoretical predictions of $R(D^+)$ are possible under certain assumptions. One analysis [20], based on moderate breaking of SU(3) symmetry, finds $R(D^+) \approx 0.04$, consistent with our measurement. Another [4], based on analysis of topological amplitudes in many D decays, finds $R(D^+) = -0.006^{+0.033}_{-0.028}$, also consistent.

This analysis takes advantage of the clean $D\bar{D}$ environment and well-known initial state at the CLEO-c detector to perform the first measurement of the branching fraction $\mathcal{B}(D^+ \to K^0_L\pi^+)$. This measurement provides useful constraints on the amplitudes for $D^+ \to K^0\pi^+$ and $D^+ \to \bar{K}^0\pi^+$, and together with the result for $\mathcal{B}(D^0 \to K^0_L\pi^0)$ it completes the picture of $D \to K\pi$ decays.

APPENDIX A

SUPPLEMENTARY INFORMATION FOR MEASUREMENT OF $D^+ \to K^0_L \pi^+$

A.1 Calculation of Efficiency and Branching Fraction Uncertainties

The calculation of uncertainties for the efficiencies and branching fractions is complicated by the fact that uncertainties arise from both statistics and fit uncertainties.

Consider the calculation of an efficiency ϵ. We measure E, the number of efficient events, and T, the total number of events (efficient plus inefficient events), from fits to $M^2_{\rm miss}$ and $M_{\rm BC}$ distributions. For each of these numbers, the fit gives an uncertainty which is a combination of two uncertainties:

- the statistical uncertainty ($\sqrt{E}$ or $\sqrt{T}$).
- the uncertainty ($\delta E_{\rm fit}$ or $\delta T_{\rm fit}$) from not knowing what fraction of the events in each fit are part of the peak (which should be included in E or T) and which are part of the background (which should not be included).

The total uncertainties δE and δT reported by the fit can be separated:

$$\begin{aligned} (\delta E)^2 &= E + (\delta E_{\rm fit})^2 \\ (\delta T)^2 &= T + (\delta T_{\rm fit})^2 \end{aligned} \tag{A.1}$$

First, combine the statistical uncertainties in E and T to get the total statistical uncertainty in the efficiency $\epsilon = E/T$:

$$\delta\epsilon_{\rm stat} = \frac{1}{\sqrt{T}}\sqrt{\epsilon(1-\epsilon)} = \epsilon\sqrt{\frac{1}{E} - \frac{1}{T}} \tag{A.2}$$

This is a binomial error.

Second, combine the fit uncertainties, which are uncorrelated, to get the total fit uncertainty:

$$\begin{aligned}\delta\epsilon_{\text{fit}} &= \epsilon\sqrt{(\frac{\delta E_{\text{fit}}}{E})^2 + (\frac{\delta T_{\text{fit}}}{T})^2} \\ &= \epsilon\sqrt{\frac{(\delta E)^2 - E}{E^2} + \frac{(\delta T)^2 - T}{T^2}} \\ &= \epsilon\sqrt{\left(\frac{\delta E}{E}\right)^2 + \left(\frac{\delta T}{T}\right)^2 - \frac{1}{E} - \frac{1}{T}}\end{aligned} \tag{A.3}$$

Combining the statistical and fit uncertainties in quadrature, we find that the total uncertainty in the efficiency is

$$\begin{aligned}\delta\epsilon &= \sqrt{(\delta\epsilon_{\text{stat}})^2 + (\delta\epsilon_{\text{fit}})^2} \\ &= \epsilon\sqrt{\left(\frac{\delta E}{E}\right)^2 + \left(\frac{\delta T}{T}\right)^2 - \frac{2}{T}}\end{aligned} \tag{A.4}$$

Equation A.4 is used to obtain the uncertainties in the efficiencies. Note that it reduces to the statistical uncertainty when $\delta E = \sqrt{E}$ and $\delta T = \sqrt{T}$. Also, $(\frac{\delta E}{E})^2$ and $(\frac{\delta T}{T})^2$ are both greater than $1/T$, so the sum under the square root is positive.

Branching fraction calculations are similar. Using $B = S/(T\epsilon)$ where S is the number of observed signal events, T is the total number of events, and ϵ is the efficiency, we find

$$\delta B = B\sqrt{\left(\frac{\delta S}{S}\right)^2 + \left(\frac{\delta T}{T}\right)^2 - \frac{2}{T} + \left(\frac{\delta\epsilon}{\epsilon}\right)^2} \tag{A.5}$$

The only difference in this calculation is the extra term for ϵ.

A.2 Comparison of D^+ and D^- Tags

In this analysis, we always measure tag and signal efficiencies in Monte Carlo samples where the D^- is the tag. This section presents efficiencies measured

with a D^+ tag. The differences are used to determine a systematic uncertainty.

Table A.1 lists tag efficiency ratios and $D^\pm \to K^0_L\pi^\pm$ reconstruction efficiencies for both D^+ and D^- tags. Note that the numbers for D^- tags are the same as those in Section 5.7. The D^+ numbers are determined in the same way.

Since we use the D^- efficiencies in the analysis, we must include a systematic uncertainty to account for differences in the efficiencies. The appropriate systematic is one half the relative difference between D^+ and D^- tags. Based on the average D^+/D^- ratios in the tables, we apply a conservative systematic of 0.5%.

A.3 Systematic Uncertainty in $\mathcal{B}(D^+ \to K^0_L\pi^+)$ Due to K^0_S Veto

This section derives the systematic uncertainty in $\mathcal{B}(D^+ \to K^0_L\pi^+) \equiv B_L$ due to the extra track and extra π^0 vetoes. This systematic is denoted as $\delta B_{L,v}$. It includes systematics on how often a $D^+ \to K^0_L\pi^+$ event is falsely vetoed and on how often a real track or π^0 is found in a $D^+ \to K^0_S\pi^+$ event.

A.3.1 Notation

Throughout this appendix, we will use the following notation:

- $B_L \equiv \mathcal{B}(D^+ \to K^0_L\pi^+)$
- $B_S \equiv \mathcal{B}(D^+ \to K^0_S\pi^+)$

Table A.1: Tag efficiency ratios R and $D^{\pm} \to K^0_L\pi^{\pm}$ reconstruction efficiencies for D^+ and D^- tags. The D^- numbers are the same as those in Section 5.7.

Tag mode	R	Efficiency (%)
$D^+ \to K^-\pi^+\pi^+$	0.9957 ± 0.0040	81.94 ± 0.23
$D^- \to K^+\pi^-\pi^-$	0.9949 ± 0.0032	82.31 ± 0.19
Ratio (D^+/D^-)	1.0008 ± 0.0052	0.9955 ± 0.0036
$D^+ \to K^-\pi^+\pi^+\pi^0$	0.9538 ± 0.0068	81.55 ± 0.38
$D^- \to K^+\pi^-\pi^-\pi^0$	0.9579 ± 0.0055	81.55 ± 0.27
Ratio (D^+/D^-)	0.9957 ± 0.0091	1.0001 ± 0.0058
$D^+ \to K^0_S\pi^+$	0.9948 ± 0.0049	82.13 ± 0.25
$D^- \to K^0_S\pi^-$	0.9908 ± 0.0039	82.37 ± 0.21
Ratio (D^+/D^-)	1.0040 ± 0.0063	0.9970 ± 0.0040
$D^+ \to K^0_S\pi^+\pi^0$	0.9689 ± 0.0077	81.74 ± 0.43
$D^- \to K^0_S\pi^-\pi^0$	0.9565 ± 0.0062	81.94 ± 0.37
Ratio (D^+/D^-)	1.0130 ± 0.0104	0.9975 ± 0.0069
$D^+ \to K^0_S\pi^+\pi^+\pi^-$	0.9668 ± 0.0062	81.02 ± 0.31
$D^- \to K^0_S\pi^-\pi^-\pi^+$	0.9552 ± 0.0050	81.33 ± 0.24
Ratio (D^+/D^-)	1.0122 ± 0.0083	0.9962 ± 0.0048
$D^+ \to K^-K^+\pi^+$	0.9947 ± 0.0047	81.10 ± 0.25
$D^- \to K^+K^-\pi^-$	0.9870 ± 0.0038	81.09 ± 0.21
Ratio (D^+/D^-)	1.0078 ± 0.0062	1.0001 ± 0.0040
Average for D^+	0.9787 ± 0.0022	81.62 ± 0.12
Average for D^-	0.9728 ± 0.0018	81.80 ± 0.09
Average Ratio (D^+/D^-)	1.0046 ± 0.0028	0.9975 ± 0.0018

- $P \equiv$ number of events in the M^2_{miss} peak at the K^0 mass squared (i.e. $D^+ \to K^0_L\pi^+$ yield plus $D^+ \to K^0_S\pi^+$ yield)
- $N_{\text{tag}} \equiv$ number of tag D^-s
- ϵ_L = efficiency for finding $D^+ \to K^0_L\pi^+$ in the missing mass squared peak, given that the tag D^- was found.
- ϵ_S = efficiency for finding $D^+ \to K^0_S\pi^+$ in the missing mass squared peak, given that the tag D^- was found.

A.3.2 Starting Formulas

The expected peak yield for a given mode is the number of tags times the branching fraction times the efficiency. Thus

$$P = (\epsilon_L B_L + \epsilon_S B_S) N_{\text{tag}} \tag{A.6}$$

Solving for B_L,

$$B_L = (\frac{P}{N_{\text{tag}}} - \epsilon_S B_S) \frac{1}{\epsilon_L} \tag{A.7}$$

We would like to separate the $D^+ \to K_S^0 \pi^+$ events into the cases where $K_S^0 \to \pi^0\pi^0$ and $K_S^0 \to \pi^+\pi^-$.

Therefore we introduce some additional notation:

- $B_{\pi^0\pi^0}$ ≡ branching fraction for $D^+ \to (K_S^0 \to \pi^0\pi^0)\pi^+ = \mathcal{B}(D^+ \to K_S^0\pi^+)\mathcal{B}(K_S^0 \to \pi^0\pi^0)$
- $B_{\pi^+\pi^-}$ ≡ branching fraction for $D^+ \to (K_S^0 \to \pi^+\pi^-)\pi^+ = \mathcal{B}(D^+ \to K_S^0\pi^+)\mathcal{B}(K_S^0 \to \pi^+\pi^-)$
- $\epsilon_{\pi^0\pi^0}$ ≡ efficiency for finding $D^+ \to (K_S^0 \to \pi^0\pi^0)\pi^+$ in the missing mass squared peak, given that the tag D^- was found.
- $\epsilon_{\pi^+\pi^-}$ ≡ efficiency for finding $D^+ \to (K_S^0 \to \pi^+\pi^-)\pi^+$ in the missing mass squared peak, given that the tag D^- was found.
- Define v_i by $\epsilon_i = v_i \epsilon_{NV}$ where $i = L, \pi^0\pi^0, \pi^+\pi^-$. ϵ_{NV} is the efficiency when no veto is applied, which we assume is the same for all three cases, and v_i is the fraction of events of type i that survive the veto. Using the approximate veto percentages in Section 5.3, $v_L \approx 96\%$, $v_{\pi^0\pi^0} \approx 40\%$, and $v_{\pi^+\pi^-} < 1\%$.

Generalizing Eq. A.6,

$$P = (\epsilon_L B_L + \epsilon_{\pi^0\pi^0} B_{\pi^0\pi^0} + \epsilon_{\pi^+\pi^-} B_{\pi^+\pi^-}) N_{\text{tag}} \tag{A.8}$$

Solving for B_L,

$$B_L = (\frac{P}{N_{\text{tag}}} - \epsilon_{\pi^0\pi^0} B_{\pi^0\pi^0} - \epsilon_{\pi^+\pi^-} B_{\pi^+\pi^-}) \frac{1}{\epsilon_L} \tag{A.9}$$

This also follows from Eq. A.7 if we substitute

$$\epsilon_S = \frac{B_{\pi^0\pi^0}}{B_S} \epsilon_{\pi^0\pi^0} + \frac{B_{\pi^+\pi^-}}{B_S} \epsilon_{\pi^+\pi^-} \tag{A.10}$$

Finally, substitute $\epsilon_i = \nu_i \epsilon_{NV}$:

$$B_L = (\frac{P}{N_{\text{tag}} \epsilon_{NV}} - \nu_{\pi^0\pi^0} B_{\pi^0\pi^0} - \nu_{\pi^+\pi^-} B_{\pi^+\pi^-}) \frac{1}{\nu_L} \tag{A.11}$$

A.3.3 Uncertainties Due to Veto Efficiencies

We are interested in the uncertainties in B_L due to the efficiencies ν_L, $\nu_{\pi^0\pi^0}$, and $\nu_{\pi^+\pi^-}$. Propagating uncertainties, we find:

$$\delta B_{L,\nu_L} = -\frac{B_L}{\nu_L} \delta\nu_L \tag{A.12}$$

$$\delta B_{L,\nu_{\pi^0\pi^0}} = -\frac{B_{\pi^0\pi^0}}{\nu_L} \delta\nu_{\pi^0\pi^0} \tag{A.13}$$

$$\delta B_{L,\nu_{\pi^+\pi^-}} = -\frac{B_{\pi^+\pi^-}}{\nu_L} \delta\nu_{\pi^+\pi^-} \tag{A.14}$$

Equivalently,

$$\frac{\delta B_{L,\nu}}{B_L} = \frac{\delta\nu_L}{\nu_L} \oplus \frac{B_{\pi^0\pi^0}}{B_L} \frac{\delta\nu_{\pi^0\pi^0}}{\nu_L} \oplus \frac{B_{\pi^+\pi^-}}{B_L} \frac{\delta\nu_{\pi^+\pi^-}}{\nu_L} \tag{A.15}$$

where $\oplus$ denotes addition in quadrature.

The analysis that follows is specific to the veto used in measuring $\mathcal{B}(D^+ \to K^0_L \pi^+)$. This veto removes any event in which at least one extra track or at least one extra π^0 is found, other than those used for the tag D^- or the π^+.

Evaluation of $\delta\nu_L$

In order to veto a $D^+ \to K_L^0\pi^+$ event, we must find a fake extra track or π^0. Let p_{fake} be the probability that this happens. Then $\nu_L = 1 - p_{fake}$, and

$$\delta\nu_L = -\delta p_{fake} \tag{A.16}$$

Evaluation of $\delta\nu_{\pi^0\pi^0}$

In this section, we will express $\delta\nu_{\pi^0\pi^0}$ as a function of $\delta\epsilon_{\pi^0}$, where ϵ_{π^0} is the efficiency for finding a single π^0.

There are three ways for a $D^+ \to (K_S^0 \to \pi^0\pi^0)\pi^+$ event to get vetoed:

1. The first π^0 is found.
2. The second π^0 is found.
3. Some bogus track or π^0 is found. This happens with probability p_{fake}.

Assuming that these three possibilities are uncorrelated,

$$\nu_{\pi^0\pi^0} = (1 - \epsilon_{\pi^0})(1 - \epsilon_{\pi^0})(1 - p_{fake}) \tag{A.17}$$

Propagating uncertainties in ϵ_{π^0} and p_{fake},

$$\delta\nu_{\pi^0\pi^0} = (1 - p_{fake})2\epsilon_{\pi^0}(1 - \epsilon_{\pi^0})\frac{\delta\epsilon_{\pi^0}}{\epsilon_{\pi^0}} \oplus (1 - \epsilon_{\pi^0})^2\delta p_{fake} \tag{A.18}$$

If we make the approximations $p_{fake} \approx 0\%$ and $\epsilon_{\pi^0} \approx 50\%$,

$$\delta\nu_{\pi^0\pi^0} \approx \frac{1}{2}\frac{\delta\epsilon_{\pi^0}}{\epsilon_{\pi^0}} \oplus \frac{1}{4}\delta p_{fake} \tag{A.19}$$

The factor of $\frac{1}{2}$ on $\frac{\delta\epsilon_{\pi^0}}{\epsilon_{\pi^0}}$ is actually an upper bound. Any nonzero p_{fake} or any $\epsilon_{\pi^0} \neq 50\%$ will produce a factor less than $\frac{1}{2}$.

Evaluation of $\delta\nu_{\pi^+\pi^-}$

In this section, we will express $\delta\nu_{\pi^+\pi^-}$ as a function of p_{bp}, the probability that an individual charged particle goes down the beampipe, and of ϵ_{π^+}, the efficiency for finding a single π^+ given that it did not go down the beampipe.

There are three ways for a $D^+ \to (K^0_S \to \pi^+\pi^-)\pi^+$ event to be vetoed:

1. The π^+ is found.
2. The π^- is found.
3. Some bogus track or π^0 is found. This happens with probability p_{fake}.

There are two ways that a π^+ might not be found:

1. It goes down the beampipe (probability p_{bp}).
2. It doesn't go down the beampipe, but the track finding fails (probability $1 - \epsilon_{\pi^+}$).

Kinematically, it is unlikely that both the π^+ and the π^- go down the beampipe. We will assume that the probability they both do is 0, and that the probability that neither does is $(1 - p_{bp})^2$. Thus, the probability that one does and one does not is $1 - (1 - p_{bp})^2 = 2p_{bp} - p^2_{bp}$. (This is an approximation, but it is sufficient for our purposes since $\delta\nu_{\pi^+\pi^-}$ will turn out to be negligibly small.) When one track is in the tracking volume, the probablity that it will not be found is $1 - \epsilon_{\pi^+}$. When two are in the tracking volume, the probability that neither is found is $(1 - \epsilon_{\pi^+})^2$. Now, we can write an expression for $\nu_{\pi^+\pi^-}$:

$$\nu_{\pi^+\pi^-} = [(2p_{bp} - p^2_{bp})(1 - \epsilon_{\pi^+}) + (1 - p_{bp})^2(1 - \epsilon_{\pi^+})^2](1 - p_{fake}) \tag{A.20}$$

Propagating errors (and assuming $\delta p_{bp} = 0$),

$$\begin{aligned}\delta\nu_{\pi^+\pi^-} &= [(2p_{bp} - p_{bp}^2) + 2(1-p_{bp})^2(1-\epsilon_{\pi^+})](1-p_{fake})\delta\epsilon_{\pi^+} \\ &\oplus[(2p_{bp} - p_{bp}^2)(1-\epsilon_{\pi^+}) + (1-p_{bp})^2(1-\epsilon_{\pi^+})^2]\delta p_{fake} \end{aligned} \quad \text{(A.21)}$$

If we make the approximations $p_{fake} \approx 0\%$ and $\epsilon_{\pi^+} \approx 96\%$, and use $p_{bp} = 0.07$ (since the tracking system covers 93% of the solid angle),

$$\delta\nu_{\pi^+\pi^-} \approx \frac{1}{5}\delta\epsilon_{\pi^+} \oplus \frac{1}{150}\delta p_{fake} \quad \text{(A.22)}$$

A.3.4 Combining Uncertainties

Starting from Eq. A.15, we substitute the uncertainties from Equations A.16, A.19, and A.22. We also make the approximations $B_{\pi^0\pi^0}/B_L = 1/3$, $B_{\pi^+\pi^-}/B_L = 2/3$, and $\nu_L = 1$.

Combining all of these equations,

$$\frac{\delta B_{L,\nu}}{B_L} = \delta p_{fake} \oplus \frac{1}{3}(\frac{1}{2}\frac{\delta\epsilon_{\pi^0}}{\epsilon_{\pi^0}} \oplus \frac{1}{4}\delta p_{fake}) \oplus \frac{2}{3}(\frac{1}{5}\delta\epsilon_{\pi^+} \oplus \frac{1}{150}\delta p_{fake}) \quad \text{(A.23)}$$

Simplifying and rounding,

$$\frac{\delta B_{L,\nu}}{B_L} \approx \delta p_{fake} \oplus \frac{1}{6}\frac{\delta\epsilon_{\pi^0}}{\epsilon_{\pi^0}} \oplus \frac{2}{15}\frac{\delta\epsilon_{\pi^+}}{\epsilon_{\pi^+}} \quad \text{(A.24)}$$

This equation expresses the systematic uncertainty due to the extra track and π^0 vetoes as a function of systematic uncertainties in the track and π^0 fake rate, the π^0 reconstruction efficiency, and the π^+ track reconstruction efficiency.

APPENDIX B

CALIBRATION OF CMS PIXEL DETECTOR READOUT

The CMS (Compact Muon Solenoid) detector [23] is one of the two large general-purpose particle detectors at the Large Hadron Collider. The component of CMS closest to the interaction region is the silicon pixel detector [24, 25]. As the innermost subdetector, it is highly segmented; this segmentation provides low occupancy and excellent position resolution. Precise position measurements are essential to allow for detection of vertices displaced from the interaction point. The pixel detector also provides seeding for track reconstruction.

The pixel detector collects charge from the passage of charged particles through silicon wafers which have been doped and biased. Charge is drawn to pads arrayed in a grid on the surface of the silicon; each pad corresponds to a single pixel. The collected charge is amplified, stored, and read out as a pulse height that is related to the charge (and is proportional for small charges). The pixel size is 150 μm $\times$ 100 μm, but the position resolution is better because hits on adjacent pixels may be interpolated to provide sub-pixel precision.

The pixel detector contains an immense number of channels – 66 million pixels. Reading out this volume of data is a challenge. The first step is to reduce the data volume through sparcification. The occupancy is very low – in a given event only about 0.03% of pixels contain a hit. Therefore, the readout sends only those pixels containing a hit. Pixels are grouped into units, each of which is read out by a dedicated optical link. When the CMS trigger selects an event, for each hit in that event the pixel ID and pulse height is sent over the optical link. The data stream is a combination of digital and analog – pixel IDs are encoded in six discrete address levels, and the pulse height is transmitted as an analog value. Electronics on the receiving end of the optical link decode the address levels

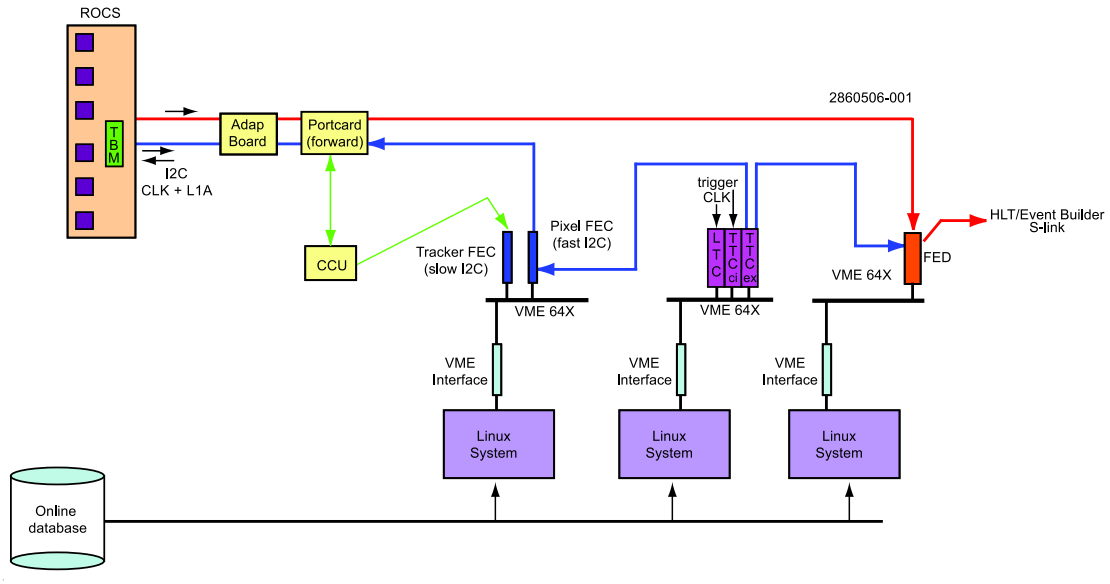

Figure B.1: Components of the CMS pixel control and readout system.

and digitize the pulse height. From this data, software determines which pixels were hit and how much charge was collected on each one.

The digital-analog hybrid data stream allows the data to be read out quickly, but it is a complicated system to set up. Many settings on many types of electronics must be calibrated to produce a data stream that can be reliably decoded. This Appendix first describes the components of the readout system and then describes the calibrations used to prepare the detector for operation.

B.1 Pixel Detector Electronics

A schematic of the components of the CMS pixel detector is shown in Fig. B.1. These components are explained below.

B.1.1 Readout Components

The most basic collection of pixels is the ROC (readout chip) [26]. A ROC contains 4160 pixels arrayed in 80 rows and 52 columns. Despite the large number of pixels, this chip is quite small – less than 1 cm square. It contains all the circuitry used to collect and store charge. It also stores hits from every LHC bunch crossing long enough for the CMS trigger to make its decision and propagate it back to the detector. When an affirmative trigger decision reaches the front end, it informs each ROC to transmit its stored hits.

ROCs are grouped into "channels", each of which is read out by a dedicated optical link. A channel contains 8 to 24 ROCs. These ROCs are chained together and controlled by a TBM (token bit manager). When the TBM receives a trigger decision, it transmits a short header data stream on the output line and then passes a readout token to the first ROC in the chain. This ROC transmits a short header and then its hits as an electrical signal to the TBM, which amplifies the signal and passes it as output. When the first ROC finishes transmitting, it passes the token to the next ROC, which sends its signal and passes the token. This chain continues until all the ROCs have transmitted and the token returns to the TBM. Finally, the TBM transmits a short trailer to signify the end of the data stream.

The data stream is transmitted with a 40 MHz clock cycle; this clock operates at the CMS bunch crossing frequency.

Figure B.2 shows an example of the output data stream from a TBM. In this example, only one ROC is connected to the TBM, and that ROC reports one hit. The signal begins with a TBM header lasting for 8 clock cycles. The header

first transmits 3 cycles at a very low level, called "ultrablack", and 1 cycle at a medium level, called "black". It then transmits an event counter, encoded in 4 discrete address levels, in the next 4 cycles. Then the first ROC transmits its 3-cycle header, which consists of 1 clock cycle at ultrablack, 1 at black, and the last cycle at a level related to the last configuration setting changed on the ROC or to the temperature of the ROC. After the header, the ROC transmits its hits. Each hit takes 6 cycles to transmit. The first 5 are the row and column of the hit, trasmitted using 6 discrete address levels. The last is the pulse height, where the analog value is correlated with the amount of charge collected. All hits on the ROC are transmitted in this way. When this is finished, the next ROC in the chain transmits its header and any hits. Finally, when all ROCs have transmitted, the TBM adds an 8-cycle trailer that begins with 2 ultrablacks and 2 blacks and finishes with 4 cycles coding for status information. In this scheme, the ultrablack levels are used to uniquely identify the TBM header (3 consecutive), ROC header (1), and TBM trailer (2 consecutive).

The electrical signal produced by the TBM is converted to an optical signal with an analog opto-hybrid (AOH) mounted on a circuit board called a supply board (in the barrel section of the detector) or a port card (in the forward region). The optical signal is transmitted off the detector to a FED (Front End Driver) board.[1] The FED decodes the signal and passes the hits to the CMS event builders for storage and later analysis. During data-taking and a few calibrations, this data is passed over a high-speed S-link [27] connection. In most calibrations, either the hits or raw data from the FED's analog-to-digital converter (ADC) are sent over a VME interface to the computer controlling the FED. The process of decoding the data stream is described in Section B.2.

[1] Each FED receives and decodes the output of 36 optical links.

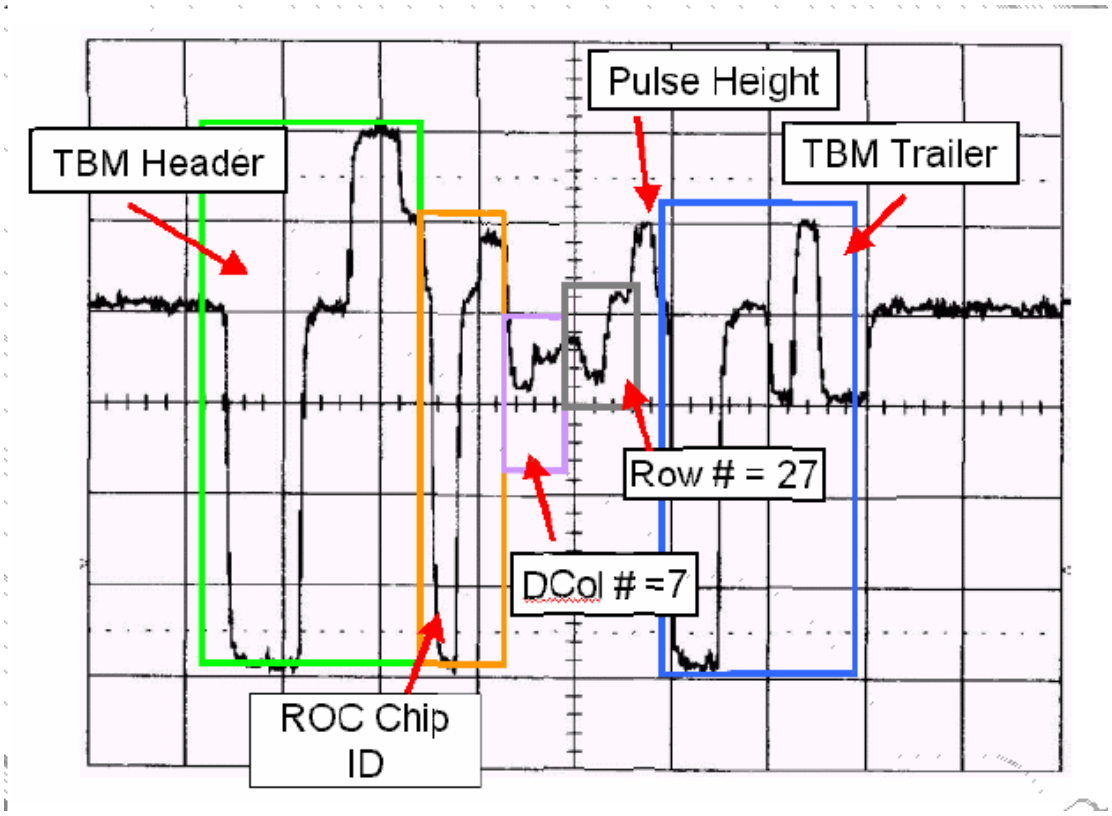

Figure B.2: Output data stream from a TBM connected to one ROC which reports one hit.

Many settings on the ROC, TBM, AOH, and FED must be adjusted to allow the data stream to be decoded. These settings must ensure that the signal has a wide dynamic range with good separation between black and ultrablack and between address levels, while keeping the signal within the FED's dynamic range. Also, the relationship between the charge received on a pixel and the measured pulse height should be as linear as possible. The calibrations used to perform these adjustments are described in Section B.3.

B.1.2 Control Components

Settings on the ROC and TBM are adjusted via a signal that originates on a FEC (Front End Controller) board. This signal is coded with the I2C protocol. The FEC passes the signal via fiber optic cable to the front end. Here, the optical signal is converted to an electrical signal by a digital opto-hybrid (DOH) on the supply board or port card. The timing of the control signal with respect to the clock is adjusted by a Delay25 chip. The electrical signal is passed to the TBM and then to the ROCs.

The supply boards and port cards contain settings that affect the flow of data to and from the detector; these settings must also be adjusted. The readout link is adjusted by the AOH settings, which determine the intensity and range of the optical output. For the control link, the Delay25 chip must be set correctly; commands will not reach the TBM and ROCs if these settings are not properly adjusted.

Settings on the supply boards and port cards are controlled by a separate link that also uses the I2C protocol, though with slower timing. Signals are sent by a "tracker FEC" (TKFEC) board. This board is the same hardware as the FEC that controls ROCs and TBMs (called the "pixel FEC"), but it uses the same firmware as the FECs used in the CMS strip tracker. Because each supply board and port card contains multiple channels (*i.e.*, optical links), there are far fewer tracker FECs than pixel FECs.

B.1.3 Timing and Trigger Components

The last class of hardware in the pixel system is the timing and trigger system. During data-taking, this system distributes level one triggers from the CMS trigger to the front end and to the readout electronics. This instructs the front end to transmit the hits for a particular bunch crossing and instructs the FEDs to decode the received data. The signal to the front end is sent via the FECs and the control link.

When running calibrations, the software instructs the trigger system to issue triggers to the hardware when the calibration algorithm calls for it. In some calibrations the ROCs are configured to inject calibration charge into some of the pixels when they receive a trigger. In all calibrations, the trigger generates a stream of output that is recorded by the FEDs and then passed to the computer for analysis.

B.2 Decoding the Analog Data Stream

Each FED contains receivers that convert the optical signal into an electrical signal. The electrical signal then passes to an ADC, which for every clock cycle converts the analog level to an integer in the range 0-1023. The FED may either decode the signal from these digital values, or it may store them in a buffer to be read out later.

B.2.1 Using the FED State Machine

During normal data-taking and in some of the calibration algorithms, the analog data stream is decoded in the FED by a state machine. The FED is configured with ranges that define the ultrablack level, the black level, and the address levels used to encode status information and the pixel row and column numbers. The state machine looks for the TBM header, ROC headers, and the TBM trailer (which contain 3, 1, or 2 clock cycles of ultrablack). It then records and stores the pixel address and the digitized pulse height for each hit. These hits are read out over an S-link interface during data-taking, and in some calibrations the hits are read out to the computer over the VME interface to be used by the calibration algorithm.

B.2.2 Using Transparent Mode

In "transparent mode" the raw ADC values are stored in a buffer and then read out over VME by the computer running the calibration. The computer then attempts to decode the signal. This process is a modified version of the FED state machine. When running a calibration the number of hits generated is known, so the decoder algorithm only needs to find the TBM header. It then knows where the signal from each ROC begins, and it knows where the TBM trailer begins. To verify successful decoding, the TBM trailer is checked; if it shows two ultrablack levels in the expected location, the decoding is considered successful. This decoding gives, for each trigger, a value for each ultrablack level, black level, address level, or pulse height measurement.

Transparent mode and this manual decoding process are needed for any cal-

ibration that adjusts or measures ultrablack, black, or address levels.

B.3 Calibrations

The software controlling the pixel hardware runs on Linux PCs connected by a VME interface to crates of FECs, FEDs, and trigger electronics. These computers run calibration algorithms that send commands to the electronics to configure the detector, issue triggers, and collect data. The calibrations used to set up the readout chain are described below in the order in which they are typically run. At the end of this sequence of calibrations, the front end produces data streams that can be reliably decoded by the FED.

B.3.1 Delay25 Settings

The Delay25 chip on the supply board / port card adjusts the timing of the control signal from the FEC to the TBM and ROCs. When the Delay25 settings are not set properly, commands do not reach the TBM and ROCs. Other calibrations are not possible without these commands.

The calibration algorithm scans over the Delay25 settings and, at each scan point, tries to send four different types of commands to the TBM. When a command is sent, the return status is checked to see if the command was received. A scan point is considered good if all four types of commands were successfully received.

The scan finds a region of good Delay25 settings, and it chooses a set of

values in the middle of the good region.

B.3.2 AOH Bias Settings

Introduction and Discussion

The AOH bias is a setting on the supply board / port card which controls the amount of light sent along the optical fiber to the FED. There is one AOH bias setting per FED channel. As AOH bias increases, more light is sent, and the analog level on the FED increases. At low values of AOH bias, the black and ultrablack levels do not change with AOH bias, and there is no separation between them. At some threshold, the black level begins to increase approximately linearly. At a higher threshold, the ultrablack level also starts to increase linearly with approximately the same slope. This behavior is illustrated in Fig. B.3.

The maximum black-ultrablack separation depends on the TBM settings. At low settings, the TBM outputs a signal with relatively low separation; as these settings increase, the separation also increases. In the AOH bias scan, the black level is independent of the TBM settings. However, the linear rise of the ultrablack level begins at a later point for higher TBM settings, and hence the black-ultrablack difference saturates at a higher AOH bias value when the TBM settings are higher.

The goal of the AOH bias calibration is to determine an AOH bias setting for each channel that is high enough to saturate the black-ultrablack difference. The calibration measures this difference, using black and ultrablack levels from the TBM header and trailer, as a function of AOH bias. From this data it determines

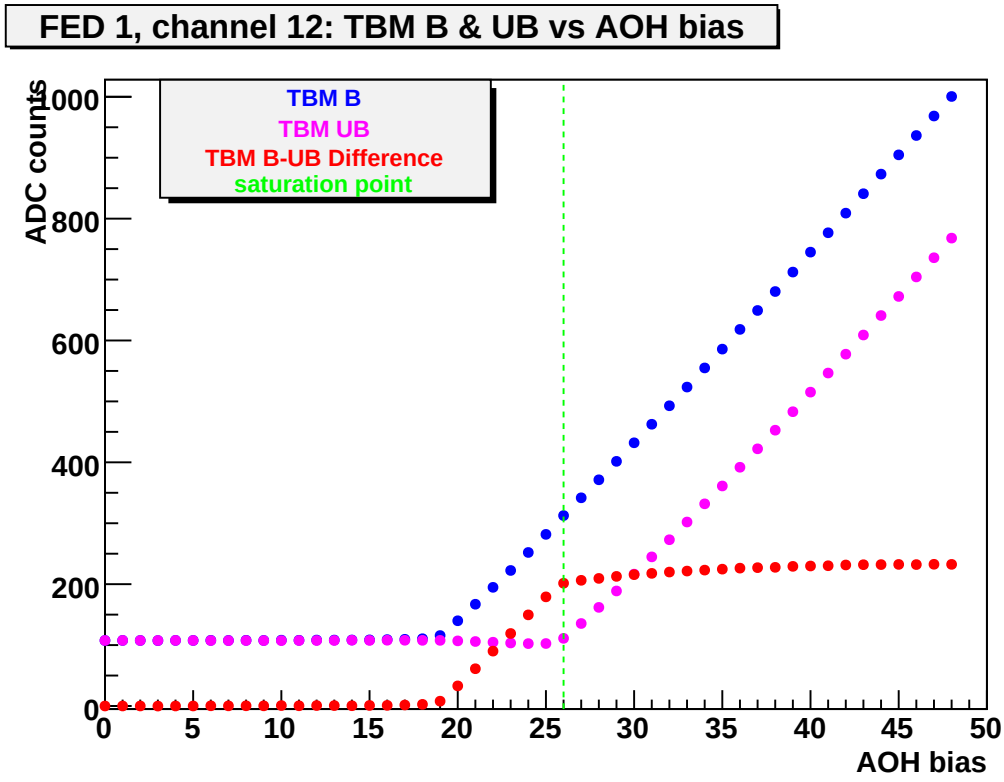

Figure B.3: Black and ultrablack levels as a function of AOH bias. The vertical green line indicates the AOH bias value at which the black-ultrablack difference saturates.

the saturation point. It is important, though, that during the scan the TBM settings are at least as high as they will be set in later calibrations and physics runs. Otherwise, the AOH bias value determined from the saturation point will be too low. Further increases in the TBM settings will not increase the black-ultrablack separation because the AOH cannot provide more separation.

Temperature variations alter the response of the AOH, essentially shifting the curves in Figure B.3 to the left or right. In order to provide a margin of error for temperature changes, the AOH bias should be set higher than the saturation value. A temperature increase of 5 degrees Celcius will shift the curves by about 4 AOH bias counts. Therefore, the chosen AOH bias setting will be 4 counts

higher than the saturation value.

The FED optical receivers, which convert the optical signal into an electrical signal before it is digitized, contain offsets that adjust the level of the electrical signal. There are two types of settings: optical receiver offsets that affect 12 channels together, and individual-channel offsets that allow finer adjustments for each channel. If the intensity of the optical signal is too high, the offsets cannot compensate enough to put the signal inside the FED ADC's dynamic range. It is therefore important that the AOH bias not be too high.

The last part of the AOH bias calibration is to do a coarse adjustment of the FED baseline – the signal level recorded by the FED's ADC when the TBM is not transmitting data or is transmitting the black level. The FED individual-channel offsets are set to the center of their range, and then the optical receiver offsets and AOH bias settings are adjusted to bring all FED baselines into a wide target range centered in the middle of the ADC's range (512). AOH bias may be lowered below the previously chosen value only if it is absolutely necessary. The end result of this calibration is a configuration of AOH bias and FED offset values that puts all FED baselines near the center of the dynamic range, with AOH bias values that allow for a large black-ultrablack separation.

There is a separate calibration routine, described in Section B.3.3, to perform finer adjustments of the FED baseline (using the freedom to move each channel offset). It should be run after the AOH bias calibration.

AOH Bias Calibration Algorithm

The calibration algorithm is described below. This procedure is performed for each channel.

The first part of the calibration is to find the AOH bias setting at which the black-ultrablack difference saturates. This requires measuring the black and ultrablack levels as a function of AOH bias. Two scans of AOH bias are performed:

- In the first scan, at each scan point several triggers are issued, and for each trigger the stream of ADC values from the FED is read out. The software attempts to decode the data stream by searching for the ultrablack and black levels of the TBM header and trailer. (This process is described in Section B.2.) This decoding is unsuccessful at low AOH bias values, where there is no separation between ultrablack and black, and also fails at high values, where the signal is above the ADC's dynamic range. It succeeds for intermediate AOH bias values. If decoding is successful, the calibration records at what times in the data stream the black and ultrablack levels occur. The times are the same on every trigger, and they are saved for later use.
- In the second scan, again triggers are issued and the FED data stream is read out. In this scan the black and ultrablack levels are recorded using the times from the previous scan.[2] This method of using previously determined times allows levels to be measured even when the data stream

[2]On a small fraction of the channels, the times are not stable and will sometimes be offset by one clock cycle. If a "jumping" phase of this sort is observed in the first scan, the second scan exploits the fact that some black and ultrablack signals last multiple clock cycles. It takes data only from those clock cycles which will be definitely black or definitely ultrablack, for either of the two phases.

cannot be decoded.

From the measured levels, the black-ultrablack difference is calculated as a function of AOH bias. The saturation point, plus an offset of 4 counts to allow for temperature changes, is taken as the tentative value for AOH bias. Figure B.3 shows an example, for one channel, of the collected data and the saturation point.

The final part of the calibration is the coarse baseline adjustment. The baseline is measured from the black level in the TBM header and trailer. The FED optical receiver input offsets and the AOH bias settings are adjusted to place the black level in a wide target range centered at 512 ADC counts. Both settings move the black level; the algorithm's first priority is to not reduce any AOH bias setting below the tentative value determined previously, unless absolutely necessary. The individual channel offsets are not adjusted here; instead they are set to the center of their range. They will be adjusted in the next calibration.

B.3.3 FED Baseline Calibration

The goal of the FED baseline calibration is to adjust the optical receiver offsets so that the baseline value is at the center of the ADC's dynamic range (512). If the AOH bias calibration has already been run, the baseline will start near 512. This calibration performs finer adjustments using the individual channel offsets (and, if necessary, the coarser offsets affecting 12 channels at once).

The calibration algorithm is an iterative process. First the baseline is measured for each channel by reading out ADC values from the FED. Next the off-

sets are adjusted in a direction that moves each baseline closer to 512. Then the baselines are measured again, and the offsets adjusted again. This process continues until no further improvement is possible.

In normal running, the FED performs an "automatic baseline correction" to compensate for small shifts in the baseline and automatically place it at exactly 512. This is implemented as a time-varying digital offset added to the value from the ADC. During the FED baseline calibration, this correction is turned off, as the goal is to adjust the raw output of the ADC.

B.3.4 FED Phase and Delay Scan

To decode the data stream from the front end, the FED first digitizes the analog value from the optical link. This digitization occurs once per 25-ns clock cycle. However, the analog signal does not move instantly to its new value on each clock cycle; it takes some time for the value to change. To provide reliable and consistent black, ultrablack, address, and pulse height levels, it is important that the input is sampled at a time when the value is stable, and not when it is transitioning to a new value.

Each FED channel contains two settings that determine at what point in the clock cycle the sampling and digitization occur. A phase bit sets whether the sampling occurs on the rising or falling edge of the 40-MHz clock. A delay setting moves the sampling point in time; there are 16 possible settings spaced evenly across the 25 ns cycle.

In this calibration the 32 values of the phase and delay are scanned. For each

setting, a fixed number of triggers are issued, and after each trigger the digitized data stream for each channel is read out from the FEDs. For each channel, the calibration chooses phase and delay values that appear to sample the signal when it is stable. For example, at a good setting the three ultrablack levels in the TBM header will be nearly equal; at a bad setting the first will be higher than the next two because it is read out while the signal is moving from black to ultrablack.

B.3.5 AOH Gain Calibration

The AOH gain is a setting for each optical link (from detector to FED) that has just 4 possible settings (0, 1, 2, 3). This setting does not change the black level. Instead, it scales the size of deviations from the black level, expanding or shrinking the signal. Larger settings correspond to larger deviations. In particular, the separation between black and ultrablack levels will be larger at a larger gain. Settings on the TBMs and ROCs will be the primary means of adjusting the ultrablack to the desired level, but the AOH gain must be set large enough in order to make possible a low enough ultrablack. However, AOH gain should not be set too high since larger settings will increase the power drawn, and larger settings are intended to be used to compensate for radiation damage over time.

The aim of this calibration is to set the AOH gain at the lowest level that will allow sufficient separation between black and ultrablack. The three TBM gain settings are set to high values. Then, for each FED channel, the ultrablack level in the TBM header and trailer is recorded as a function of AOH gain by reading out and decoding the data stream for a number of triggers. To choose

an AOH gain setting, the calibration selects the smallest value that produces an ultrablack below a user-defined threshold.

B.3.6 TBM Ultrablack Calibration

With the black level set at 512 by the baseline calibration and automatic baseline correction, the next step is to set the ultrablack levels appropriately. We first adjust settings on the TBM to set the TBM header and trailer ultrablack to an appropriate value. (Experience suggests that a value of 120 to 150 is good.)

There are three settings on the TBM, all of which affect the ultrablack level. Higher values of these settings correspond to lower ultrablack (and greater black-ultrablack separation). These settings also scale the rest of the TBM and ROC output.

The TBM UB calibration routine can run in either of two modes, as selected by the user:

1. Fix two settings and scan the third.
2. Scan all three settings simultaneously. During the scan, all three settings are moved simultaneously and linearly through their scan ranges.

In either mode, the calibration searches for settings that put the TBM ultrablack at the target level. The second mode, where all three settings are varied simultaneously, is usually best.

The calibration procedure is similar to the AOH gain calibration. Ultrablack levels from the TBM header and trailer are recorded for each trigger by reading

out and decoding the transparent data. This is performed for a number of triggers at each scan point. At the end of the scan, the calibration selects the TBM settings that place the ultrablack level closest to the target value, interpolating between scan points if appropriate.

There is a special case for "dual" TBMs. In the barrel section of the detector, some TBMs control two sets of ROCs and output data on two channels. These two channels produce separate data streams on the FED, but they share the same TBM settings. Therefore they cannot be adjusted independently to put both channels' ultrablack at the target level. For a dual TBM, we choose settings so that one channel is at the target ultrablack level, and the other is below.

B.3.7 ROC Ultrablack Equalization Calibration

This calibration is the ROC analogue of the TBM ultrablack calibration. It adjusts a setting on each ROC, called `VIbias_DAC`, to place the ROC ultrablack at the same level as the corresponding TBM's ultrablack. (The black level cannot be adjusted, but it is automatically close to the TBM's black level.) This setting also scales the rest of the ROC output – address levels and pulse heights.

The calibration algorithm is similar to the TBM ultrablack calibration. Transparent data is collected and decoded for multiple triggers at each scan point. From this data each TBM and ROC's ultrablack level is recorded and stored. During the scan the ROC ultrablack changes, but the TBM ultrablack is stable. At the end of the scan, each ROC's `VIbias_DAC` setting is chosen to place the ROC ultrablack at the same level as the TBM ultrablack, interpolating between scan points if appropriate. (Each ROC is recorded and adjusted individually.)

B.3.8 Address Level Determination

The address level calibration determines the values used by the FED to decode the incoming data. This includes pixel row and column address levels, TBM header and trailer levels, and the black and ultrablack levels.

The calibration enables the generation of hits so that pixel address levels will be produced. The specific pixels enabled are designed to probe combinations of address levels that could potentially cause problems, such as transitions from high to low levels and vice versa.

For each trigger, the transparent buffer is read out, and the ADC values for pixel address levels are placed in a histogram for each ROC. Each TBM's address levels are placed in a separate histogram. In all histograms, the calibration searches for the peaks corresponding to the six (ROC) or four (TBM) address levels. It selects bounds that enclose each peak and saves these bounds as configuration settings for the FED state machine.

B.3.9 Linearity vs. Vsf

The ROC setting `Vsf` affects the linearity of the pixel response vs. received charge; larger values improve linearity. `Vsf` also affects the digital current drawn by the ROC, with higher values increasing the current. We have implemented two algorithms to set `Vsf` at a value that gives good linearity without drawing excessive power. The first is described in this section.

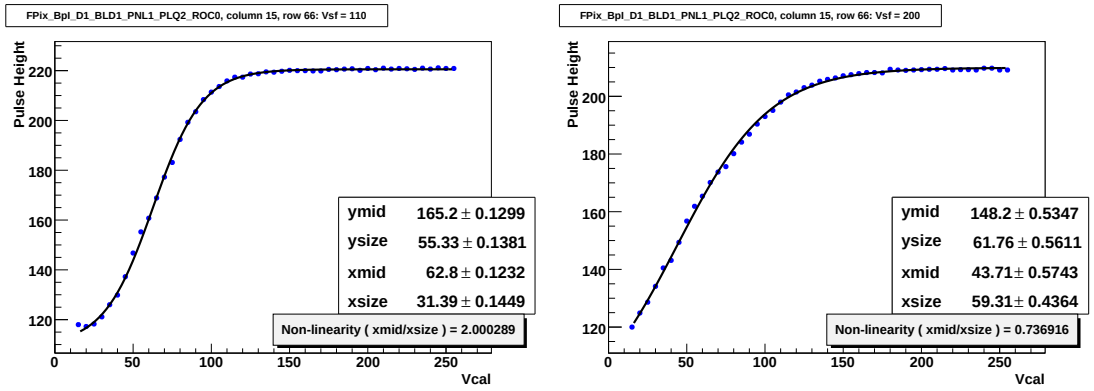

Figure B.4: Scans of pulse height vs. Vcal at different values of Vsf. The scan on the left has poor linearity, and the scan on the right has good linearity.

Introduction and Discussion

This algorithm measures linearity from scans of pulse height vs. injected charge – which is proportional to the ROC setting `Vcal` – at different values of `Vsf`. Examples of these scans are shown in Fig. B.4.

To quantify the degree of nonlinearity, the scan data are fit with a function

$$PH = f(Vcal) = y_{\text{mid}} + y_{\text{size}} \times \tanh\left(\frac{Vcal - x_{\text{mid}}}{x_{\text{size}}}\right) \tag{B.1}$$

where PH is the recorded pulse height, $Vcal$ is ROC setting controlling the amount of injected charge, $(x_{\text{mid}}, y_{\text{mid}})$ is the point at the center of the quasi-linear rise region of the hyperbolic tangent, x_{size} is the horizontal scale of the quasi-linear region, and y_{size} is the vertical scale of that region.

From this fit, the degree of nonlinearity can be quantified in different ways. The simpler nonlinearity parameter, used by default in this calibration, is $x_{\text{mid}}/x_{\text{size}}$. When this parameter is small, it means that `Vcal` = 0 lies within the quasi-linear rise region, and hence the response is linear for small amounts of

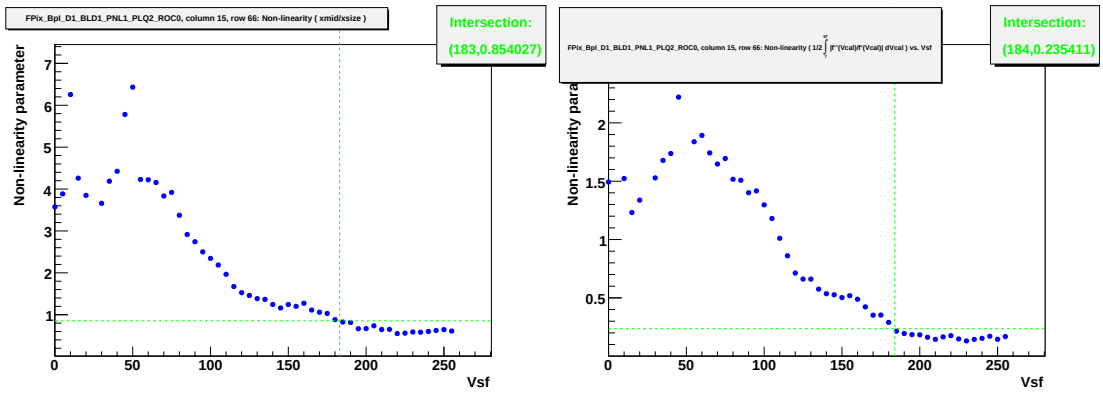

Figure B.5: Plots of nonlinearity vs. Vsf. On the left, nonlinearity is measured by $x_{\text{mid}}/x_{\text{size}}$, and on the right, it is measured by the integral in Eq. B.2. The green lines indicate the chosen Vsf setting.

injected charge. Previous studies have used $x_{\text{mid}}/x_{\text{size}} = 1.4$ as the cutoff – values below 1.4 indicate good linearity.

An alternate nonlinearity parameter is

$$\frac{1}{2}\int_{Vcal_{\text{min}}}^{Vcal_{\text{max}}} dVcal \left|\frac{f''(Vcal)}{f'(Vcal)}\right| \tag{B.2}$$

where $f(Vcal)$ is the hyperbolic tangent function in Eq. B.1. This integral is a measure of the vertical change due to curvature divided by the vertical change due to slope over the range of the integral. The limits of the integral should be chosen to include the range for which we want good linearity. This integral can be evaluated analytically.

Figure B.5 shows scans of both measures of nonlinearity vs. `Vsf`. As seen in the plots, they give similar shapes. This calibration allows the user to choose either measure; the default is $x_{\text{mid}}/x_{\text{size}}$.

Linearity vs. Vsf Calibration Steps

This calibration consists of the following steps:

1. Enable the generation of one or more calibration hits on each ROC.
2. Scan over `Vcal` and `Vsf`. On each trigger, read out the decoded hits from the FED. (Note that this uses the FED's internal decoding, rather than the transparent data.) Record the pulse height, keeping separate scans for different pixels.
3. For each scan of pulse height vs. `Vcal` (for a given ROC, pixel, and `Vsf` value), fit with the function in Eq. B.1. (See Fig. B.4 examples of these scans.) If the fit is successful, compute the nonlinearity parameter (either $x_{\text{mid}}/x_{\text{size}}$ or the integral in Eq. B.2) and add it to a scan of nonlinearity vs. `Vsf` for that ROC and pixel. (See Fig. B.5 for examples of this scan.)
4. For each scan of nonlinearity vs. `Vsf`, determine an optimal `Vsf`. This is done by finding the highest `Vsf` where the scan intersects a nonlinearity threshold. This threshold may be either a fixed value or a multiple of the nonlinearity at the highest `Vsf` in the scan.
5. For each ROC, examine the optimal `Vsf`s on the various pixels. If there are at least 4 pixels, discard any `Vsf` outliers. After any discarding, average the `Vsf` values to determine the `Vsf` setting for that ROC.

B.3.10 Vsf and VHldDel

We have also implemented a simpler algorithm for determining `Vsf`, as well as the ROC setting `VHldDel`, which controls the time at which each pixel's re-

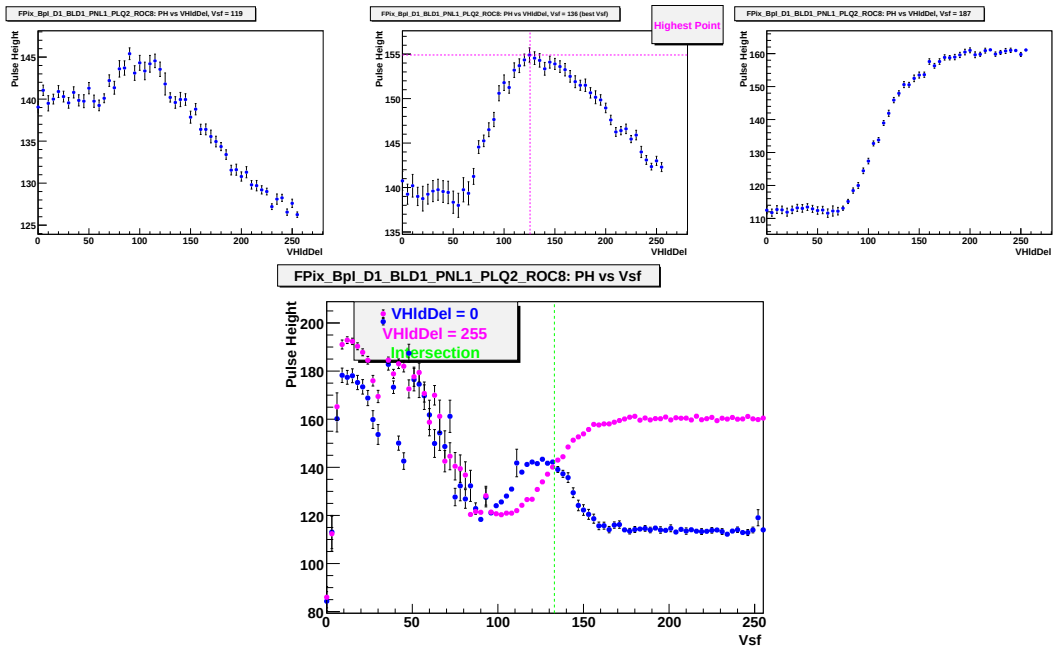

Figure B.6: *Top row:* Pulse height vs. VHldDel at low, medium, and high values of Vsf. As Vsf increases, the right endpoint increases. The best Vsf value is the one for which the pulse heights measured at VHldDel = 0 and VHldDel = 255 are equal. The purple line in the middle plot indicates the chosen VHldDel setting. *Bottom plot:* Pulse height at the endpoints of these plots, as a function of Vsf. The green line indicates the chosen Vsf setting. Low values of Vsf produce garbage output.

ceived charge is sampled. Figure B.6 shows plots of pulse height vs. `VHldDel` at low, medium, and high values of `Vsf`, with a small amount of injected charge. Operating experience has shown that linearity is good at a `Vsf` value for which this curve rises and then falls so that the pulse heights at the two endpoints (lowest and highest `VHldDel`) are equal. Figure B.6 also includes a plot of these endpoints as a function of `Vsf`; the rightmost intersection point is the `Vsf` value chosen. Low values of `Vsf`, below ~90, produce garbage output.

After choosing a `Vsf` value, `VHldDel` should be set to the value that maximizes the pulse height.

These `Vsf` and `VHldDel` settings are found to give good linearity in pulse height vs. injected charge, while not drawing too much power.

Data collection uses the same method as described for the previous calibration in Sec. B.3.9 – reading pulse height information from the decoded hits at each scan point.

This procedure is typically split into two calibration runs – the first to determine `Vsf` and the second to determine `VHldDel`. If the algorithm described in Sec. B.3.9 is used to determine `Vsf`, `VHldDel` should be set with the algorithm used here – maximizing pulse height at the chosen `Vsf`.

B.3.11 Pulse Height Range Calibration

A number of ROC settings affect the scaling of the pulse height signal that is sent to the FED. (This refers not to the actual charge collection, but to the translation of that charge into the signal sent out on the optical link.) We want the range of this signal – the difference in recorded pulse height between small and large amounts of charge – to be large. However, the pulse height signal should not go low enough to be confused with the ultrablack level, nor high enough to exceed the FED's dynamic range.

The ROC setting `VIbias_PH` is intended to be used for adjusting the pulse height. Several other settings also affect the pulse height, and they may also be scanned.

The algorithm for this calibration is rather minimal. In the configuration, the user specifies a set of ROC settings to be scanned, and also "low" and "high"

amounts of injected charge (*i.e.*, low and high `Vcal` settings). The pulse height is recorded at each scan point for the low and high charges. (If multiple pixels are enabled, their pulse heights are averaged on each ROC.) A scan point is discarded if the low reading is too close to ultrablack, or if the high reading is near the top of the FED's dynamic range. From the remaining scan points, the point chosen is the one with the largest pulse height difference between high and low charges. The ROC settings at this point are written out for later use.

B.4 Conclusion

Given the large number of components in the CMS pixel detector readout system, a great deal of setup is required to enable data-taking. Many settings must be adjusted properly just to provide an analog output stream that the FED can decode. Still more settings are needed to improve the quality of that decoded data – to provide a linear response to collected charge and a wide dynamic range. Each of the calibrations described above is an essential element in providing reliable, high-quality data from the pixel detector.

BIBLIOGRAPHY

[1] W.-M. Yao *et al.*, Journal of Physics G **33**, 1 (2006).

[2] T. E. Browder (1996), hep-ph/9611373.

[3] J.L. Rosner, Phys. Rev. D **60**, 114026 (1999).

[4] B. Bhattacharya and J. L. Rosner, Phys. Rev. **D77**, 114020 (2008), arXiv:0803.2385.

[5] D. Asner, Ph.D. thesis (2000).

[6] Q. He *et al.* (CLEO Collaboration), Phys. Rev. Lett. **100**, 091801 (2008), arXiv:0711.1463.

[7] D. Peterson *et al.*, Nucl. Instrum. Methods A **478**, 142 (2002).

[8] M. Artuso *et al.*, Nucl. Instrum. Methods A **554**, 147 (2005), physics/0506132.

[9] Y. Kubota *et al.* (CLEO Collaboration), Nucl. Instrum. Methods A **320**, 66 (1992).

[10] D. J. Lange, Nucl. Instrum. Methods A **462**, 152 (2001).

[11] E. Barberio and Z. Was, Comput. Phys. Commun. **79**, 291 (1994).

[12] R. Brun *et al.*, GEANT 3.21, CERN Program Library Long Writeup W5013 (unpublished) 1993.

[13] D. Cassel *et al.*, *Determination of Tracking, K^0_S, and π^0 Efficiencies*, CLEO CBX 05-07.

[14] J. Gaiser, Ph.D. thesis, SLAC (1982), SLAC-0255.

[15] B. Heltsley and H. Mahlke, *Branching Fractions for $\psi(2S)$ Transitions to J/ψ and for $J/\psi \to \ell^+\ell^-$*, CLEO CBX 04-47.

[16] S. Stroiney *et al.*, *Determination of Tracking Efficiency Systematics with Full 818 pb^{-1} Dataset*, CLEO CBX 2008-040.

[17] S. Stroiney *et al.*, *Determination of K^0_S Efficiency Systematic with Full 818 pb^{-1} Dataset*, CLEO CBX 2008-041.

[18] I.I. Bigi and H. Yamamoto, Physics Letters B **349**, 363 (1995).

[19] J. L. Rosner, Phys. Rev. **D74**, 057502 (2006), hep-ph/0607346.

[20] D.-N. Gao, Physics Letters B **645**, 59 (2007).

[21] H. Albrecht *et al.* (ARGUS Collaboration), Phys. Lett. B **241**, 278 (1990).

[22] S. Dobbs *et al.* (CLEO Collaboration), Phys. Rev. **D76**, 112001 (2007), arXiv:0709.3783.

[23] G. L. Bayatian *et al.* (CMS Collaboration), CERN-LHCC-2006-001 (2006).

[24] CMS Tracker TDR, CERN-LHCC-98-6 (1998).

[25] Addendum to the CMS Tracker TDR, CERN-LHCC-2000-016 (2000).

[26] H. C. Kaestli, M. Barbero, *et al.*, Nucl. Instrum. Methods A **565**, 188 (2006), physics/0511166.

[27] E. van der Bij, R. A. McLaren, *et al.*, IEEE Trans. Nucl. Sci. **44**, 398 (1997).